

Norwegian University of Science and Technology  
Kavli Institute for Systems Neuroscience / Centre for Neural Computation / Egil and Pauline  
Braathen and Fred Kavli Centre for Cortical Microcircuits

Master's thesis in Neuroscience

Trondheim, June 2020

Effects on Tau Hyperphosphorylation as a Function of  
Lowering Levels of Reelin in Entorhinal Cortex Layer II  
Neurons

Author:

Tore Bryntesen Lund

Supervisor:

Dr. Asgeir Kobre-Flatmoen



NTNU

Kavli Institute for  
Systems Neuroscience

## **Acknowledgements**

The work presented in this master's thesis was carried out in the Witter Group at the Kavli Institute for Systems Neuroscience at the Norwegian University of Science and Technology.

First, I would like to thank Professor Menno P. Witter for taking me on as a master's student and providing me with the opportunity to be part of his lab. The learning experience I have had, and skill set I have acquired while being a master's student in your lab has far exceeded any expectations I had before starting the work on my thesis.

I would especially like to extend my gratitude to my thesis supervisor Dr. Asgeir Kobro-Flatmoen. Thank you for being supportive and understanding of my health-related issues and medical hiatus that unfortunately occurred during the work on this thesis. You also deserve much praise for always having both the time and patience to provide me with help and guidance whenever I needed it. Thank you for letting me be part of such an exciting research project on Alzheimer's disease.

I would also like to thank Bruno Monterotti, Grethe M. Olsen, and Paulo Girão for technical support and excellent laboratory training.

Last, but not least I would like to thank Andrea for her love and support during my work with this thesis.

## Abstract

Alzheimer's disease (AD) is a progressive, and ultimately fatal neurodegenerative disorder, characterized by the neuropathological hallmarks amyloid- $\beta$  plaques and neurofibrillary tangles. It is estimated that the pathological alterations in neurons associated with the disease starts 10-20 years prior to the onset of clinical symptoms. For this reason, understanding the molecular mechanisms that initiate the disease is crucial. Entorhinal cortex (EC) is affected particularly early in the course of AD, and neurofibrillary tangle pathology first occurs in neurons in EC LII. The neurons in EC layer II, particularly those that express the protein reelin, give rise to projections to the hippocampal formation, a region that is essential for memory functions. Disruption of normal reelin function has been shown to contribute to the neuropathology seen in AD, including hyperphosphorylation of tau protein via upregulation of the tau protein kinase glycogen synthase kinase-3 $\beta$  (GSK3 $\beta$ ). Based on recent evidence that demonstrate that intracellular amyloid- $\beta$  co-localize in the EC layer II reelin-immunoreactive neurons implicated in the onset of neurofibrillary tangle pathology, we hypothesized that lowering the levels of reelin in EC layer II neurons would increase levels of GSK3 $\beta$  and hyperphosphorylated tau. Stereotaxic injection of a novel viral construct containing micro-RNA targeted to interfere with translation of reelin, were performed in three different transgenic animal models for AD: the APP/PS1 mouse model, the 3xTG mouse model and the McGill-R-Thy1-APP rat model. Reelin was successfully lowered in EC layer II neurons in all three animal models. However, no consistent change was observed with respect to levels of hyperphosphorylated tau and GSK3 $\beta$  in EC LII.

## Abbreviation list

3xTG	Triple-transgenic mouse model	mRNA	Messenger-RNA
3R/4R	Three-repeat/Four-repeat	miRNA	Micro-RNA
AAV	Adeno-associated virus	MCI	Mild cognitive impairment
A $\beta$	Amyloid- $\beta$	N	Number of (animals/cells)
ABC	Avidin-biotin complex	NaCl	Sodium chloride
AD	Alzheimer's disease	NaHCO <sub>3</sub>	Sodium Bicarbonate
AICD	APP intracellular domain	NFT	Neurofibrillary tangle
APir	Amygdalopiriform transition area	NGS	Normal goat serum
APOE	Apolipoprotein E	NTNU	Norwegian University of Science and Technology
APP	Amyloid precursor protein	p-Tau	Hyperphosphorylated tau
BACE1	$\beta$ -secretase cleavage enzyme 1	PA	Primary antibody
CA	Cornu ammonis	PB	Phosphate buffer
CDK5	Cyclin-dependent protein kinase-5	PBT	PB containing 0.2% Triton X-100
CE	Caudal entorhinal area	PDPK	Proline-directed protein kinase
CMV	Cytomegalovirus	PFA	Paraformaldehyde
CSF	Cerebrospinal fluid	PHF	Paired helical filaments
CTF	C-terminus fragment	PS1/PSEN1	Presenilin-1
DAB	3,3'-Diaminobenzidine	PS2/PSEN2	Presenilin-2
DIE	Dorsal intermediate entorhinal area	RE	Reelin
DLE	Dorsolateral entorhinal area	RNA	Ribonucleic acid
DMSO	Dimethyl sulfoxide	ROI	Region of interest
DNA	Deoxyribonucleic acid	SA	Secondary antibody
EC	Entorhinal cortex	SD	Standard deviation
GFP	Green fluorescent protein	Ser	Serine
GSK3 $\beta$	Glycogen synthase kinase-3 $\beta$	TBS	Tris-buffered saline
H <sub>2</sub> O <sub>2</sub>	Hydrogen peroxide	TBS-Tx	Tris containing 0.2% Triton X-100
HIAR	Heat induced antigen retrieval	Tet	Tetracycline-controlled transactivator
HCl	Hydrochloric acid	Thr	Threonine
KCL	Potassium chloride	TR	Transentorhinal region
L	Layer	Tris	Tris(hydroxymethyl)aminomethane
LEC	Lateral entorhinal cortex	Tyr	Tyrosine
LTP	Long-term potentiation	VIE	Ventral intermediate area
M	Mean	WHO	World Health Organization
MAPT	Microtubule-associated protein tau	WT	Wild type
Mdn	Median		
ME	Medial entorhinal area		
MEC	Medial entorhinal cortex		

# Table of contents

<b>Acknowledgements</b> .....	<b>II</b>
<b>Abstract</b> .....	<b>III</b>
<b>Abbreviation list</b> .....	<b>IV</b>
<b>1. Introduction</b> .....	<b>1</b>
1.1 Alzheimer’s disease and dementia .....	1
1.1.1 Historical overview of Alzheimer’s disease research .....	1
1.2 Anatomy of the hippocampal formation and parahippocampal region .....	3
1.2.1 The entorhinal cortex .....	4
1.2.1.1 Entorhinal-hippocampal connectivity through the perforant path.....	4
1.2.1.2 Cell types in layer II of the entorhinal cortex .....	5
1.3 Neuropathology of Alzheimer’s disease.....	6
1.3.1 Neuropathological hallmarks .....	6
1.3.2 Brain atrophy.....	6
1.3.3. Amyloid plaques .....	7
1.3.3.1 Amyloid cascade hypothesis .....	9
1.4 Tau protein and neurofibrillary tangles .....	10
1.4.1 Tau protein .....	10
1.4.2 Tau structure.....	10
1.4.3 Tau hyperphosphorylation.....	11
1.4.4 Tau pathology in the Alzheimer’s disease brain .....	13
1.4.5 Tau protein kinases.....	13
1.5 Reelin.....	14
1.5.1 Reelin function in neurodevelopment and in the healthy brain .....	14
1.5.2 Reelin in Alzheimer’s disease .....	15
1.6 Transgenic animal models of Alzheimer’s disease .....	16
1.6.1 APP/PS1 mouse.....	16

1.6.2	3xTG mouse .....	17
1.6.3	McGill-R-Thy1-APP rat.....	18
1.7	Aims and hypotheses .....	18
<b>2.</b>	<b>Methods.....</b>	<b>20</b>
2.1	Animals.....	20
2.1.1	Housing and animal care .....	20
2.1.2	Animals used .....	20
2.2	Stereotaxic injections.....	20
2.2.1	Viral constructs .....	20
2.2.2	Stereotaxic surgery procedure .....	22
2.3	Tissue processing.....	23
2.3.1	Transcardial perfusion and brain extraction.....	23
2.3.2	Brain sectioning.....	25
2.4	Immunohistochemistry .....	26
2.4.1	Double fluorescent immunohistochemistry protocol in viral-injected tissue.....	26
2.4.2	3,3'-diaminobenzidine .....	28
2.4.3	Cresyl Violet-staining (Nissl-staining).....	28
2.4.4	Tissue mounting and coverslipping.....	29
2.5	Microscopy .....	29
2.5.1	Fluorescent and bright field microscopy .....	29
2.5.2	Tissue scanning .....	29
2.6	Data analysis.....	29
2.6.1	Inclusion criteria for quantitative data analysis.....	29
2.6.2	Quantitative data analysis.....	30
2.6.3	Background subtraction.....	30
2.6.4	Data processing .....	31
2.7	Delineation.....	32

2.7.1	Delineating the lateral entorhinal cortex .....	32
2.7.2	Delineating the medial entorhinal cortex .....	34
2.7.3	Differentiating the lateral entorhinal cortex from the medial entorhinal cortex	34
2.7.4	Delineating entorhinal cortex layer II .....	34
<b>3.</b>	<b>Results .....</b>	<b>36</b>
3.1	Large amounts of non-specific binding in APP/PS1 tissue caused by mouse on mouse cross reactivity with secondary antibody .....	36
3.1.1	Non-specific binding in plaque-like substances in APP/PS1 mice .....	36
3.1.2	Testing in other animal models .....	38
3.1.3	Testing with fluorescent secondary antibodies .....	39
3.1.4	Pre-incubating the secondary antibody reduces non-specific binding .....	40
3.2	Effects on p-Tau and GSK3 $\beta$ following reduction of reelin in entorhinal cortex layer II in the APP/PS1 mouse model .....	42
3.2.1	Reducing reelin in APP/PS1 76502 mouse results in increased levels of measured p-Tau and GSK3 $\beta$ .....	42
3.2.2	Reducing reelin in APP/PS1+Ck2 mouse 75284 results in decreased levels of measured p-Tau and GSK3 $\beta$ .....	45
3.3	Effects on p-Tau and GSK3 $\beta$ following reduction of reelin in entorhinal cortex layer II in the 3xTG mouse model.....	48
3.3.1	Reducing reelin in 3xTG 77132 mouse did not alter the levels of measured p-Tau or GSK3 $\beta$ .....	48
3.4	Effects on p-Tau following reduction of reelin in entorhinal cortex layer II in the McGill-R-Thy1-APP rat model.....	51
3.4.1	Reducing reelin in McGill-R-Thy1-APP rat 25180 results in reduced levels of measured p-Tau.....	51
3.4.2	Reducing reelin in McGill-R-Thy1-APP rat 25181 results in increased levels of measured p-Tau.....	51
3.4.3	Measured levels of reelin and p-Tau was not significantly altered in McGill-R-Thy1-APP rat 25561 .....	52

3.4.4	Reducing reelin in McGill-R-Thy1-APP rat 25562 results in decreased levels of measured p-Tau.....	52
<b>4.</b>	<b>Discussion.....</b>	<b>56</b>
4.1	Summary of main findings .....	56
4.2	Non-specific binding of mouse secondary antibody in APP/PS1 mice.....	56
4.3	Reducing reelin expression in layer II of the entorhinal cortex yields mixed results with respect to levels of p-Tau and GSK3 $\beta$ .....	59
4.3.1	APP/PS1 mice .....	59
4.3.2	3xTG mice .....	60
4.3.3	McGill-R-Thy1-APP rat model .....	60
4.4	Tau in rodent animal models for AD.....	61
4.5	Methodological considerations.....	62
4.5.1	Scanning .....	62
4.5.2	Stereotaxic injections .....	62
4.6	Future directions .....	62
4.7	Conclusions .....	64
<b>5.</b>	<b>References .....</b>	<b>65</b>
<b>6.</b>	<b>Appendices .....</b>	<b>75</b>
Appendix 6.1	List of animals .....	75
6.1.1	Animals used for antibody testing and Nissl staining.....	75
6.1.2	List of injected 3xTG mice excluded from final analysis.....	76
6.1.3	List of injected APP/PS1 mice excluded from final analysis .....	76
6.1.4	List of injected McGill-R-Thy1-APP rats excluded from analysis .....	77
Appendix 6.2	Immunohistochemistry protocols .....	78
6.2.1	pSer396 tau and Reelin G10 double immunofluorescent protocol.....	78
6.2.2	GSK3 $\beta$ Tyr216 and Reelin G10 double immunofluorescent protocol. ....	78
6.2.3	AT8 phospho tau protocol.....	79
6.2.4	AT8 protocol with pre-incubation of SA .....	80

6.2.5 AT8 protocol with Tween-20.....	80
6.2.6 AT8 protocol with Goat SA/Donkey SA .....	82
Appendix 6.3 List of secondary antibodies .....	84
Appendix 6.4 Chemical solutions.....	85
Appendix 6.5 SPSS output from statistical analyses .....	88
6.5.1 APP/PS1 76502.....	88
6.5.2 APP/PS1 75284 .....	89
6.5.3 3xTG 77132.....	90
6.5.4 McGill-R-Thy1-APP 25180.....	91
6.5.5 McGill-R-Thy1-APP 25181 .....	92
6.5.6 McGill-R-Thy1-APP 25561 .....	93
6.5.7 McGill-R-Thy1-APP 25562.....	93



# 1. Introduction

## 1.1 Alzheimer's disease and dementia

Alzheimer's disease (AD) is a progressive and ultimately fatal neurodegenerative disease of the brain. AD is the most common form of dementia and accounts for 60-70% of all dementia cases <sup>1</sup>. Dementia is a general term for several diseases that destroys memory, behavior, cognitive abilities, and a person's ability to perform everyday activities. The brain of a person suffering from AD will undergo molecular abnormalities that selectively and irreversibly damages neurons in a region-specific manner. This ultimately leads to large-scale neuronal dysfunction and cell death. Current estimates indicate that the pathological changes occur up to 10-20 years before onset of clinical symptoms <sup>2,3</sup>. Eventually, the progressive loss of neuronal connections and neurons themselves manifests in cognitive deterioration, loss of memory, and gradual impairment in activities of daily living<sup>4</sup>. In the final stages of the disease, all cognitive functions are severely impaired, and the patient becomes completely dependent on palliative care. As death eventually occurs, in most cases this is thought to stem from medical complications not directly related to AD in itself, such as infections, often including pneumonia <sup>4,5</sup>.

According to estimates from the World Health Organization (WHO), dementia will affect 75 million people worldwide by 2030, and is estimated to increase to 132 million by 2050 <sup>6</sup>. The WHO also projects that by 2030, global cost of caring for people suffering from dementia will have risen to US\$ 2 trillion, a cost that potentially could undermine social and economic development worldwide and overwhelm health and social services<sup>6</sup>. The WHO has specifically called for the prevention of dementia as being made a public health priority, and to this end medical research and innovation is crucial.

### *1.1.1 Historical overview of Alzheimer's disease research*

The disease now known as AD was first systematically studied by, and later named after, the German psychiatrist and neuropathologist Alois Alzheimer. In November 1901, a middle-aged woman by the name of Auguste Deter was admitted to the Frankfurt Psychiatric Hospital with symptoms consisting of memory disturbances, paranoia, and progressive

confusion. In 1906, after four and half years in the institution, Auguste Deter succumbed to her illness<sup>7-9</sup>. Upon post-mortem examination of her brain, Alzheimer observed and described an atrophic brain, miliary foci caused by deposition of a peculiar substance in the cortex, and tangled bundles of fibrils remaining where once neurons



**Figure 1** Left: Alois Alzheimer photographed in Berlin. Right: Auguste Deter at 51 years old. Pictures taken from <https://www.alzforum.org/timeline/alzheimers-disease>

had been located<sup>10</sup>. Alzheimer presented the case of Auguste Deter in 1906 to a disinterested audience at a scientific congress of German psychiatrists in Tübingen, and published his findings one year later<sup>7, 8, 11</sup>. Emil Kraeplin, a prominent German psychiatrist, and senior colleague and mentor of Alzheimer understood the fundamental significance of Alzheimer's findings. Thus, the diagnostic term *Alzheimer's disease* was introduced on Kraeplin's authority with the inclusion of the case report of Auguste Deter in the 8<sup>th</sup> edition of his textbook *Psychiatrie*<sup>11, 12</sup>.

Despite AD being recognized as a defined illness by Kraeplin in 1910, the scientific interest in the disease remained modest at best. AD saw renewed scientific interest in the 1960s, when electron microscopy revealed that the tangles of fibrils described by Alzheimer were made up of paired helical filaments (PHF)<sup>13</sup>. A few years later, Blessed, Roth and Tomlinson published a series of histopathological studies of patients with senile dementia. In these publications, the authors revealed high correlations between plaque counts, neurofibrillary change and cortical atrophy found in post-mortem examinations with high scores for dementia and low psychological functioning<sup>14-18</sup>. These publications pointed to AD, then considered a rare presenile dementia, to be a leading cause of dementia.



**Figure 2** Alzheimer's own drawings of fibrillary changes in ganglion cells stained by Bielschowsky silver staining. (A) Onset of the disease. (B) Advanced disease. (C) Final condition of the disease. Pictures taken from Alzheimer <sup>19</sup>

Essential breakthroughs in AD research came in the 1980s, first with the purification and characterization of the amyloid protein that forms the pathological plaque cores seen in AD. Amino acid sequencing of this protein identified a unique 40-42 peptide sequence which we now refer to as amyloid- $\beta$  ( $A\beta$ ) <sup>20-22</sup>. Then, researchers discovered a specific cellular pattern of pathology affecting the major input and output pathways to the hippocampal formation, a structure crucial to memory. By examining medial temporal lobe structures from AD patients, researchers observed that projection neurons found in layers (L) II and IV of the entorhinal cortex (EC) were especially damaged, effectively isolating the hippocampal formation <sup>23</sup>. Also came the discovery that the PHF polypeptides seen in tangled fibrils were labeled by antibodies specific for microtubule associated protein tau <sup>24</sup>. Subsequent research revealed that the tau protein found in AD brains were abnormally phosphorylated. This lead researchers to the conclusion that phosphorylation of tau protein is a key step in the formation of PHF seen in AD-neurons <sup>25-27</sup>

## **1.2 Anatomy of the hippocampal formation and parahippocampal region**

Our memory functions relies heavily on the hippocampal formation and surrounding medial temporal lobe, and disruption of episodic memory is one of the earliest and most prominent cognitive impairments in AD <sup>28, 29</sup>. The hippocampal formation is a three-layered cortex and consists of the following regions in the rodent brain: the dentate gyrus, the hippocampus proper (cornu ammonis (CA) fields 1-3) and the subiculum <sup>30</sup>. The parahippocampal region consist of the six layered cortical regions: EC, the perirhinal- and the postrhinal cortex (Figure 4 A-B)<sup>31</sup>

### 1.2.1 The entorhinal cortex

EC is most commonly divided into two subregions based on differences in cytoarchitecture: the lateral entorhinal cortex (LEC), and the medial entorhinal cortex (MEC)<sup>33</sup>. The two main subregions can be further subdivided in rodents, where LEC includes the dorsolateral- (DLE), dorsal intermediate- (DIE) and ventral intermediate- (VIE) entorhinal areas, whereas MEC includes the medial (ME) and caudal (CE) entorhinal areas<sup>34, 35</sup>.

#### 1.2.1.1 Entorhinal-hippocampal connectivity through the perforant path

EC is a major cortico-hippocampal relay point, receiving uni- and multimodal inputs from much of the neocortex, and in turn EC projects massively to the hippocampal formation. Traditionally two parallel projection input streams to EC have been described, where perirhinal cortex projects non-spatial information to the LEC, while the postrhinal cortex projects visuospatial information to the MEC<sup>31</sup>. However, recent evidence challenges this model by demonstrating that all main principal neurons in LEC LII receive convergent inputs from perirhinal and postrhinal cortices, making LEC LII the main multimodal integration structure<sup>36</sup>. *The perforant path* provides a connectional route from EC to all subregions of the hippocampal formation<sup>31, 37</sup>. The perforant path includes neurons in EC LII projecting to the dentate gyrus and CA3, and neurons in LIII projecting to CA1 and the subiculum via the temporoammonic pathway. The trisynaptic pathway continues from the dentate gyrus to CA3 through *the mossy fiber pathway*, from CA3 to CA1 via the *Schaffer collaterals*. CA1 and subiculum also relay projections back to the deep layers of EC (Figure 4C)<sup>31, 37, 38</sup>.

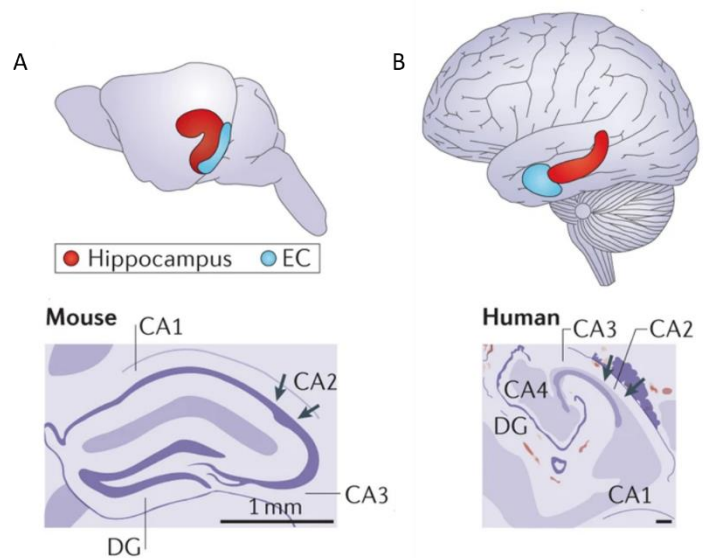


**Figure 3** The full long axis of the hippocampal formation (red) with the entorhinal cortex (blue) in the rodent (A) and human (B) brain. Illustrations of Nissl coronal sections with of the hippocampus. DG = dentate gyrus, CA = cornu ammonis fields. Figure adapted from Strange, Witter<sup>32</sup>

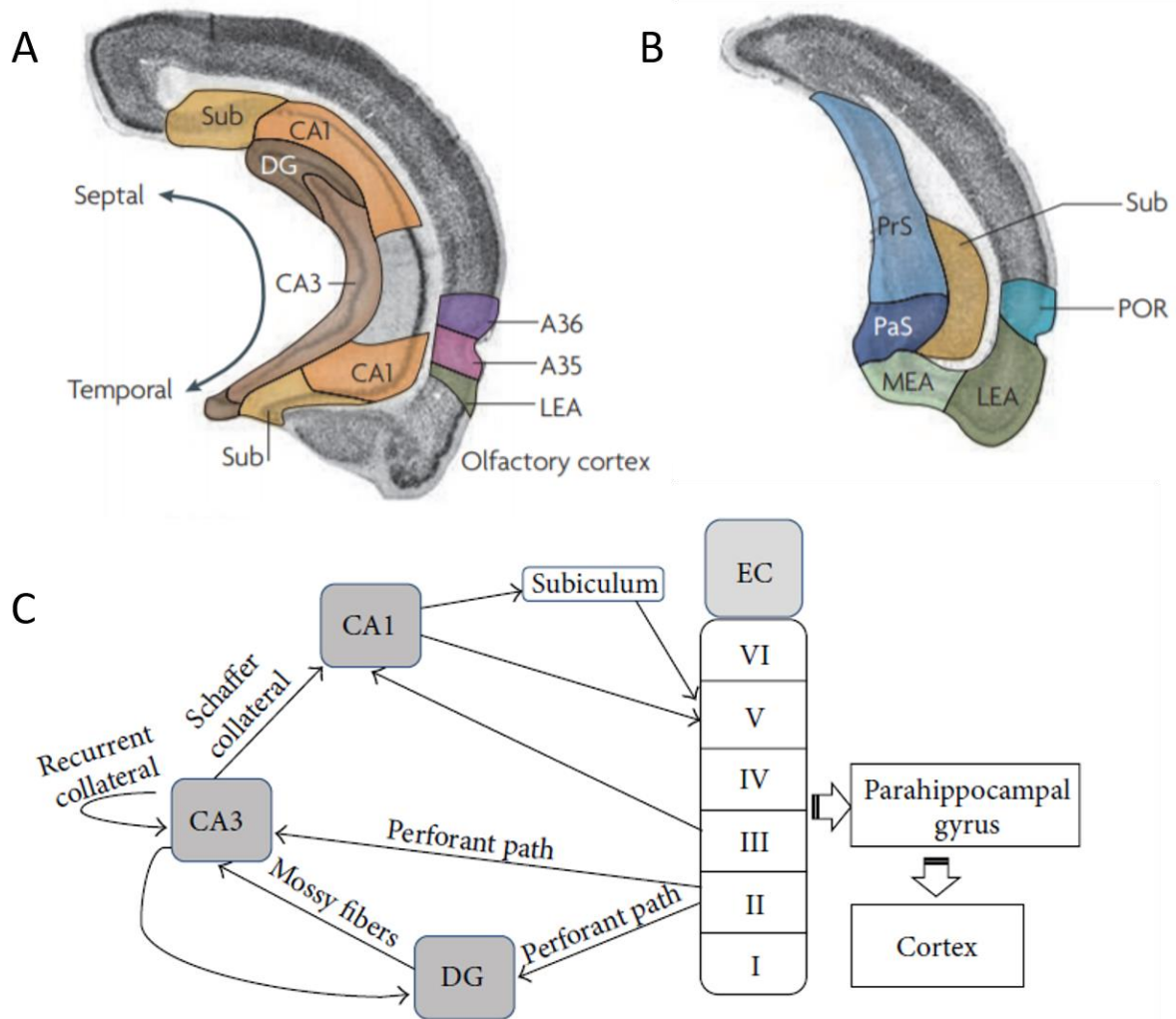


**Figure 4** (A-B) The areas of the hippocampal formation and parahippocampal region in the rodent brain shown in two coronal sections, mid-rostrocaudal (A) and caudal (B). (C) A diagram illustrating the entorhinal-hippocampal connectivity. The perforant path arises from EC LII and projects both to the dentate gyrus (DG) and CA3. Sub = subiculum, A35/36 = perirhinal cortex Brodmann's area 35/36, LEA = lateral entorhinal cortex, MEA = medial entorhinal cortex, POR = postrhinal cortex, Prs = Presubiculum, PaS = parasubiculum. Figure (A-B) adapted from van Strien, Cappaert<sup>39</sup>, figure (C) adapted from Yau, Li<sup>38</sup>

### 1.2.1.2 Cell types in layer II of the entorhinal cortex

In MEC, roughly 50% of the cells are stellate cells, while the majority of cells in LEC are fan cells. Additionally, multiform cells can be found in LEC, but not in MEC<sup>31</sup>. Also, both LEC and MEC LII contains pyramidal and pyramidal like neurons<sup>31</sup>. Most of the stellate and fan cells are reelin (RE)-positive and give rise to projections to the dentate gyrus and CA3<sup>40, 41</sup>. If one follows the original definition of Cajal and Lorente de N6, one must conclude that LEC LII is largely devoid of calbindin-positive cells, unlike MEC<sup>40, 42, 43</sup>. The alternative delineation places the border between LII and LIII at a deeper position. This splits the dorsal part of LEC into two sublayers, where the outermost layer, referred to as LIIa, contains the

fan cells characteristic of LEC, while the inner sublayer, LIIB, includes a sizable portion of calbindin-positive neurons. Conversely, MEC LII contains calbindin-positive neurons, which are grouped in clusters<sup>40</sup>. MEC will contain calbindin-positive neurons regardless of which of the two delineation schemes used with respect to placement of the LII/LIII border. Calbindin-positive neurons in MEC and LEC provide a wide range of extrinsic projections, including to CA1 and extra-hippocampal areas, as well as providing local excitatory projections within and between MEC and LEC<sup>41</sup>

### 1.3 Neuropathology of Alzheimer's disease

#### 1.3.1 Neuropathological hallmarks

The two primary neuropathological hallmarks enabling post-mortem verification of AD are the same as Alzheimer described over 100 years ago. These hallmarks are referred to as amyloid plaques, and neurofibrillary tangles (NFTs)<sup>44</sup>. Another main characteristic of later stages of AD is massive neuronal loss, especially in the limbic and association cortices, leading to gross atrophy of the brain<sup>45</sup>. Also seen in AD as a consequence of progressive neuropathology, is widespread synaptic dysfunction, oxidative stress and markers of neuroinflammation<sup>46-50</sup>. The primary focus of this thesis is on the tau-related pathology of AD, however, a brief consideration of amyloid pathology and brain atrophy will be provided, as it is relevant when

considering the disease as a whole and when discussing the events that might lead up to tau-specific changes.

#### 1.3.2 Brain atrophy

Brain atrophy caused by synaptic loss and neuronal death is a prominent pathological feature of AD. A symmetrical pattern of cortical atrophy, including widening of the sulci and enlarged ventricles are visible when comparing the brains of AD-patients with

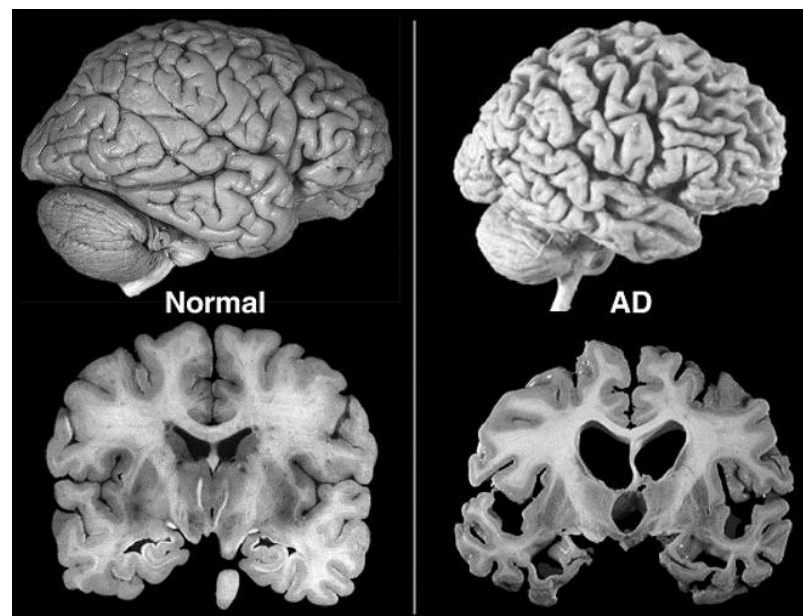


**Figure 5** Brain atrophy in advanced Alzheimer's disease (AD). Left: Healthy aged subject. Right: the brain of a patient in late-stage AD. Take note of the severely enlarged ventricles, the shrinkage of the cerebral cortex and the extreme shrinkage of the hippocampus and entorhinal cortex. Figure adapted from Bagad, Chowdhury & Khan<sup>51</sup>

healthy controls. Cortical atrophy occurs early in the medial temporal lobe, and soon after spreads to the remainder of the cortex with a temporal-parietal-frontal trajectory, while atrophy in motor area occurs in the late disease stages<sup>52, 53</sup>. Atrophy in the hippocampus is prominent in AD and the hippocampal atrophy rate is strong predictor of mild cognitive impairment (MCI)<sup>54</sup>. The reduction in hippocampal volume occurs early and progresses throughout the disease. It also correlates well with Braak staging and neuronal counts in dementia<sup>52</sup>. The EC is one of the earliest regions where neuronal loss is apparent<sup>55</sup>. Atrophy in the EC is dramatic and affects individual lamina differently. LII, which gives rise to the perforant path to the hippocampus, and LIV which receives major hippocampal efferent projection, are especially affected. Patients diagnosed with MCI, have a reduction in LII neurons of around 60%, as well as a near 25% reduction in neuronal volume compared to controls, while LIV has a neuronal loss of 40%<sup>56, 57</sup>.

### 1.3.3. Amyloid plaques

A $\beta$  peptides are derived by proteolysis of a larger transmembrane glycoprotein known as amyloid precursor protein (APP). Sequential cleavage of the APP protein can follow two distinct pathways; the *non-amyloidogenic pathway*, which prevents generation of A $\beta$ , or the *amyloidogenic pathway*, which results in the formation of A $\beta$  (Figure 6)<sup>58</sup>.

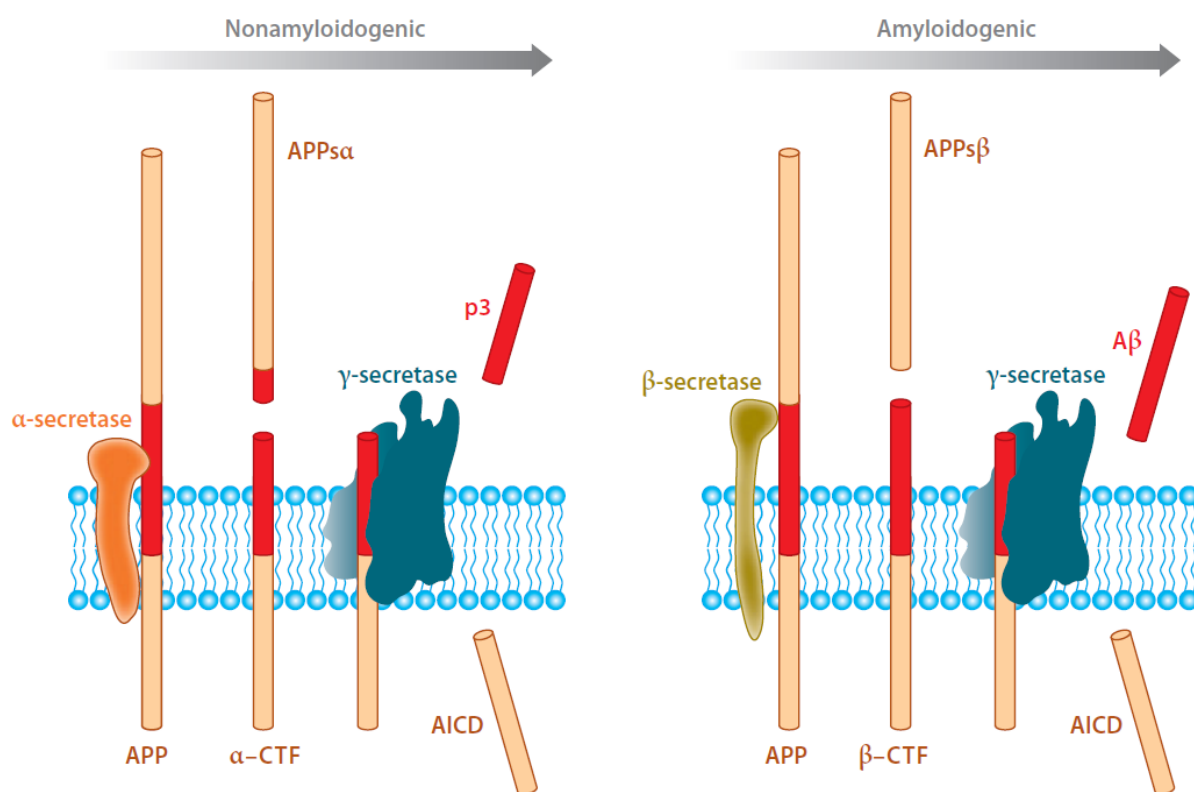


**Figure 6** Visualization of the two pathways of processing amyloid precursor protein (APP). In the non-amyloidogenic pathway, APP is first processed by  $\alpha$ -secretase resulting in the soluble ectodomain APPs $\alpha$  and 83 amino acid long C-terminus fragment ( $\alpha$ -CTF). Subsequent cleavage of  $\alpha$ -CTF by  $\gamma$ -secretase yields extracellular p3 and the APP intracellular domain (AICD). In the amyloidogenic pathway, APP is first processed by  $\beta$ -secretase, resulting in the soluble ectodomain APPs $\beta$  and the 99 amino acid long  $\beta$ -CTF. Subsequent cleavage of  $\beta$ -CTF by  $\gamma$ -secretase creates AICD and extracellular amyloid- $\beta$  (A $\beta$ ). Figure has been adapted from O'Brien and Wong<sup>59</sup>.

Processing of APP in healthy neurons mainly follow the non-amyloidogenic pathway, where APP is cleaved approximately in the middle of the A $\beta$  region by  $\alpha$ -secretase. This generates a C-terminus fragment ( $\alpha$ -CTF) 83 amino acids in length and the soluble ectodomain APPs $\alpha$ , which is shed into the extracellular medium. The  $\alpha$ -CTF is subsequently cleaved by  $\gamma$ -secretase, resulting in a truncated peptide called p3 being released into the extracellular medium and the APP intracellular domain (AICD)<sup>58</sup>. In contrast, the amyloidogenic pathway processes APP by an initial cleavage by  $\beta$ -secretase (also known as BACE1), generating a longer 99 amino acid C-terminus fragment ( $\beta$ -CTF) as well as a soluble ectodomain APPs $\beta$ . The  $\beta$ -CTF is subsequently cleaved by  $\gamma$ -secretase. This also generates an AICD, but more importantly, it also generates A $\beta$ . Depending on variabilities in the cleavage by  $\gamma$ -secretase, A $\beta$  can vary in length from 39 to 43 amino acids<sup>60</sup>. Of these different isoforms, the 40-isoform of A $\beta$  (A $\beta$ <sub>40</sub>) is the most abundant<sup>61</sup>. Of particular interest, is the -42 isoform (A $\beta$ <sub>42</sub>), which has been shown to be prone to self-aggregation into non-soluble neurotoxic oligomers and is more abundant in AD brain tissue compared to age-matched controls<sup>62-64</sup>. By misfolding and self-aggregation, the A $\beta$  peptide will undergo conformational changes, transforming from smaller soluble monomer and oligomer fragments, into larger insoluble fibrils, eventually becoming amyloid plaques<sup>61, 65</sup> (Figure 7). The extracellular amyloid deposits can appear in different morphological types, including *dense core plaques* and *diffuse plaques*. Dense-core plaques, also referred to as senile plaques or neuritic plaques, consist of a fibrillar amyloid core, and are often linked to dystrophic neurites, activated microglia and reactive astrocytes. Diffuse plaques are amorphous deposits of A $\beta$  with a finely granular pattern, but lacks a compacted fibrillar core<sup>66, 67</sup>.

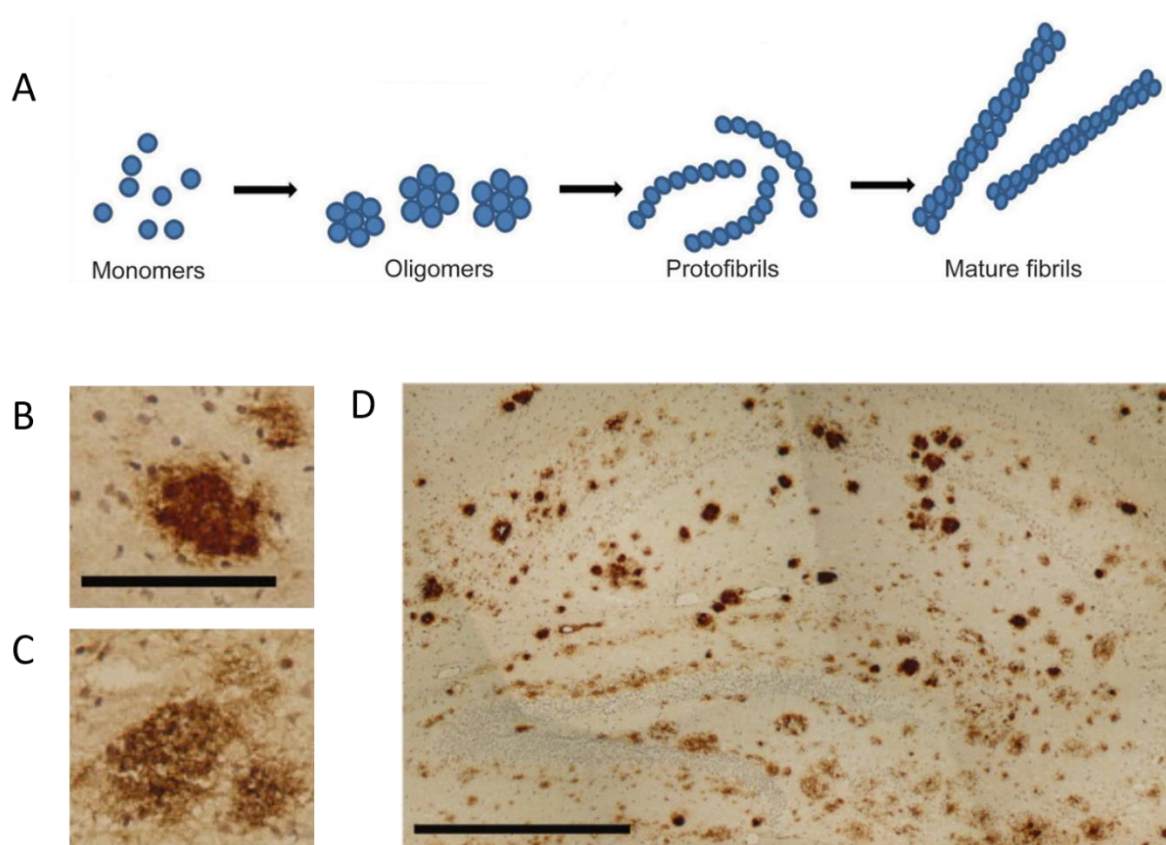


**Figure 7** Amyloid- $\beta$  ( $A\beta$ ) oligomerization and  $A\beta$  plaques. (A) Visual representation for the conversion of  $A\beta$  monomers to higher order oligomers, protofibrils and fibrils. Adapted from Chen et al.<sup>68</sup>. (B-D) Immunostaining of amyloid plaques in a 14-month-old APP transgenic mouse (*TgCRND8*) with anti- $A\beta$  antibody 4G8 and visualized with 3,3'diaminobenzidine (DAB) (B) Dense-core plaque in the hippocampus. (C) Diffuse plaque in the caudate. (D) Overview of amyloid plaques in the hippocampus. Scale bar = 100 $\mu$ m for (B-C) and 500 $\mu$ m for (D). Pictures adapted from Rak et al.<sup>66</sup>

### 1.3.3.1 Amyloid cascade hypothesis

The amyloid cascade hypothesis states that deposition of  $A\beta$  is the causative pathological agent in AD and that amyloidogenic processing of APP precedes the formation of NFTs. A disruption in the production- and clearance of  $A\beta$ , resulting in increased levels of  $A\beta_{42}$ , is thought to initiate a series of pathogenic events, including formation of p-Tau and NFT, and ultimately synaptic and neuronal dysfunction<sup>69, 70</sup>. Genetic evidence in favor of the hypothesis comes from studies of humans with Down syndrome, who develop neuropathology indistinguishable from AD. Due to trisomy of chromosome 21, persons with Down syndrome have three copies of the APP gene, which researchers claim to be a causal factor in the AD neuropathology observed Down syndrome. Individuals with Down syndrome show abundant diffuse  $A\beta$  plaques, microgliosis and NFT accumulation already in the early-to-mid teens<sup>69, 71</sup>. Also, the majority of cases of familial AD, are caused by mutations in the catalytic subunits of  $\gamma$ -secretase, presenilin 1 and 2 (PS1/2), which result increase in the ratio of  $A\beta_{42}$  produced to  $A\beta_{40}$ <sup>72, 73</sup>. Although accumulation of  $A\beta$  plaques has a low correlation with cognitive decline, intracellular  $A\beta$  correlates strongly with cognitive decline<sup>74, 75</sup>.

Intracellular A $\beta$ <sub>42</sub> is reported to accumulate in EC LII, a region associated with early accumulation of tau pathology, prior to NFT and A $\beta$  plaque deposition<sup>76, 77</sup>.

## 1.4 Tau protein and neurofibrillary tangles

### 1.4.1 Tau protein

Tau protein, also commonly referred to as microtubule-associated protein tau (MAPT), was initially discovered in 1975<sup>78</sup>. Much of AD research has been devoted to the study of tau protein since the breakthrough discovery in 1986 that abnormally phosphorylated tau is the major component of the PHFs that make up NFTs<sup>24-27</sup>. Dysfunction of tau protein is not a unique pathological feature of AD. Aggregation of tau is the primary pathological feature of a wide range of neurodegenerative disorders, collectively termed *tauopathies*. These include, but are not limited to, frontotemporal dementia and parkinsonism linked to chromosome 17, Pick's disease, chronic traumatic encephalopathy, progressive supranuclear palsy, argyrophilic grain disease, and corticobasal degeneration<sup>79, 80</sup>

In healthy neurons, tau acts mainly as a stabilizing molecule on axonal microtubules. Microtubules are protein polymers of the cytoskeleton, tasked with stabilizing cell shape, aiding mitosis, and serve as tracks for intracellular transport by motor proteins like kinesin and dynein. The main function of tau is to stabilize the microtubules by binding to the microtubule surface and promote their self-assembly from tubulin subunits<sup>81</sup>. As a phosphoprotein, the functions of tau are regulated by phosphorylation, which reduces its ability to bind to microtubules<sup>82</sup>.

### 1.4.2 Tau structure

Tau protein can be divided into two parts based on functionality: the microtubule binding domain towards the C-terminus, and the projection domain towards the N-terminus. The microtubule binding domain has four imperfectly repeated motifs, separated by flanking regions, which together provides the structure by which tau binds and stabilizes microtubules<sup>83</sup>. Upon binding, the N-terminal projection domain protrudes away from the microtubule. This enables regulation of microtubule dynamics by providing spacing between microtubules and other cell components<sup>84</sup>. The MAPT gene located on chromosome 17q21 encodes the tau protein, and combinations of alternative splicing of exons 2, 3 and 10 gives rise to six different isoforms of tau in the human brain. Having zero, one or two N-terminal inserts (0N,

1N and 2N), in combination with either three (3R) or four (4R) repeat regions in the microtubule binding domain determines the isoform (Figure 8) <sup>85, 86</sup>.

Tau expression is developmentally regulated, such as in the fetal brain, only the shortest isoform (0N3R) of tau is expressed, whereas in the adult human brain, all six isoforms are present with equal amounts of the 3R and 4R tau isoforms <sup>83</sup>. However, this is not the case in the murine brain. Although the 0N3R isoform is briefly present in fetal wild type (WT) mice, the predominant isoform quickly changes to the point where only 4R tau is expressed in the adult mouse brain, with the 0N4R being the predominant isoform <sup>87-90</sup>. The adult rat brain contains all six tau isoforms like the human brain, however, the expression of 4R tau isoforms are nine-fold higher than 3R isoforms <sup>91</sup>.

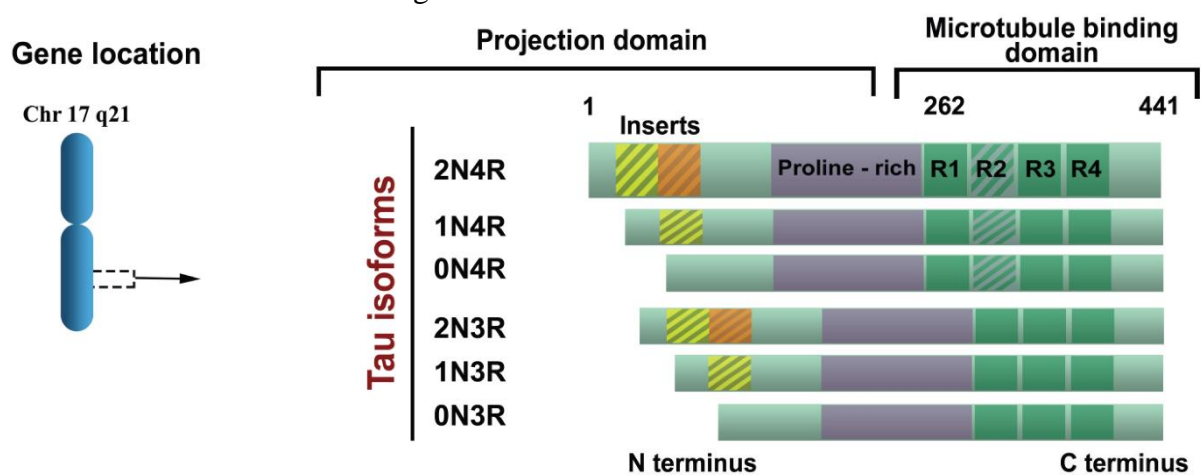


**Figure 8** MAPT gene chromosomal location and all six isoforms of tau protein by alternative splicing of exons 2,3 and 10. Different tau isoforms occur as a result of the absence or presence of one or two N-terminal inserts encoded by exon 2 (yellow) and 3 (orange), in combination with the presence or absence of the R2 repeat encoded by exon 10. Figure adapted from Šimić et al <sup>85</sup>

### 1.4.3 Tau hyperphosphorylation

Under pathological conditions, tau protein can become excessively phosphorylated, a process which is called hyperphosphorylation. The level of phosphorylated tau protein in autopsied AD brains have been reported to be three- to four-fold higher than in healthy controls <sup>92</sup>. Approximately 45 phosphorylation sites have been identified in tau protein isolated from the AD brain <sup>85, 93, 94</sup>. Hyperphosphorylated tau (p-Tau) undergoes conformational changes that makes tau lose its ability to bind to and stabilize microtubules. This leads to microtubule depolymerization, eventually resulting in disruption of intracellular axonal transport and degeneration of axons <sup>95, 96</sup>. Detached tau accumulates in the somatodendritic compartment of the affected neuron, and will start to self-aggregate into higher order oligomers <sup>97, 98</sup>. These aggregates form the PHFs, which are made up of paired

fibrils, alternating 8nm and 20nm in width, wound in a helical fashion with a regular periodicity of 80 nm. The PHFs make up the principal component of the NFTs.<sup>13, 81, 99</sup> A secondary structural variant of PHFs, also made from p-tau subunits, are straight filaments, which are also found in NFTs. The straight filaments are slightly smaller with a width of 15 nm, and does not exhibit the modulation in width seen in PHFs<sup>100, 101</sup> (Figure 9).

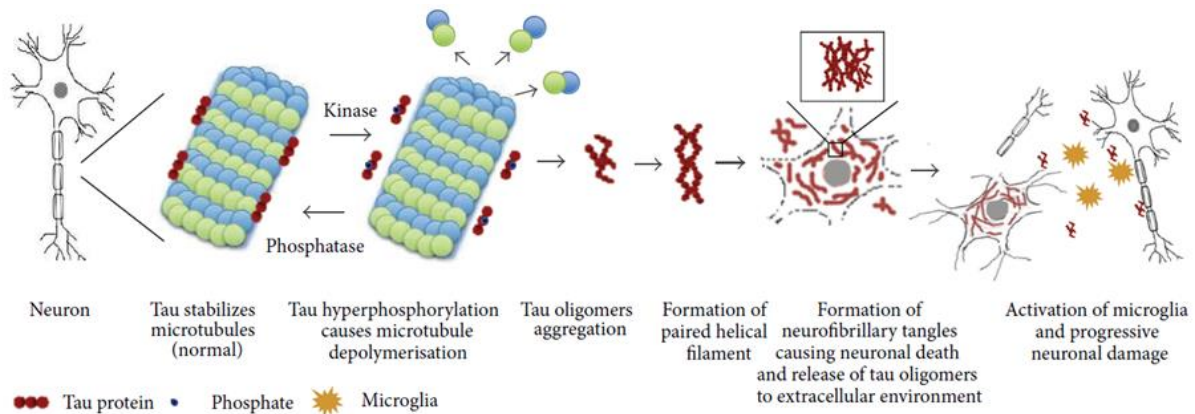


**Figure 9** Visual representation of tau-pathological cascade. Microtubule stabilization by tau protein is regulated by phosphatases and kinases. Under pathological conditions, tau protein becomes hyperphosphorylated (p-tau) and detaches from microtubules and form cytoplasmic tau oligomers, which eventually form paired helical filaments (PHFs). The PHF assemble to produce neurofibrillary tangles (NFT), eventually leading to neuronal death and the release of NFTs into the extracellular medium. Figure adapted from Mokhtar et al.<sup>102</sup>

Dense arrays of PHFs will ultimately aggregate into its final state of NFTs, and prolonged dysfunction of neuronal processes will lead to neuronal death. NFTs and neuropil threads of PHFs and straight filaments are then released into the extracellular space, triggering microglial activation<sup>103-105</sup>. P-Tau is also found extracellularly in dystrophic neurites and in neuritic A $\beta$  plaques<sup>96, 106</sup>.

#### 1.4.4 Tau pathology in the Alzheimer's disease brain

The pattern in cortical atrophy, as well as the degree of clinical dementia correlates well with the NFT spread, suggesting that NFT pathology has some direct impact on brain function<sup>57, 108, 109</sup>.

Initial tau pathological changes occur in the parts of EC located towards the collateral sulcus, i.e. laterally, in what is sometimes called the transentorhinal region (TR)<sup>110-114</sup>. Progression of NFT pathology in AD follows a well-established regional pattern, defined in the so-called Braak stages. Stages I and II are called the transentorhinal stages, where tau pathology first appears in LII-neurons in the part of EC located

towards the collateral sulcus. In stage III-IV, NFT pathology increases in EC LII, while it also appears in the hippocampus. By stages V-VI, NFTs have spread to all neocortical association areas, as well as primary sensory areas such as the striate cortex<sup>110, 111, 115, 116</sup>. Throughout the stages, there is a continuous increase of NFTs in those areas already affected.

#### 1.4.5 Tau protein kinases

Microtubule function is regulated by phosphorylation and dephosphorylation of tau protein. In healthy neurons this demands a balance between the *kinases*, which adds a phosphate group, and the *phosphatases*, which removes a phosphate group. Disruption of this equilibrium by an increase in kinase activity is thought to be a key step in the tau-pathological cascade. Tau specific kinases can be divided into three groups, proline-directed kinases (PDPK), non-PDPK, and tyrosine (Tyr) kinases<sup>117</sup>. PDPK phosphorylate the serine (Ser) and threonine (Thr) residues on tau. The kinases glycogen synthase kinase 3 $\beta$  (GSK3 $\beta$ ) and

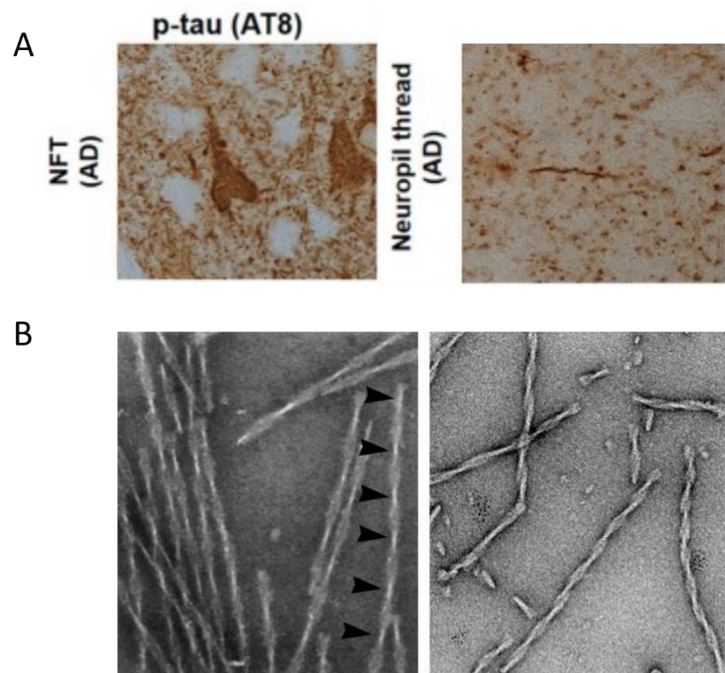


**Figure 10** (A) Immunostaining of neurofibrillary tangles (NFT) and neuropil threads in human Alzheimer's disease (AD) brain using AT8 antibody visualized with 3,3' diaminobenzidine (DAB). Pictures from Kurihara et al.<sup>107</sup> (B) Electron micrographs of paired helical filaments (PHF). Left: PHF isolated from an AD brain, with 80nm crossover repeats (arrowheads). Right: PHF assembled in vitro from recombinant tau. Pictures from Mandelkow & Mandelkow<sup>101</sup>

cyclin-dependent protein kinase-5 (CDK5) belong to this group of kinases, and have been extensively studied in relation to tau pathology in AD.

GSK3 exists in two different isoforms: GSK3 $\alpha$  and GSK3 $\beta$  <sup>118, 119</sup>. GSK3 $\beta$  regulates multiple cellular functions, including gene expression, cell proliferation, neural development and plasticity <sup>120</sup>. Formerly known as tau protein kinase I, GSK3 $\beta$  also induces abnormal phosphorylation of tau and promotes assembly of PHFs seen in AD <sup>120-122</sup>. GSK3 $\beta$  is a constitutively active kinase, however, its activity is modulated by phosphorylation at specific residues. The activity of GSK3 $\beta$  is significantly downregulated by phosphorylation at the Ser9 residue, while its activity is upregulated by phosphorylation on the Tyr216 residue <sup>123</sup>. Multiple AD-related residues on tau protein are phosphorylated by GSK3 $\beta$  activity, among which are Ser199, Thr205 and Ser396 <sup>93, 124-127</sup>. Interplay between GSK3 $\beta$  and additional kinases have previously been reported to increase the scope of tau phosphorylation by GSK3 $\beta$ . For instance, pre-phosphorylation of tau by the non-PDPK A-kinase, allows GSK3 $\beta$  to phosphorylate residues on tau that GSK3 $\beta$  normally does not have access to <sup>125, 126</sup>. Also, tau phosphorylation by PDPKs aren't mutually exclusive, as it has been demonstrated that pre-phosphorylation of tau by CDK5 stimulated both the rate and extent of subsequent phosphorylation of GSK3 $\beta$  <sup>128</sup>.

## 1.5 Reelin

### 1.5.1 Reelin function in neurodevelopment and in the healthy brain

Reelin (RE) is a large extracellular glycoprotein which plays a key role in neurodevelopment by regulating neuronal migration, thereby aiding corticogenesis and neuronal lamination. During neuronal development, Cajal-Retzius cells in the marginal zone secrete RE, postmitotic cells cell migrate along radial glial cells to form the cortical plate and subplate via the RE-pathway <sup>129, 130</sup>. The importance of RE becomes particularly evident in the RE-deficient *reeler* mouse model, where cortical lamination is severely disrupted in homozygous animals <sup>131-133</sup>. RE also plays a role in adult synaptic plasticity by interacting with the lipoprotein receptors ApoE receptor 2 (ApoER2) and the very low-density lipoprotein receptor (VLDLR). Long-term potentiation (LTP), which is a process considered to be the basis of memory formation, was demonstrably reduced in VLDLR-deficient mice, and profoundly reduced in ApoER2-deficient mice. Also, RE significantly augmented LTP induction in hippocampal slices from WT-mice, but not in slices from either VLDLR- or

ApoE2-deficient animals <sup>134</sup>. Binding of RE to ApoER2 and VLDLR at the postsynapse also modulates neurotransmission through N-methyl-D-aspartate receptor (NMDAR). This elevates levels of intracellular calcium, leading to downstream effects including enhanced LTP, increased synaptic plasticity, neurite growth and dendritic spine development (Figure 11) <sup>135, 136</sup>.

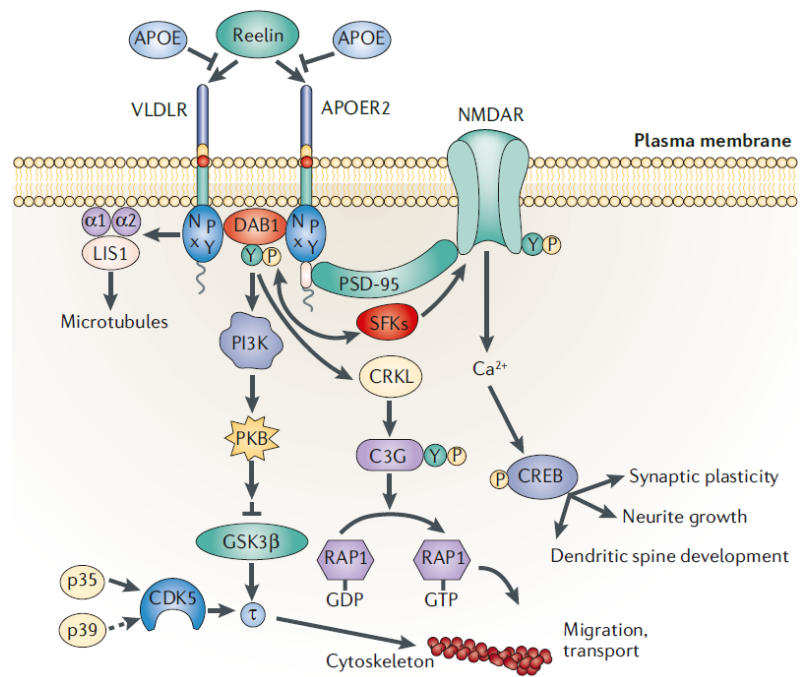


**Figure 11** Schematic of intracellular signaling as a result of reelin (RE) binding to very low-density lipoprotein receptor (VLDLR) and ApoE receptor 2 (ApoER2). RE binding to VLDLR/ApoER2 potentiates N-methyl-D-aspartate (NMDA) influx of calcium (Ca<sup>2+</sup>), leading to downstream effects increasing synaptic plasticity, neurite growth, and dendritic spine development. RE binding to VLDLR/ApoER2 also initiates intracellular signaling leading to inhibition of glycogen synthase kinase 3β (GSK3β) by phosphorylating Ser9, thus preventing tau hyperphosphorylation and microtubule destabilization. Figure adapted from Herz & Chen <sup>136</sup>

RE binding to ApoER2 and VLDLR receptor also promotes microtubule stabilization by activating an intracellular cascade through the cytoplasmic adapter protein disabled 1 (DAB1) inhibiting GSK3β activity by phosphorylating Ser9, ultimately preventing tau hyperphosphorylation and microtubule destabilization (Figure 11) <sup>136, 137</sup>.

### 1.5.2 Reelin in Alzheimer's disease

As previously mentioned, EC LII neurons are especially implicated in the early development of AD regarding early onset of p-Tau accumulation and neuronal loss. RE in the rodent brain is abundantly expressed in LII of both LEC and MEC. RE expression is strongest in neurons close to the rhinal fissure, and there is a gradual reduction in RE expression when moving further away from the rhinal sulcus until only a small amount is present in the most venteromedial parts of EC <sup>138</sup>. Recent evidence indicates that RE-positive neurons in EC LII are particularly vulnerable to the accumulation of intracellular Aβ. In EC, similar to the expression of RE, the accumulation of intracellular Aβ also follows a topographical gradient, with levels of intracellular Aβ being strongest near the rhinal fissure <sup>138</sup>. A study of RE levels in EC in transgenic mice expressing human APP, RE levels were significantly reduced in EC

projection neurons in comparison to non-transgenic controls, suggesting that A $\beta$  can reduce levels of RE in EC <sup>139</sup>. Interestingly, the expression pattern of intracellular A $\beta$  and RE is strikingly similar to the expression pattern of early NFT accumulation described by Braak & Braak <sup>110</sup>. Age-related reduction of RE-expressing neurons in LEC LII in rats has been shown to be associated with cognitive decline, as well as increased accumulation of p-Tau <sup>140, 141</sup>. In reeler mice, as well as mice deficient in VLDLR/ApoE2, levels of GSK3 $\beta$  and p-Tau has been shown to be dramatically increased, suggesting that accumulation of p-Tau could be related to RE dysfunction in the DAB1 signaling pathway <sup>142, 143</sup>.

The observed prodromal accumulation of intracellular A $\beta$  in RE-positive neurons in EC, which happens to be the same neurons implicated in the onset of tau-pathological changes, might suggest some form of interaction between RE and intracellular A $\beta$ , resulting in the initiation of tau pathology. As previously mentioned, RE is indirectly regulating tau-phosphorylation by promoting GSK3 $\beta$  inactivity by phosphorylation of its Ser9 residue. Reduced levels of RE would potentially lead to less inhibition of GSK3 $\beta$ , resulting in p-Tau formation <sup>144</sup>. Interaction between intracellular A $\beta$  and RE that results in disrupted RE signaling, might be a molecular mechanism that initiates NFT pathology in EC LII.

## **1.6 Transgenic animal models of Alzheimer's disease**

### *1.6.1 APP/PS1 mouse*

First developed and published in 2006 by R. Radde and her team at the Hertie-Institute for Clinical Brain Research in Germany, the APP/PS1 is a transgenic mouse model for AD on a C57BL/6J genetic background that co-express transgenes for human APP Swedish double mutation (KM670/671NL) and PSEN1 containing the L166P mutation. Both transgenes are controlled by a neuron specific Thy1 promoter element <sup>106</sup>.

Initial A $\beta$  plaques are detectable in the neocortex of the APP/PS1 at 6 weeks postnatally. As the disease progresses, amyloid deposits appear in the hippocampus at 3-4 months of age, and in becomes apparent in the striatum, thalamus, and the brain stem after 4-5 months. After 8 months, A $\beta$  plaques are present throughout the forebrain <sup>106</sup>. At 8 months, the A $\beta$  plaques were surrounded by hyperphosphorylated tau-positive neuritic processes detectable by AT8 immunostaining. However, no fibrillar tau inclusions or tangle formation has been observed in the APP/PS1. Levels of total tau concentration in CSF does increase at 6 months, and reach a 5-fold increase by 18 months of age<sup>145</sup>. The APP/PS1 displayed a

significant impairment in reversal learning compared to age-matched littermate controls by 8 months of age<sup>106</sup>. There were no registered statistical differences in A $\beta$  pathology between male and female APP/PS1 mice in the initial publishing<sup>106</sup>.

### 1.6.2 *3xTG mouse*

Developed by S. Oddo and his team at University of California, Irvine and published in 2003, the triple-transgenic (3xTG) AD model is a widely used mouse model in AD research and is known for developing both A $\beta$  plaques and NFT pathology<sup>146</sup>. This model was developed by co-microinjecting two independent transgenes encoding for human APP with the Swedish double mutation (K670N/M671L) and the human MAPT P301L mutation, both under control of the Thy 1.2 promoter, into single-cell embryos harvested from homozygous mutant PSEN1 M146V knock-in mice with a C57BL/6 genetic background.

The earliest detectable neuropathological changes in the 3xTG mouse are the intracellular accumulation of A $\beta$  peptides in the neocortex. This occurs by 3 to 4 months of age in both homo- and heterogeneous genotypes and precedes any detectable extracellular A $\beta$  pathology<sup>146, 147</sup>. Extracellular accumulation of A $\beta$  is first apparent in 6-month-old homozygous mice, mainly in the frontal cortex LIV-V and senile plaques can be identified in the neocortex and the hippocampal areas by 12-15 months<sup>146, 147</sup>. Tau-specific pathology, including phosphorylation at the epitopes S202/Thr205, was first detectable at 12 months in the CA1 subfield of the hippocampus, particularly in pyramidal neurons. Phosphorylation at epitopes Ser396/Ser404 became evident at 18 months of age<sup>146</sup>. This differs from the human AD brain, where first tau-specific cortical pathology is detected in EC<sup>110</sup>. Cognitive impairments are apparent in the 3xTG mouse at 4 months of age, prior to onset of A $\beta$  plaque and NFT pathology, and manifest in long-term retention deficits and progresses to learning deficits at 6 months of age<sup>148</sup>. At 6 months, the mice also displayed a decrease in LTP and impairments in basal synaptic transmission in comparison to wild type<sup>146</sup>. Both male and female mice seem equally affected by the disease phenotype<sup>146</sup>. In summary, the 3xTG mouse model for AD demonstrates an age-related and progressive disease phenotype that includes both neuropathological hallmarks for AD, namely A $\beta$  plaques and NFTs. However, these lesions appear to be restricted to only parts of the cerebral cortex, hippocampus, and amygdala, likely owing to limits in the expression of the transgene.

### 1.6.3 *McGill-R-Thy1-APP rat*

The McGill-R-Thy1-APP is a transgenic rat model for AD developed by Prof. A. Claudio Cuello and his research team at McGill University in Montreal, Canada. This model was first published in 2010<sup>149</sup>. The McGill-R-Thy1-APP was developed to express the modified variant of the human APP<sub>751</sub> isoform, containing both the Swedish double mutation (K670N/M671L) and the Indiana mutation (V717F), under the control of the murine *Thy 1.2* promoter. Since the McGill-R-Thy1-APP model is reproducing AD-pathology with only a single transgene, the rat model's minimal genetic invasiveness is considered to offer the closest available analogy to the human sporadic AD pathology<sup>150</sup>.

In this transgenic AD model, homozygous rats display the complete amyloid pathology phenotype with intracellular A $\beta$  accumulation and dense fibrillar plaque deposition. The amyloid pathology in heterozygous rats, however, display only intracellular accumulation of A $\beta$  throughout their lifespan<sup>149</sup>. Intracellular accumulation of A $\beta$  in pyramidal neurons of both the cerebral cortex, and hippocampus was detectable as early as one week after birth, and was well established at 2-3 month old rats<sup>149</sup>. Amyloid plaque pathology occurs after the intracellular pathology is well established. The amount of plaque increases over time and the anatomical spreading coincides with that observed in human AD<sup>150</sup>. At 6 months of age in homozygous rats, extracellular A $\beta$  plaques accumulate first in the subiculum and occasionally in EC. At 13 months of age, plaque pathology has spread to the remaining hippocampal formation and neocortex. Finally, in 20-month old rats A $\beta$  plaques were present in nearly all areas of the brain, especially in the hippocampus, as well as in the parietal cortex and EC<sup>149</sup>. Homozygous rats displayed a clear cognitive deficiency by the age of 3 months, compared to age-matched wild type controls and heterozygous littermates when evaluated in performance in the Morris water maze test<sup>150</sup>. All described pathology was equally present in both male and female rats, and there was no evidence of any gender associated differences in A $\beta$  pathology in the McGill-R-Thy1-APP rat model<sup>149</sup>.

## 1.7 **Aims and hypotheses**

When a person develops apparent clinical symptoms of AD, the person may have already undergone at least a decade-long pre-clinical phase of the disease with underlying neuropathological changes. Understanding the early molecular mechanisms of AD is essential in order to develop effective early diagnostic tools and treatment strategies. A better understanding of the molecular mechanisms behind the initiation of NFT formation in EC LII

is therefore highly relevant. One such mechanism that lead to p-Tau formation could be the activation of tau kinases such as GSK3 $\beta$  as a result of pathological interactions between RE and intracellular A $\beta$ .

The aim of this thesis is to test the hypothesis that when RE expression is effectively reduced in EC LII, higher levels of upregulated GSK3 $\beta$  phosphorylated at Tyr216, as well as a concurrent increase in p-Tau will follow in these neurons. Investigation into the possible relationship between RE and p-Tau is done by artificial lowering of RE levels in EC LII of the APP/PS1, 3xTG and McGill-R-Thy1-APP transgenic animal models for AD

## 2. Methods

### 2.1 Animals

#### 2.1.1 Housing and animal care

All animals used in this thesis were provided by the animal facility belonging to Kavli Institute for Systems Neuroscience. All experimental procedures were performed within the Kavli Institute for Systems Neuroscience at the Norwegian University of Science and Technology (NTNU). All research animals were housed in enriched cages with free access to food and water, and kept on a 12-hour light/dark cycle in 20-23 °C, 50-60% humidity. Considerations regarding the three R's; Replacement, Reduction and Refinement, as first described by Russel and Burch <sup>151</sup>, was implemented in the planning and the performing of experiments using animals. All steps necessary to ensure good animal welfare has been taken throughout this project. The use of research animals in this thesis was approved by the Norwegian Animal Research Authority and is in accordance with the Norwegian Animal Welfare Act §§ 1-28, the Norwegian Regulations of Animal Research §§ 1-26.

#### 2.1.2 Animals used

Three different transgenic animal models were used in this thesis: the APP/PS1 AD mouse model <sup>106</sup>, the 3xTG AD mouse model <sup>147</sup> and the McGill-R-Thy-1-APP rat model for AD<sup>149</sup>. Two APP/PS1 mice, one 3xTG mouse and four McGill-R-Thy-1-APP rats were used to investigate the effects on tau phosphorylation on Ser396. Two APP/PS1 mice and one 3xTG mouse were used to investigate the effects on phosphorylation on GSK3 $\beta$  Tyr216. See Appendix 6.1 for a complete list and details of all animals used in this thesis.

### 2.2 Stereotaxic injections

#### 2.2.1 Viral constructs

The viral constructs used in this thesis were generated by Dr. Rajeevkumar Nair Raveendran at the Viral Vector Core Facility at Kavli Institute for Systems Neuroscience, NTNU. In order to reduce RE expression locally in EC LII neurons, a transgenically-targeted viral vector was injected in each animal in one cerebral hemisphere, and a control virus injected in the contra-lateral hemisphere. The experimental viral vector used was an adeno-associated virus (AAV2) with a green fluorescent protein-tag (GFP) carrying a payload of micro-RNA (miRNA) specifically designed to block translation of RE messenger-RNA (mRNA), under control of a cytomegalovirus (CMV) promoter. The control virus used was an

AAV2 containing GFP driven by a CMV promoter. The choice of experimental and control hemispheres was randomized between animals.

Initially, a complementary approach was planned where we sought to increase RE expression locally in EC LII neurons. This was attempted by utilizing a tetracycline-controlled transactivator- (Tet) dependent AAV2 containing the signaling component middle-fragment of RE (R3-R6-Tet). However, expression of the RE middle fragment failed, most likely due to the R3-R6-tet RE middle fragment being too large for our viral vector. The animals injected with the RE middle fragment as the experimental virus were excluded from further analysis.

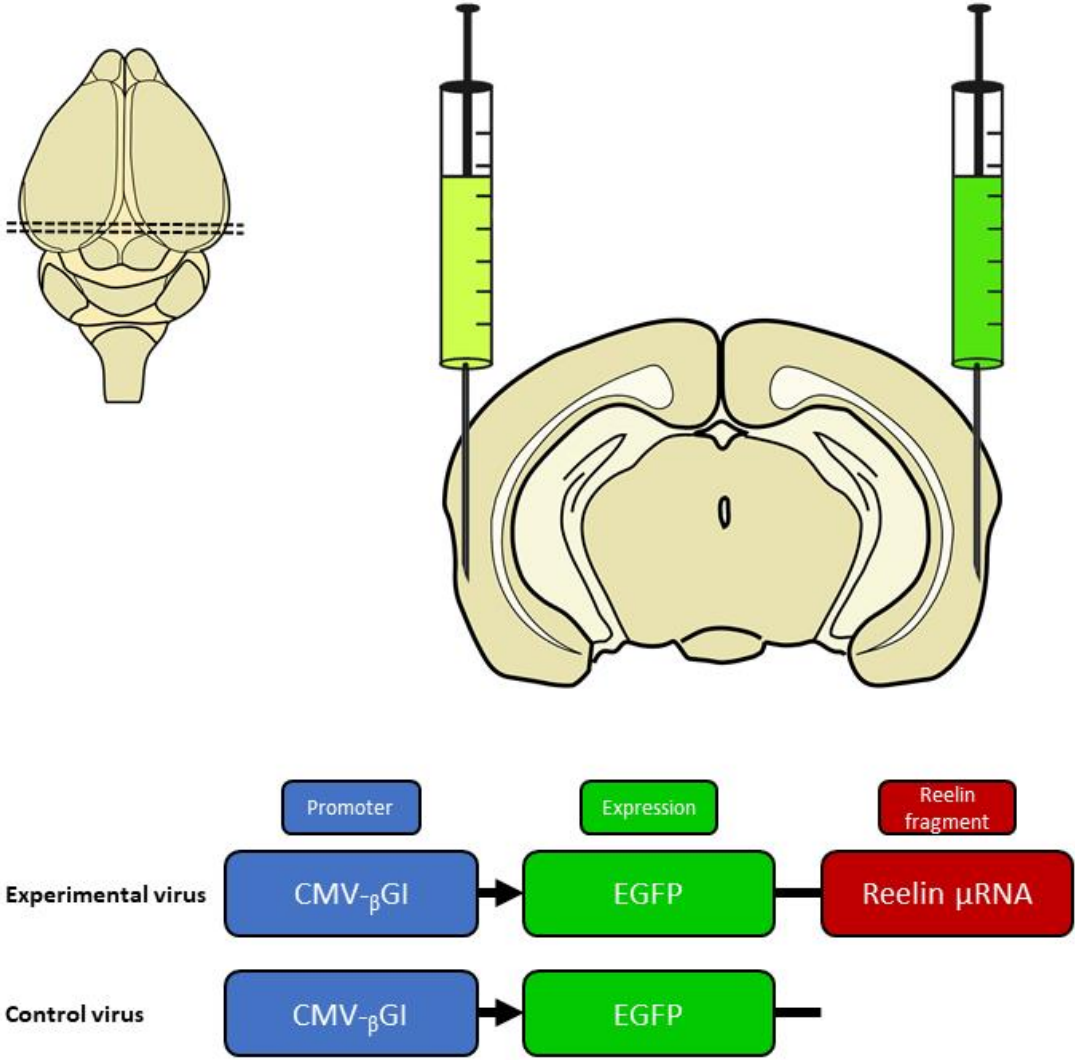


**Figure 12** Diagram of both the experimental virus and the control virus. The experimental virus was injected into EC LII and the control virus was injected into LII of the contralateral EC. The experimental virus is an AAV2 with a GFP tag carrying a payload of μRNA targeted against Reelin, driven by a CMV promoter. The control virus is identical, but does not contain μRNA targeted against Reelin.

### 2.2.2 *Stereotaxic surgery procedure*

All surgeries were performed by my thesis supervisor, Dr. Asgeir Kobro-Flatmoen. I did, however, assist him on a few surgeries involving both mice and rats. By doing this, I gained a basic theoretical understanding of the surgical procedure, and I received some practical training in performing key parts of the process. I will give a brief summary of the surgical procedure below.

The surgical environment was prepped and readied prior to the start of the surgery. This included prepping analgesics/anesthesia, lining up and sterilizing all necessary surgical equipment and preparing the microinjection-pump. Once ready, the animal was first anesthetized with 5% isoflurane gas (IsoFlo vet., Abbott Laboratories, Chicago IL, USA) in an induction chamber. Once anesthetized, the animal was weighed and subsequently mounted on the stereotaxic surgery table (Kopf Instruments, Tujunga CA, USA) with a steady flow of 1% isoflurane gas with a set airflow at 1L/min. The animal's response to pain was tested by administering pinches to the toes with forceps and checking for reflexes. The animal was deemed sufficiently anesthetized when it did not respond to nociceptive stimuli and exhibited a slow, but steady respiration. The animal's eyes were covered with Simplex, a protective balm (Tubilux Pharma S.p.A., Pomezia, Italy), to prevent drying. The eyes were covered to prevent damage to the retina by the bright fiberoptic lighting. The fur on the head of the animal was thoroughly shaved and iodine (Iodine NAF Liniment 2%, Norges Apotekforening, Oslo, Norway) was used to clean the skin. Marcain (0.06ml/30g, bupivacaine, AstraZeneca AB, Södertälje, Sweden) was subcutaneously injected beneath the scalp of the animal. Additionally, Metacam (0.12ml/30g, meloxicam, Boehringer Ingelheim Vetmedica GmbH, Ingelheim am Rhein, Germany) and Temgesic (0.09ml/30g, buprenorphine, Indivior, Dublin, Ireland) was subsequently administered separated by one minute. The animal was then left for a few minutes in order for the analgesics to take full effect. The head of the animal was fixed in place on the stereotaxic frame (Kopf Instruments, Tujunga CA, USA) with ear bars and the rostral-caudal and medial-lateral alignment was controlled by aligning the points of bregma and lambda on the animal's skull (Figure 13). A single straight midline incision was made from the frontal cranial bones to the back of the interparietal cranial bones using a small blade scalpel. The skin was pulled apart and held in place with hooks. The periosteum was removed and the top of the skull was rinsed with a saline solution and cleaned with cotton swabs. By using

predetermined coordinates<sup>1</sup> specific to mice and rats, the first injection point was identified by navigating from sinus sagittalis and sinus transversus. Once the first injection point was identified, a craniotomy was performed by carefully drilling a small hole with a handheld drill. A glass capillary containing the viral vector was gently lowered into the brain. The capillary was kept in place for 5 minutes, allowing the surrounding tissue to retract around the needle. The subsequent injection was done using a microinjector pump (Micro4, World Precision Instruments, Hertfordshire, United Kingdom), injecting at a constant speed of 30 nl/min. After the injection was completed, the capillary was kept in place for an additional 5 minutes to prevent backflow of the viral vector. The capillary was slowly retracted from the brain. The skin was sutured, and the animal was placed in a heated recovery cage to recuperate. The well-being of the animal was constantly monitored throughout the procedure.

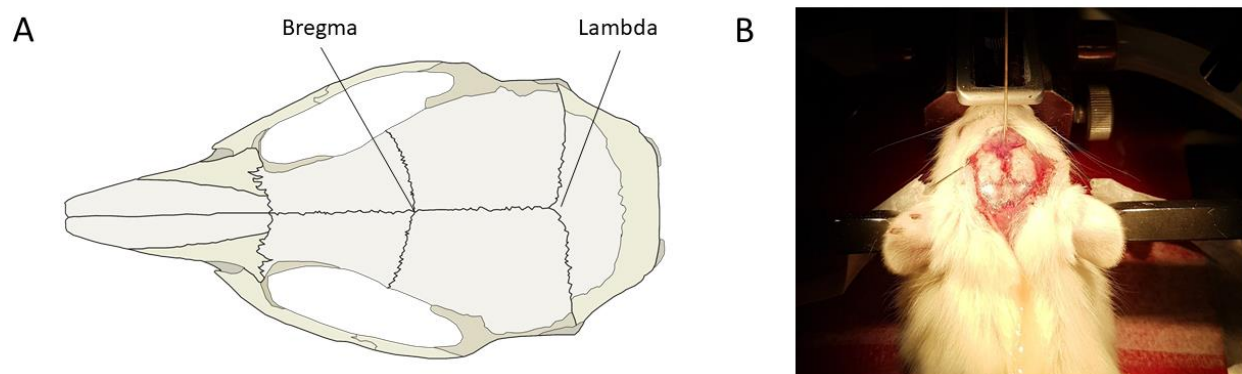


**Figure 13** (A) Diagram of a rat skull viewed from above, highlighting the reference points bregma and lambda used in stereotaxic surgeries for the purpose of leveling the brain. Bregma is located at the intersection between the frontal bone and the parietal bones, and lambda is positioned where the parietal bones meet the occipital bone. Note that lambda is not located precisely at the intersection where the skull bones meet, but it is placed on the midpoint of the curve of best fit along the lambdoid suture. (B) Rat mounted on the stereotaxic surgery table and fixed in place with ear bars. A midline incision has been made, exposing the skull, and making the points bregma and lambda visible.

## 2.3 Tissue processing

### 2.3.1 Transcardial perfusion and brain extraction

After carrying the viral vectors for the predetermined time, animals were anesthetized with 5% isoflurane gas in an induction chamber, weighed, and given an intraperitoneal injection of pentobarbital (100mg/kg, NAF vet, Oslo, Norway) appropriate to its weight. The animal was placed back into the induction chamber, and dose of isoflurane lowered to 2%. Once respiration reached the point of clearly being in the terminal phase, the animal was

<sup>1</sup> Stereotaxic coordinates for mice: sinus sagittalis +3, sinus transversus +2, move laterally towards the edge of the skull, injection at -2.8 depth.

Stereotaxic coordinates for rats: sinus sagittalis +3.30, sinus transversus +4.60, move laterally towards the edge of the skull (roughly +3.60), injection at -4.50 depth.

transferred from the induction chamber to a down-ventilated surgery table. Absence of reflexes was determined by pinching the animal's paws with forceps. The procedure would then only continue if the animal proved unresponsive. The animal was taped in place in a supine position, and a lateral incision was made through the integument and abdominal wall beneath the rib cage. Subsequently two incisions were made on both sides along the entire length of the rib cage, exposing the pleural cavity. The diaphragm was cut along the rib cage, and the rib cage was cut through up to the collar bone on both sides. The sternum was clamped with a hemostat, and placed over the head, fully exposing the heart. A cut in the heart's right atrium was made, and a perfusion needle connected to a Peri-Star pro 4-channel perfusion pump (World Precision Instruments Inc., Hertfordshire, United Kingdom) was carefully inserted into the left ventricle in a straight angle to prevent accidental penetration into the right ventricle. Ringer's solution (3.35 mM KCl, (Merck KGaA, Darmstadt, Germany), 145 mM NaCl (VWR International, Radnor, PA, USA), 2.28 mM NaHCO<sub>3</sub> (Merck KGaA, Darmstadt, Germany), pH 6.9, room temperature) was administered through the perfusion needle at a constant pressure, emptying the blood content of the animal through the right atrium. Ringer's solution was administered until the solution exiting the heart was clear of blood and the liver was lighter in color. At this point, the ringer's solution was disconnected at the pump, and 4% freshly depolymerized paraformaldehyde (PFA, Merck kGaa, Darmstadt, Germany) in 125mM phosphate buffer (PB, pH 7.4) was connected and administered through the same needle in order to fixate the brain. Fixation tremors and movement of the tail was taken as indicators of a good fixation. PFA was administered for roughly 5 minutes, until the fixation tremors completely subsided.

In order to extract the brain, the animal's head was first completely removed from the body. Then, a midline incision from the top of the neck to the nose was made, exposing the dorsal cranium. Remaining neck and chin musculature were then removed, and skin peeled back, exposing the entirety of the cranium. A pair of small sharp scissors were placed inside the foramen magnum, and the skull was carefully cut along the dorsal midline, traveling the inner surface of the skull caudo-rostrally with the tip of the scissors facing upwards to avoid damaging brain tissue. Using a rongeur, the dorsal surface of the skull was carefully peeled of, followed by removal of the sides of the skull. The cranial nerves and small parts of the olfactory bulb was severed using a spatula, and the brain was subsequently removed from the lower part of the skull and placed in brain cup containing PFA. The brain was kept in PFA overnight at 4 °C. The following day, the brain was transferred to a cryoprotective PB

solution containing 2% dimethyl sulfoxide (DMSO, VWR International, Radnor, PA, USA) and 20% glycerol (VWR International, Radnor, PA, USA), and stored for a minimum of 24 hours until sectioning.

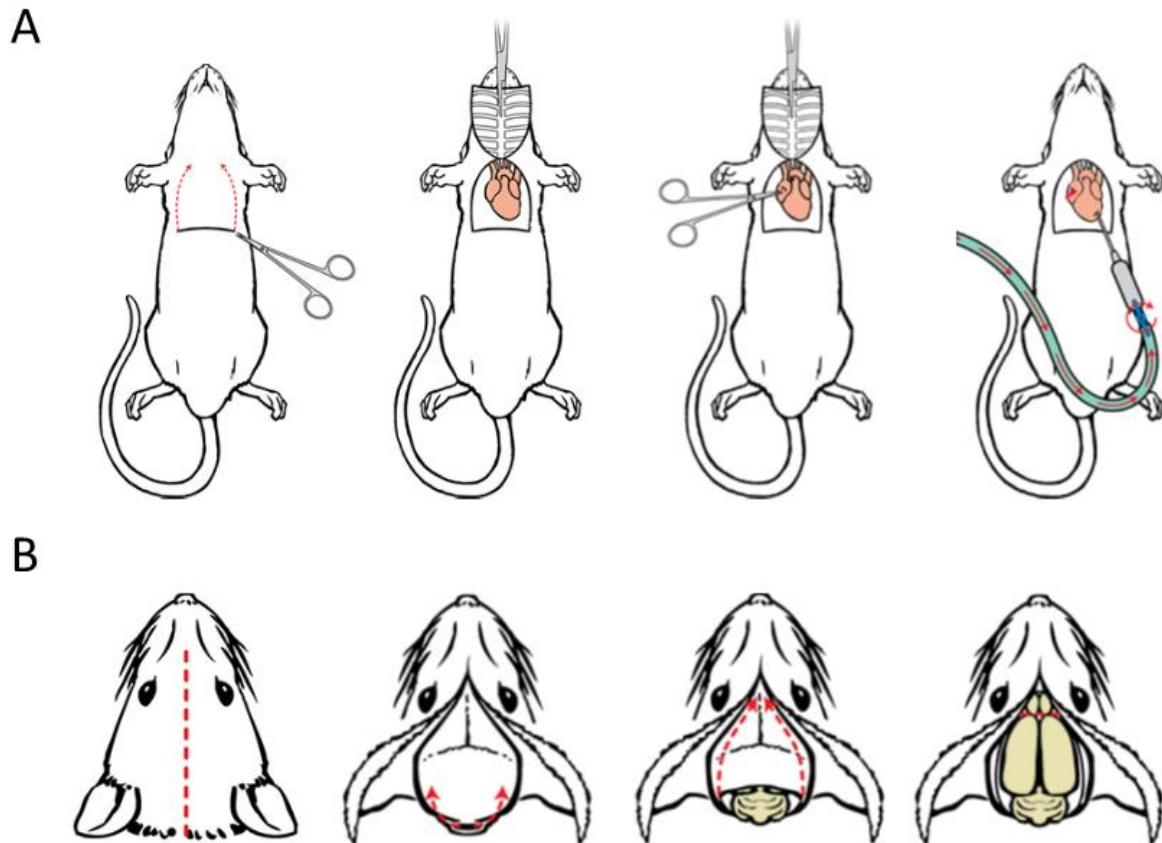


**Figure 14** (A) Transcardial perfusion of rat visualized in a stepwise manner. Steps one and two illustrates how to correctly open the chest cavity, exposing the heart. Steps three and four shows how to cut the right atrium and how to correctly insert the perfusion needle into the left ventricle. (B) Step wise illustration of how to expose a brain for extraction. All illustrations have been adapted from Gage, Kipke & Shain <sup>152</sup>.

### 2.3.2 Brain sectioning

All brains were sectioned in the coronal plane. Before sectioning, each brain was marked by a small incision running along the entire right dorsal cerebral hemisphere to enable differentiation of the hemispheres. All brains were sectioned using freezing sledge microtome (Microm HM430, Thermo Fisher Scientific, Waltham, MA, USA) set at a temperature to  $-37^{\circ}\text{C}$ . A base of sucrose (VWR International, Radnor, PA, USA) solution (30% sucrose dissolved in 0.4M PB and  $\text{H}_2\text{O}$ ) was applied to the microtome base and leveled with the microtome blade. In order to properly mount brains to the microtome in an upright position, the caudal-most portion of the cerebellum was cut at a straight angle, creating a flat base on which brains could stand. After placing brains on the sucrose base, they were visually inspected and adjusted such that the midline was perpendicular to the surface, before applying

additional sucrose to the surface of the brain, attaching it firmly to the microtome stage. The brain was then covered with finely crushed dry ice and left to freeze all the way through. Once frozen solid, sectioning could be performed. Additional dry ice was applied throughout the process to ensure the brain tissue was kept frozen. All experimental APP/PS1 and 3xTG mouse brains were cut into series of five at 30  $\mu\text{m}$ . The McGill-R-Thy1-APP rat brains were sectioned into six series at 40  $\mu\text{m}$ . Due to this thesis being part of a larger ongoing research project, the virus-injected rat tissue were needed for a wide range of analyses and tissue was in short supply. Therefore, one series from each injected rat was sorted rostral-caudally and split in half. One half was used for analysis of p-tau, and the other half was given back to my supervisor. No rat tissue was available for GSK3 $\beta$  analysis at the time. All sectioned series of brains consisted of equally spaced coronal slices and was stored at  $-24\text{ }^{\circ}\text{C}$  in DMSO in individual tubes.

## **2.4 Immunohistochemistry**

### *2.4.1 Double fluorescent immunohistochemistry protocol in viral-injected tissue*

In order to investigate potential changes in p-Tau as a function of lowered expression of RE, tissue injected with the viral construct were subjected to double fluorescent immunohistochemical labeling with primary antibody (PA) anti-pSer396 (Abcam, Cambridge UK) and anti-RE G10 (Merck kGaA, Darmstadt, Germany). In the APP/PS1 and 3xTG mouse models, anti-pGSK3 $\beta$  Tyr216 (Abcam, Cambridge UK) was also used to investigate potential upregulations of the GSK3 $\beta$  tau-kinase as a result of lowered RE levels and was used in double fluorescent immunohistochemical labeling in combination with anti-RE G10. For a complete list of all PA used, see Table 1.

**Table 1**

Overview of primary antibodies used in this thesis.

<i>Product name</i>	<i>Host/Clonality</i>	<i>Target</i>	<i>Manufacturer</i>	<i>Catalog number/RRID</i>	<i>Batch number</i>
<b><i>Anti-Tau (phospho S396) antibody EPR2731</i></b>	Rabbit monoclonal	Tau phosphorylated at serine 396	Abcam	ab109390, RRID: AB_10860822	303639
<b><i>Anti-GSK3 beta (phospho Y216) antibody</i></b>	Rabbit polyclonal	Endogenous levels of GSK3 $\beta$ phosphorylated at tyrosine 216	Abcam	ab75745, RRID: AB_1310290	258756
<b><i>Phospho-Tau (Ser202, Thr205) Antibody AT8</i></b>	Mouse monoclonal	Tau phosphorylated serine 202 and threonine 205	Thermo Fisher Scientific	MN1020, RRID: AB_223647	2207392
<b><i>Anti-Reelin Antibody G10</i></b>	Mouse monoclonal	Mouse reelin amino acids 164-496.	Merck Millipore	MAB5364, RRID: AB_11212203	3099957

Excess DMSO were rinsed off in short washes of PB 3 times for 2 minutes. After this, the tissue underwent heat induced antigen retrieval (HIAR) in 40 ml PB for 2 hours at a temperature of 60°C. After HIAR, sections were washed 3 times for 10 minutes in PB containing 0.2% Triton X-100 (PBT, Merck kGaA, Darmstadt, Germany). To prevent non-specific binding of the antibodies, the tissue was incubated in PBT with 10% normal goat serum (NGS, Abcam, Cambridge, UK) for one hour. After this, the tissue was incubated overnight at 4°C with PA goat anti-rabbit pSer396 (1:2000) or goat anti-rabbit pGSK3 $\beta$  Tyr216 (1:1000) with goat anti-mouse RE G10 (1:1000) in PBT containing 5% NGS. The following day, the tissue was rinsed in PBT 3 times for 10 minutes. In order to visualize the PA, the tissue was incubated for 2 hours in room-temperature, protected from light with fluorescent secondary antibodies (SA), goat anti-rabbit Alexa Flour 546 (1:1000, Invitrogen, Carlsbad, CA, USA) and goat anti-mouse Alexa Flour 635 (1:1000, Invitrogen Carlsbad, CA, USA) in PBT containing 5% NGS. For a complete list of SA used in this thesis, see Appendix 6.3. After this, the tissue was rinsed 3 times for 10 minutes in PB, followed by a quick wash in tris(hydroxymethyl)aminomethane (Tris, Merck kGaA, Darmstadt, Germany) pH-adjusted to 7.6 with hydrochloric acid (HCl) 2 times for 5 minutes.

#### 2.4.2 *3,3'-diaminobenzidine*

To ensure that the fluorescent signal was not confounded by autofluorescence, and to optimize immunohistochemical protocols, the PAs for AT8 and anti-pSer396 and anti-GSK3 $\beta$  Tyr216, were subjected to immunohistochemical testing using 3,3'-diaminobenzidine (DAB, Sigma-Aldrich, St. Louis, MO, USA) as chromogen. This testing was done in tissue from un-injected AD animal models used in this thesis, as well as wild type controls. Prior to incubation with the respective PA, endogenous peroxidases were quenched by incubating the sections in 3% hydrogen peroxide (H<sub>2</sub>O<sub>2</sub>, Sigma-Aldrich, St. Louis, MO, USA) solution in PB or Tris-buffered saline (TBS). After incubation with SA, all sections were incubated in PBT/TBS with 0.2% triton-x (TBS-Tx) containing Avidin-Biotin complex (ABC, Vector Laboratories, Burlingame, CA, USA). DAB was prepared two hours prior to use: One 10mg DAB tablet was dissolved in 15ml Tris-HCl heated to 50 °C and kept on a magnetic stirrer. Before incubating, 12  $\mu$ l hydrogen peroxide was added, and the DAB solution was filtered. Depending on the observed chromogenic signal, the tissue was incubated for 2 minutes (for pSer396/pGSK3 $\beta$ ) up to 10 minutes (for AT8).

#### 2.4.3 *Cresyl Violet-staining (Nissl-staining)*

To accurately delineate anatomical borders, I carried out Nissl-staining of non-experimental animals. Nissl staining involves cresyl violet dye binding to negatively charged nucleic acids like RNA and DNA within the neuron, rendering a dark blue color. Tissue mounted on microscope slides was dehydrated by gently dipping the microscope slides 10 times in ethanol in increasing concentrations (50-, 70-, 80-, 90-, 100-, 100-, and 100% ethanol). After this, the tissue was placed 2 minutes in xylene (VWR International, Radnor, PA, USA) for clearing/de-fatting. The tissue was rehydrated by dipping 10 times in ethanol in the reverse order, and briefly washed in water before the tissue was placed in the Cresyl Violet solution (0.1%, Sigma-Aldrich, St. Louis, MO, USA) on a shaker, protected from light. The tissue was left in the Cresyl Violet solution for approximately 3-4 minutes. Once sufficient color-contrast was obtained, sections were put in running water to rinse off excess color and then put in 70% ethanol containing acetic acid for a few seconds. This was repeated until the optimal contrast was achieved. After this, the sections were once again dehydrated in increasing concentrations of alcohol and placed in xylene for clearing before being coverslipped with entellan (VWR International, Radnor, PA, USA) containing xylene.

#### 2.4.4 *Tissue mounting and coverslipping*

After processing, all immuno-labeled tissue was mounted in Tris-HCl buffer in on Superfrost (Thermo Fisher Scientific, Waltham, MA, USA) microscope slides. The mounted tissue was left on a heating plate set to 37°C, protected from light. The following day the microscope slides were rinsed in either Toluene (VWR International, Radnor, PA, USA) or Xylene for 3-4 minutes in order to remove excess water and lipids. Subsequently the microscope slides were coverslipped with Entellan containing either Toluene or Xylene accordingly. The coverslipped microscope slides were left to dry overnight, protected from light.

## 2.5 **Microscopy**

### 2.5.1 *Fluorescent and bright field microscopy*

Fluorescently stained tissue was inspected with an epifluorescent microscope (Axio.Imager M1 light microscope, Carl Zeiss AG, Oberkochen, Germany) to verify the presence of cells infected with the viral constructs in both experimental and control hemispheres.

### 2.5.2 *Tissue scanning*

All Nissl-stained and DAB-stained tissue was digitized with a bright field scanner (Zeiss Axio Scan.Z1, Carl Zeiss AG, Oberkochen, Germany) at 20x magnification. Tissue stained with fluorescent antibodies were digitized using a fluorescent scanner (Zeiss Axio Scan.Z1) at 20x magnification with channels specific to wavelengths 488nm, 546nm and 635nm.

## 2.6 **Data analysis**

### 2.6.1 *Inclusion criteria for quantitative data analysis*

Several criteria had to be met for the processed brain tissue to be included in the final data analysis. As previously mentioned, all animals injected with the RE middle fragment were excluded from further analysis due to lack of viral vector expression (see section 2.2 and appendix 6.1). Variabilities in the stereotaxic injection could exclude brains from analysis after processing and immunohistochemistry: first, the experimental virus and the control virus had to be sufficiently expressed with GFP-infected EC LII cells in both cerebral hemispheres. Analysis could not be performed in brains with GFP-infected cells in only one hemisphere or in brains where no GFP-infected cells were visible. Secondly, miRNA-infected cells and

control-virus infected cells on the contralateral side could only be analyzed and compared if they were part of cell populations at the same level.

### 2.6.2 *Quantitative data analysis*

All fluorescent quantitative image analysis of the digital output from Axio Scanner was performed using the Zeiss Zen software (ZEN 2.6 blue edition, Carl Zeiss Microscopy GmbH, Jena, Germany). All sections containing virus-infected cells in EC LII were identified, and sorted rostro-caudally to ensure that each experimental hemisphere was compared to a control hemisphere in the corresponding bregma level. If the viral expression in LEC was greater in one hemisphere compared to the contralateral hemisphere, the tagged cells in the hemisphere with the largest viral expression were restricted to the same region of infected cells in the contra-lateral hemisphere with less viral expression. This ensured that a comparable population of cells in both hemispheres was compared. To guard against experimenter-bias when selecting cells for analysis, only the channel visualizing the GFP-signal (488) was visible. Channels visualizing p-Tau/GSK $\beta$  and RE were switched off. Densitometric image analysis was performed in order to quantify the fluorescent signal present in the scanned brain tissue. GFP-infected cells were individually selected using the circle tool set to a diameter of 20  $\mu\text{m}$  ( $\pm 0.1\mu\text{m}$ ). This made the selection of each individual cells consistent, and the diameter of 20  $\mu\text{m}$  corresponded well to the size of the great majority of GFP-infected cells.

This gave a readout of the pixel intensity of all channels individually within each circle. Only GFP-infected cells displaying a clearly defined soma in EC LII were selected for analysis. Once all relevant cells were marked in one hemisphere, the pixel intensity readouts were saved as a .czt-file for further data analysis. The same process was repeated in the contralateral hemisphere.

### 2.6.3 *Background subtraction*

To subtract fluorescent background from the data analysis, a baseline readout of p-Tau or GSK3 $\beta$  in conjunction with RE was performed for each immune-labeled series. In the rat brain, the most abundant isoform of tau, the 4R-tau, has the lowest expression in the cerebellum<sup>91, 153</sup>. In the mouse brain, endogenous tau exhibits only weak staining in the white matter of the cerebellum<sup>154</sup>. Consistent with the above-mentioned literature, own readouts of p-Tau in the cerebellum proved to be low in both mice and rats.

GSK3 $\beta$  is abundant throughout the entire brain, including in the mouse brain in regions like the hippocampus, thalamus and cerebellum<sup>120, 155</sup>. However, GSK3 $\beta$  has been reported to change from being highly expressed in cerebellar axons during development, to being virtually absent in cerebellar axons after maturation at 5 weeks<sup>155, 156</sup>. Consistent with this, own readouts of detectable GSK3 $\beta$  Tyr216 in cerebellar white matter was low compared to other regions.

Therefore, for p-Tau and GSK3 $\beta$  analysis in the rodent brain, regions of interest (ROI) were drawn in the white matter of the cerebellum and the readout showing the lowest pixel intensity for p-Tau or GSK3 $\beta$  in conjunction with RE was selected. The values for each channel was then subtracted from each individual measurement pr. cell for the series in question (see following section).

#### 2.6.4 Data processing

The relevant output tables of each. czf-file were copied into Microsoft Excel (Version 1908, Microsoft Corporation, Redmond, WA, USA). The background measurements were then subtracted from each individual measure/cell, and subsequently all measures were normalized using the min/max normalization:  $z = (x - \min(x)) / (\max(x) - \min(x))$ . The normalized data were then plotted into respective graphs/scatterplots using Excel's built in functions.

Statistical analysis was performed using IBM SPSS Statistics for Windows (version 26.0.0.0, IBM, Armonk, NY, USA). Independent samples t-test were performed to compare the means of the experimental- and control-hemispheres. A prerequisite for performing an independent samples t-test, is that the data is normally distributed. The Central Limit Theorem postulates that with a sample size larger than 30, the sampling distribution of the mean will be normally distributed<sup>157</sup>. When analyzing sample sizes larger than 30, independent samples t-test were still conducted even if the assumption of normality could be considered violated. In sample sizes smaller than 30, the non-parametric Mann-Whitney  $U$  test used. To calculate effect sizes, the following formulae has been used:  $d = 2t/\sqrt{df}$ ,  $r = z/\sqrt{n}$ .

Illustrations and photo editing for figures were performed using Adobe Photoshop CS6 (Adobe Systems Inc., San Jose, CA, USA), Adobe Illustrator 2019 (Adobe Systems Inc., San Jose, CA, USA) and Microsoft Powerpoint (Version 1908, Microsoft Corporation, Redmond, WA, USA).

## 2.7 Delineation

The entire rostro-caudal EC axis was delineated coronal Nissl sections in both un-injected C57BL/6 control mouse and un-injected McGill-R-Thy1-APP rat tissue. The boundaries of EC LII were outlined, and EC was further subdivided into LEC and MEC. Delineation for rats were based on *The Rat Brain in Stereotaxic Coordinates*<sup>158</sup> and *The Rat Hippocampus Atlas*<sup>34</sup>. Delineation for mice were based on<sup>159</sup> and *The Allen Mouse Brain Atlas*<sup>160</sup>. The delineation of Nissl-stained tissue from the C57BL/6 control mouse and McGill-R-Thy1-APP rat are featured in the figures included in the results section as visual references.

### 2.7.1 Delineating the lateral entorhinal cortex

The anterior borders of LEC meet with both olfactory and amygdaloid cortices: the piriform cortex laterally, and the periamygdaloid cortex and the posterior cortical nucleus of the amygdala medially,<sup>161</sup>. The anteriormost part of LEC appears as a thin strip bordering the dorsal piriform cortex and ventral perirhinal cortex area 35 (Figure 15A). At the rostral portion of LEC, the dorsal borders of LEC ends just ventral of the rhinal fissure. Differentiating the rostral LEC from the piriform cortex can be accomplished by comparing differences in laminar organization between the two areas. While EC has six identifiable cell layers, the piriform cortex only has three<sup>162, 163</sup>. Defining the border between dorsal LEC and ventral perirhinal cortex is done by identifying EC LII's larger cells from the smaller cells in perirhinal LII<sup>161</sup>. Another differentiating feature is the absence of a distinct cell-free LIV (lamina dissecans) in the perirhinal cortex<sup>161, 162</sup>. Moving caudally, the thin strip of LEC increase in size and gradually occupy an increasingly larger portion of the ventral part of the cerebral hemisphere (Figure 15B). As this happens, the ventral border of LEC changes from piriform cortex to the amygdalopiriform transitional area (APir)<sup>158</sup>. The APir can also be differentiated from ventral LEC by its three-layered laminar structure<sup>164</sup>. Moving further caudally, the APir recedes, and LEC meets the most medial part of MEC<sup>158</sup>. Differentiating LEC from MEC will be discussed further below (section 2.7.3). LEC will have reached its largest surface area coronally at approximately the point where the caudal end of the perirhinal cortex gives way to the postrhinal cortex. At this point, the dorsal border of LEC will have moved from its starting point of being below the rhinal sulcus, into the fundus of this sulcus. The ventral border will also at this point have moved nearly 90 degrees ventrally, bordering MEC ventromedially and the subiculum and perirhinal cortex dorsally<sup>158</sup> (Figure 15D).

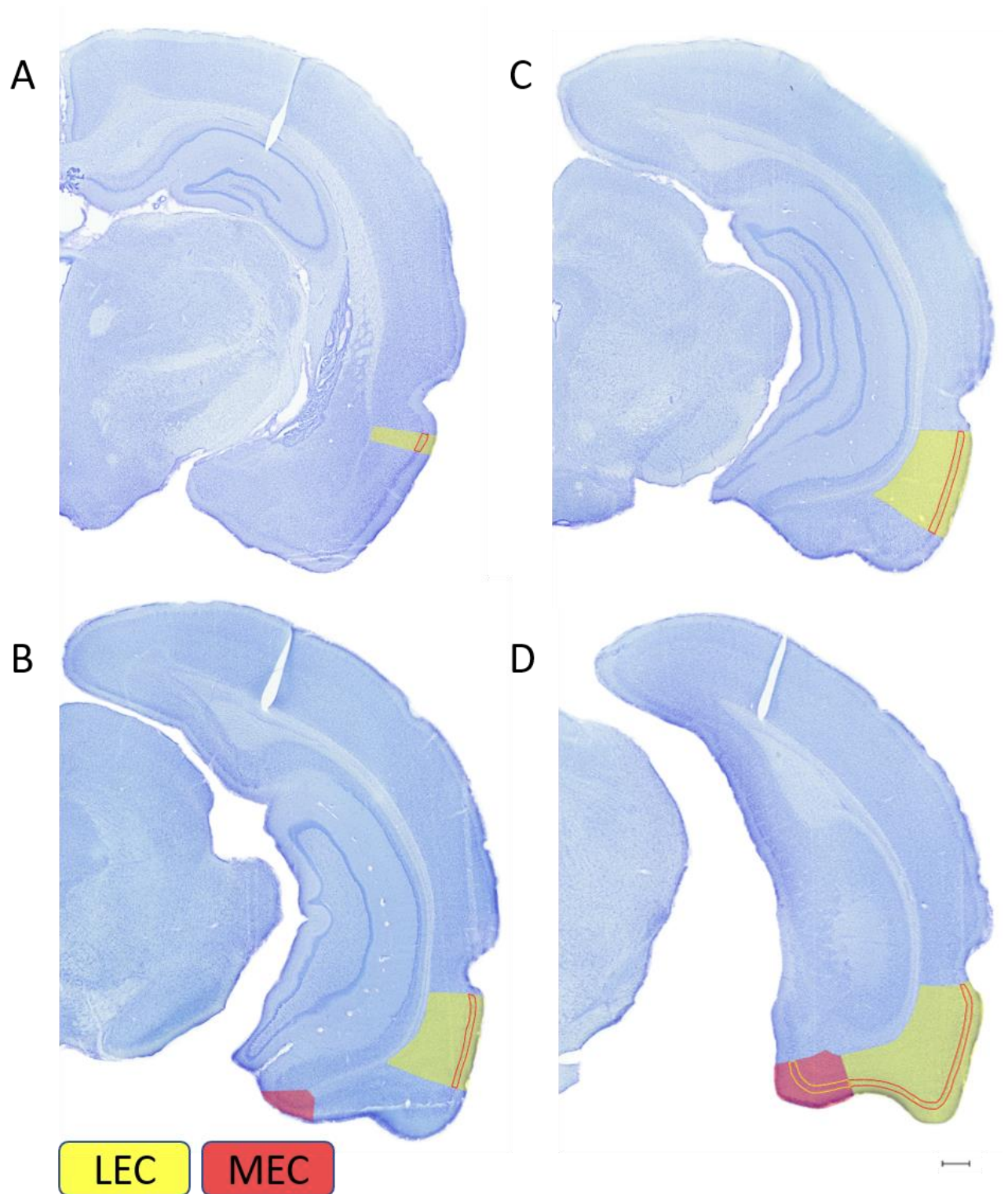


**Figure 15** Selected sections of delineation of lateral entorhinal cortex (LEC) and medial entorhinal cortex (MEC) with layer II outlined. (A) The rostralmost part of LEC appearing below the rhinal fissure (Bregma -4.24). (B) The expansion of LEC as one moves caudally (Bregma -5.68). (C) The rostral portion of MEC appearing (Bregma -5.86). (D) The ventral border of LEC meets the lateral border of MEC. The dorsal border of LEC starts moving up into the fundus of the rhinal fissure (Bregma -6.94). 5-month-old male McGill-R-Thy1-APP +/+ rat. Scale bar = 500  $\mu$ m.

### 2.7.2 *Delineating the medial entorhinal cortex*

At the rostralmost portion of MEC, the dorsal border is with the ventral subiculum (Figure 15C) <sup>158</sup>. Moving further caudally, the dorsal border will eventually be replaced by the parasubiculum, which will remain MEC's dorsal border throughout the rest of the rostrocaudal axis <sup>158</sup>. MEC can be differentiated from the ventral subiculum and parasubiculum by having six distinct cell layers, with a clear lamina dissecans <sup>162</sup>. Also, MEC LII thickens into a club-like shape at its dorsal border to the parasubiculum, further aiding differentiation between the two regions. At this level the lateral border of MEC is set against APir <sup>158</sup>. APir can be identified by having less developed lamination, a broad LI and a scalloped border between LI and LII, and no marked lamina dissecans <sup>35</sup>. Moving further caudally, the lateral border of MEC is replaced by the ventral extension of LEC (Figure 15D) <sup>158</sup>. Moving further caudally, the LEC will disappear, and the MEC will make up the entirety of the ventral hemisphere <sup>34</sup>. MEC will at this point have its dorsolateral border with the postrhinal cortex. The postrhinal cortex can be distinguished from MEC by its laminar structure, namely that the postrhinal cortex have a bilaminar appearance due to LII/LIII and LV/LVI appearing merged <sup>162</sup>.

### 2.7.3 *Differentiating the lateral entorhinal cortex from the medial entorhinal cortex*

LEC can be differentiated from MEC by comparing the laminar structure between the two. LII of LEC has a narrower appearance than LII of MEC, and stellate cells in MEC tends to be clustered together <sup>34, 35, 162</sup>. Also, the lamina dissecans of MEC is more sharply delineated than in LEC, and the deeper layers of MEC, mainly layer V, displays a distinct radial, column-like arrangement <sup>162</sup>.

### 2.7.4 *Delineating entorhinal cortex layer II*

EC LI is the most superficial layer and is sparsely populated by neurons, making it easily distinguishable from LII. There are currently multiple ways of delineating EC LII/LIII being used. This thesis will base its delineation of EC LII/LIII on the original definition by Cajal and Lorende de N6 <sup>42, 43</sup>. Using their definition, it is posited that LII is rather narrow and mainly contains neurons with a stellate morphology. Also, LII contains pyramidal-like neurons with apical dendrites oriented towards the pia and occasional classical pyramidal neurons, both being spread among the stellate neurons<sup>40</sup>. LIII is described as a broad and dominated by several strata of pyramidal neurons, with somewhat larger pyramidal neurons present at the border with LIV, whereas the neurons located towards the border to LII are relatively small to medium sized pyramidal neurons <sup>40</sup>.



### 3. Results

#### 3.1 Large amounts of non-specific binding in APP/PS1 tissue caused by mouse on mouse cross reactivity with secondary antibody

##### 3.1.1 Non-specific binding in plaque-like substances in APP/PS1 mice

Initial testing with the AT8 PA on un-injected APP/PS1 tissue revealed high amounts of apparent reactivity. However, the same amount of reactivity was found in the control section where AT8 was omitted from the protocol. The reactivity manifested itself as high amounts of plaque-like substances distributed throughout the tissue, especially in the neocortex and in the hippocampal formation (Figure 16). The plaque-like substances varied in morphology, most being similar in appearance to diffuse A $\beta$  plaques, while some had the appearance similar to that of dense-core A $\beta$  plaques.

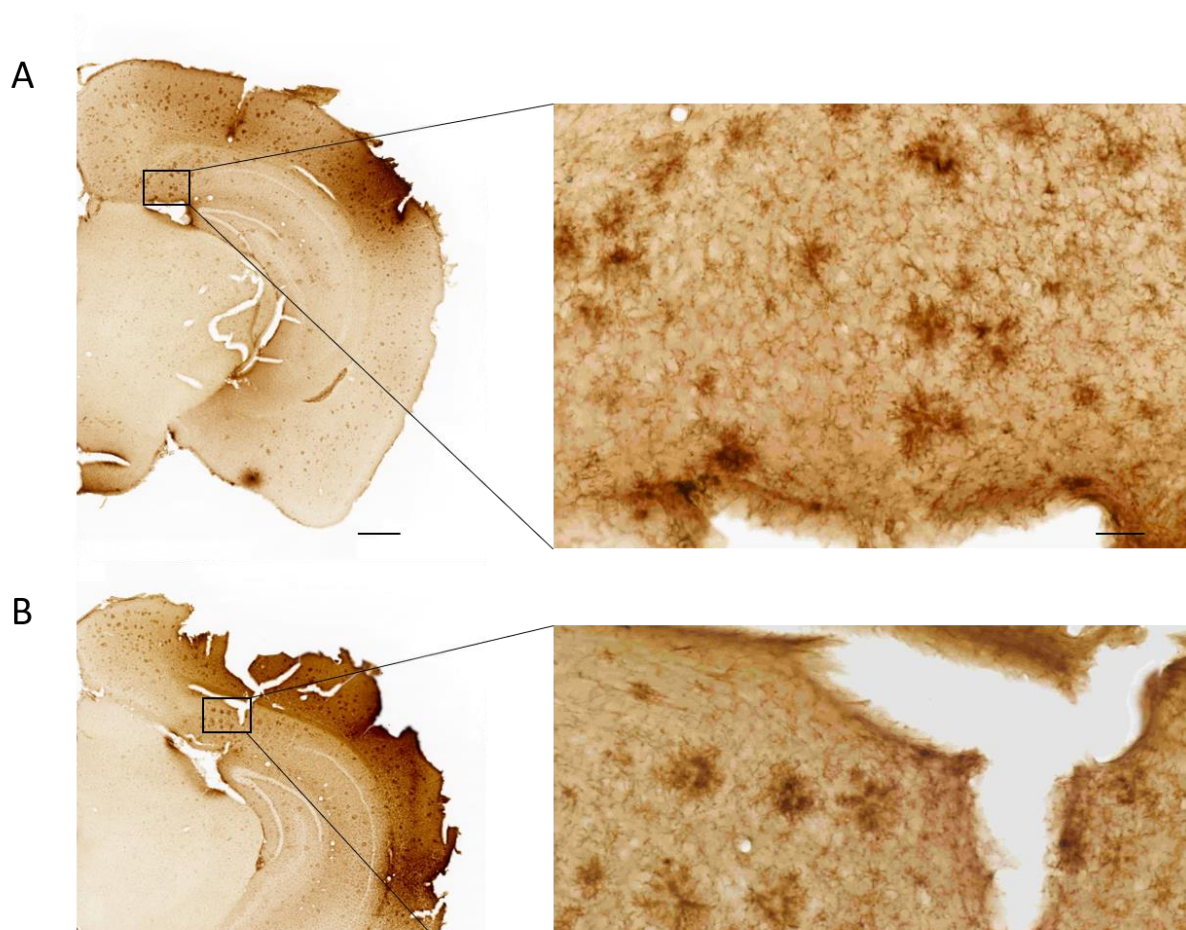


**Figure 16** AT8 immunostaining of a 5 months old male APP/PS1 +/- x CK2/tTa +/- (71758). Primary antibody (PA) AT8 (1:1000), biotinylated Goat anti-Mouse secondary antibody (SA) (1:500), visualized with 3,3'diaminobenzidine (DAB). (A) Immunostaining with both PA and SA, (B) immunostaining but with omission of PA. Zoom-in of the subiculum reveals plaque-like staining in both conditions. Scale bars = 500µm, 50µm for zoomed inset.

This prompted me to undertake rigorous testing of the AT8 antibody, with multiple variations to the protocols to ensure that the non-specific binding was not due to user error. In each immunohistochemical procedure devoted to this purpose, two sections from each animal was used: One section was run only with SA, and one section with neither SA nor PA.

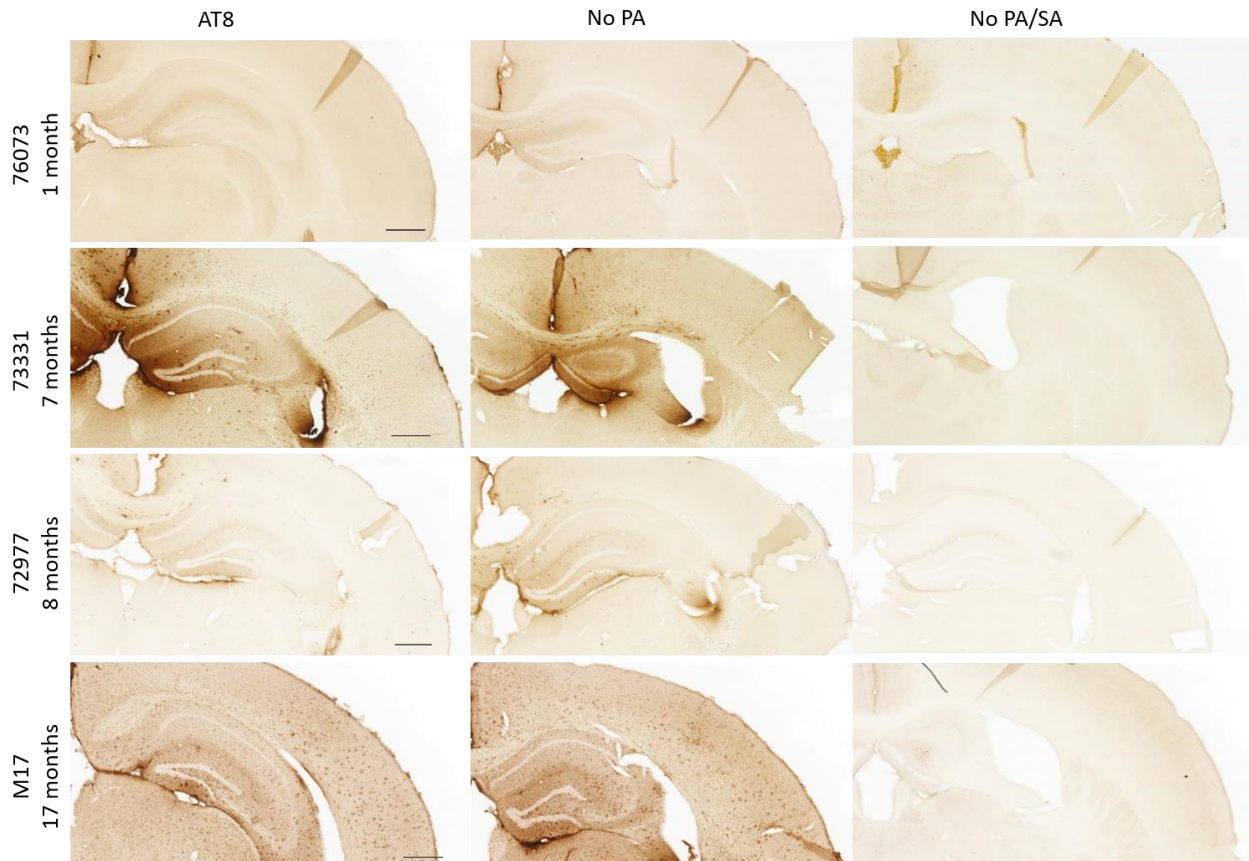


**Figure 17** AT8 immunostaining in APP/PS1 mice in different ages. 1-month old male APP/PS1<sup>+/-</sup> x Ck2/tTA<sup>+/-</sup> (76073) primary antibody (PA) AT8 (1:1000), biotinylated Goat anti-Mouse secondary antibody (SA) 1:500. 7-month old male APP/PS1<sup>+/-</sup> x Odz3-P8117<sup>+/-</sup>;tetO-HM4<sup>+/-</sup> (73331), AT8 (1:1000), SA (1:1000). 8 month old male APP/PS1<sup>+/-</sup> x Odz3-P8117<sup>+/-</sup>;tetO-HM4<sup>+/-</sup> (72977), AT8 (1:1000), SA (1:500). 17-month-old male APP/PS1 (M17), AT8 (1:1000), SA (1:1000). Scale bars = 500µm.

Further testing of the AT8 antibody in APP/PS1 mice across different ages, revealed similar results, where the tissue incubated only with SA had equivalent staining to the tissue processed with both PA and SA. No reactivity was seen in tissue incubated with neither PA or SA, demonstrating that the reactivity in the tissue stems from the SA, and not the DAB chromogen (Figure 17). Only slight reactivity could be detected in young mice, with no visible plaque-like substances. High amounts of reactivity with the SA-only was detectable by 5 months (Figure 16) but did not necessarily increase in an age dependent manner. Comparisons between 7-month old (73331) and 8-month old (72977) APP/PS1 mice shows quite large variability in the amount of SA reactivity, where the 8-month old mouse displayed

markedly less reactivity than 7-month old. The oldest APP/PS1 mouse at 17-months of age (M17) showed an almost uniform deposition of plaque-like substances throughout the neocortex, thalamus, and hippocampal formation.

### 3.1.2 Testing in other animal models

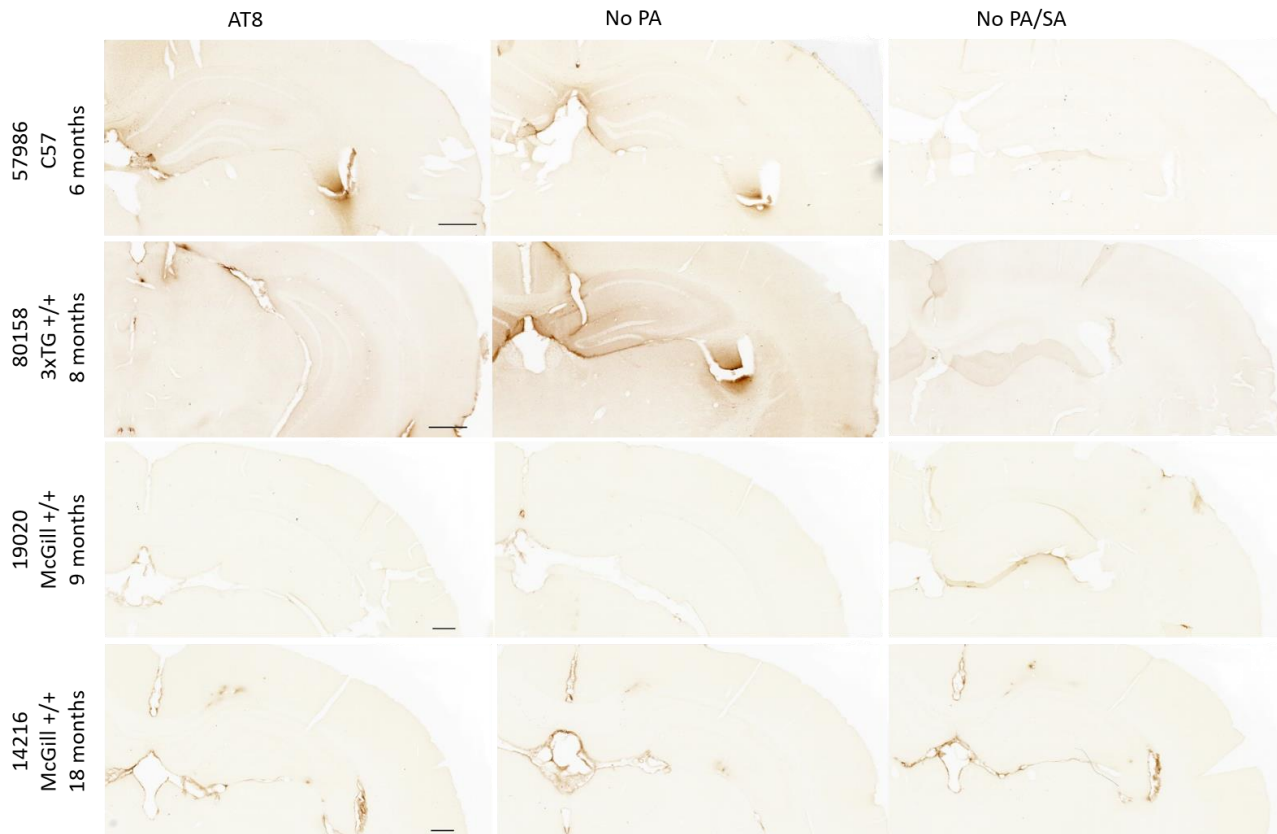


**Figure 38** AT8 immunostaining in other animal models. 6-month old female C57BL/6 mouse (57986), primary antibody (PA) AT8 (1:1000), biotinylated Goat anti-Mouse secondary antibody (SA) (1:500). 8-month old female 3xTG mouse (80158), AT8(1:1000), SA (1:1000). Rats McGill-R-Thy1-APP +/+ 9-month old female (19020), 18-month old female (14216), AT8 (1:1000), SA (1:1000). Scale bars = 500µm.

Immunostaining in a 6-month-old C57BL/6 (57986) and an 8-month old 3xTG (80158) mouse only showed slight diffuse labeling in the tissue. The reactivity was quite faint in the C57BL/6 mouse, and slightly stronger in the 3xTG-mouse. SA reactivity was mostly visibly in the molecular layer of the dentate gyrus, and unlike the APP/PS1, no plaque-like substances were apparent (Figure 18). When immunostaining tissue from the McGill-R-Thy1-APP rats, no reactivity was seen in either conditions. Also worthy of note, no p-Tau labeling was seen with AT8 PA in either 9-month old, or 18-month old homozygous McGill-R-Thy1-APP rats (Figure 18).

### 3.1.3 Testing with fluorescent secondary antibodies

To rule out the possibility of a problem uniquely tied to the biotinylated Goat anti-Mouse SA, fluorescent SA were tested in conjunction with the AT8 PA.

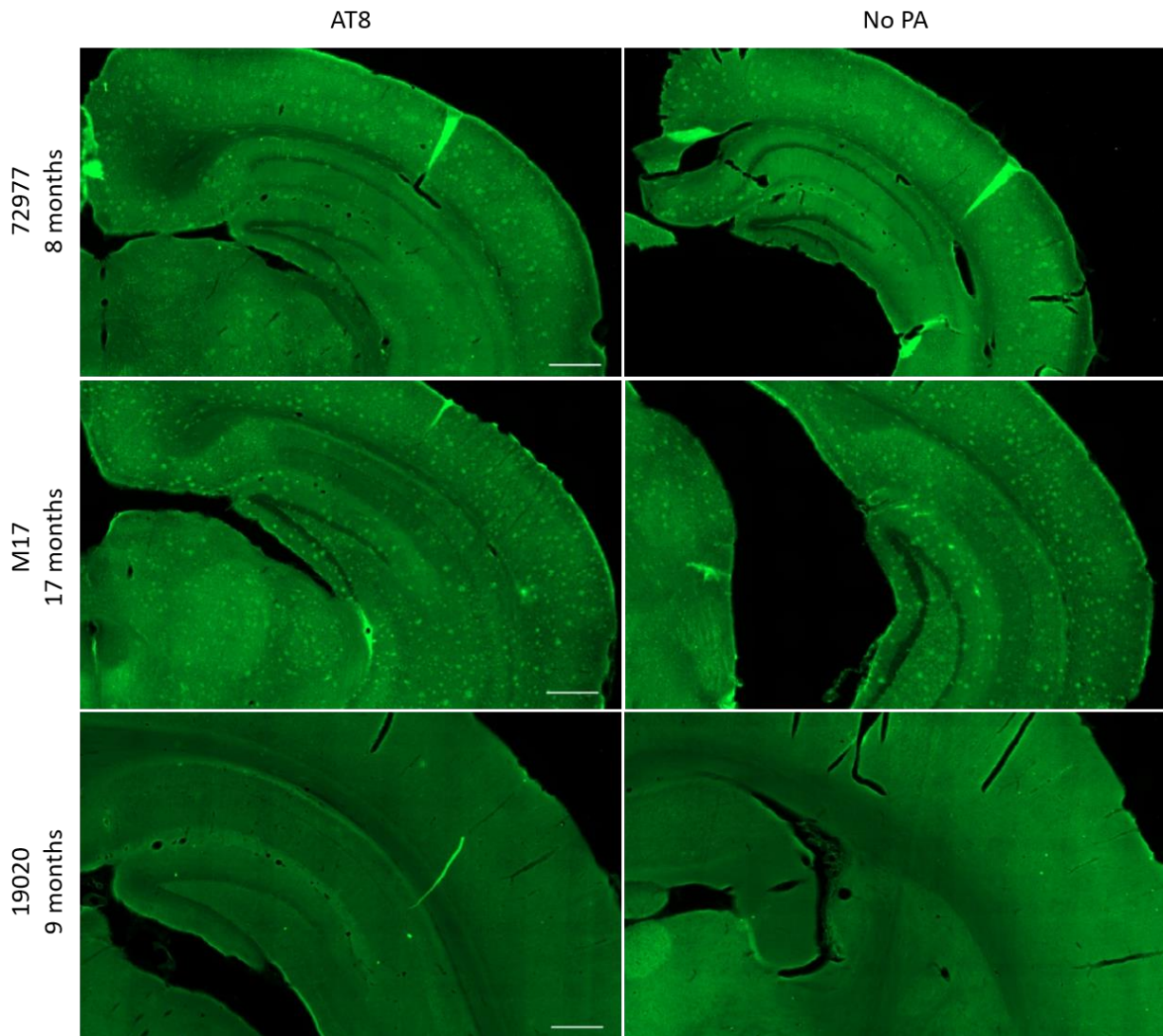


**Figure 19** AT8 immunostaining with fluorescent SA in APP/PS1 mice and McGill-R-Th1-APP rat. 8-month old male APP/PS1<sup>+/-</sup> x Odz3-P8117<sup>+/-</sup>;tetO-HM4 Mouse (72977), primary antibody (PA) AT8 (1:1000), secondary antibody Alexa Fluor 488 Goat anti-Mouse (SA) (1:1000). 17-month old male APP/PS1 mouse (M17), AT8 (1:1000), SA (1:1000). 9-month old female McGill-R-Thy1-APP rat (19020), AT8 (1:1000), SA (1:1000). Scale bars = 500 $\mu$ m

AT8 was tested in conjunction with Alexa Fluor 488 Goat anti-Mouse (Figure 19) and with Alexa Fluor 546 Goat anti-Mouse (not shown). In the APP/PS1 mouse, incubating with fluorescent SA alone resulted in non-specific binding similar to that of tissue incubated with both PA and fluorescent SA. Much like the reactivity with the biotinylated SA, high amounts of plaque-like deposits were visible with fluorescent SA. The plaque-like deposits were most pronounced in the neocortex in the 8-month old APP/PS1 mouse (72977). While in the 17-month old APP/PS1 mouse (M17), the plaque-like deposits were evenly distributed throughout the tissue. On the other hand, when testing AT8 with fluorescent SA in the

McGill-R-Thy1-APP rats, no reactivity was observed in either tissue incubated with both PA and SA, or tissue incubated in SA alone.

Further testing to attempt to reduce the non-specific binding of the SA in APP/PS1 mice were undertaken without success: Donkey anti-Mouse Alexa Fluor 488 SA was tested and yielded similar SA reactivity as Goat anti-Mouse Alexa Fluor 488 (Appendix 6.2.6). Attempts to use Tween-20 as a blocking agent also proved unsuccessful. 0.25% Tween-20 was added to incubation buffers for NGS, PA and SA. Non-specific binding by the SA was still highly present, albeit somewhat less than that of tissue from the same mouse processed without Tween-20 (Appendix 6.2.5).

### 3.1.4 Pre-incubating the secondary antibody reduces non-specific binding

The most successful method of reducing the non-specific binding of SA in the AT8 protocol was to pre-incubate the SA. This was done by incubating mouse tissue rostral to hippocampus, and caudal to EC, in the SA-buffer overnight, thereby pre-exposing the anti-mouse SA to mouse tissue, and saturating non-specific binding sites. The following day, the SA-buffer was extracted and then used for the AT8- protocol.

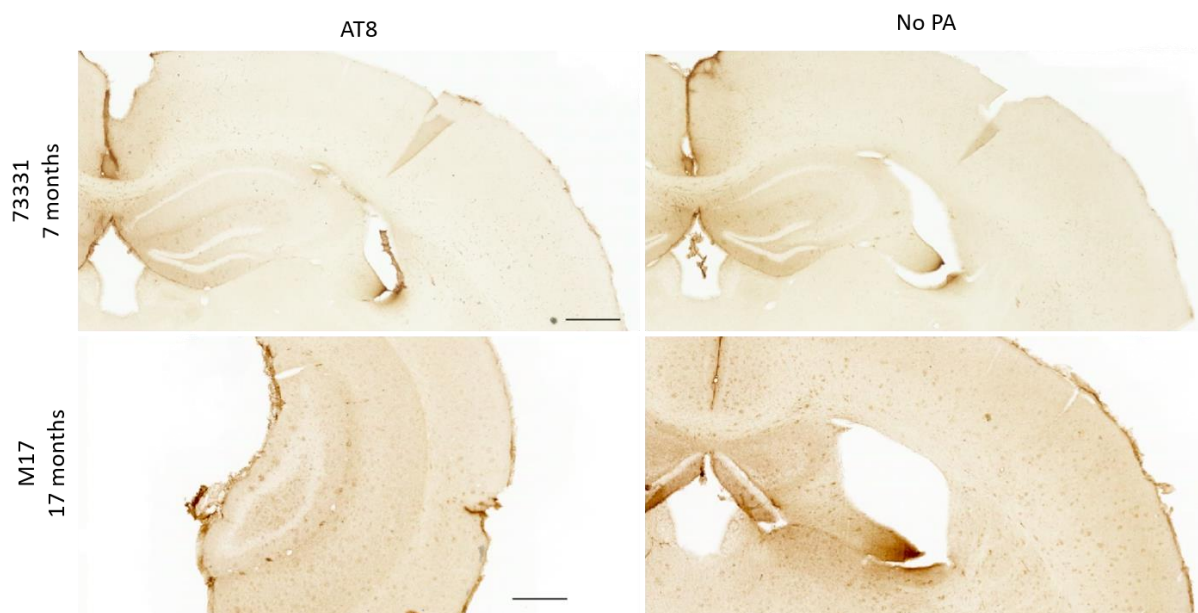


**Figure 20** AT8 immunostaining with pre-incubated secondary antibody. 7-month old male APP/PS1<sup>+/-</sup> x Odz3-P8117<sup>+/-</sup>;tetO-HM4<sup>+/-</sup> (73331), primary antibody (PA) AT8 (1:1000), biotinylated Goat anti-Mouse secondary antibody (SA) (1:500). 17-month male APP/PS1 mouse (M17), AT8 (1:1000), SA (1:1000). Scale bars = 500 $\mu$ m

Pre-incubating the secondary antibody resulted in lower amounts of non-specific binding in APP/PS1 tissue incubated with PA and SA, and in tissue incubated with SA only (Figure 20). Comparing the sections in Figure 17 to the sections of mice 73331 and M17 in Figure 20,

shows an overall less intense background reactivity, as well as fewer and smaller plaque-like substances.

The method of pre-incubating SA did not yield consistent results. When using the same method of pre-incubating the SA in a different APP/PS1 mouse, strong non-specific binding persisted (Figure 21).

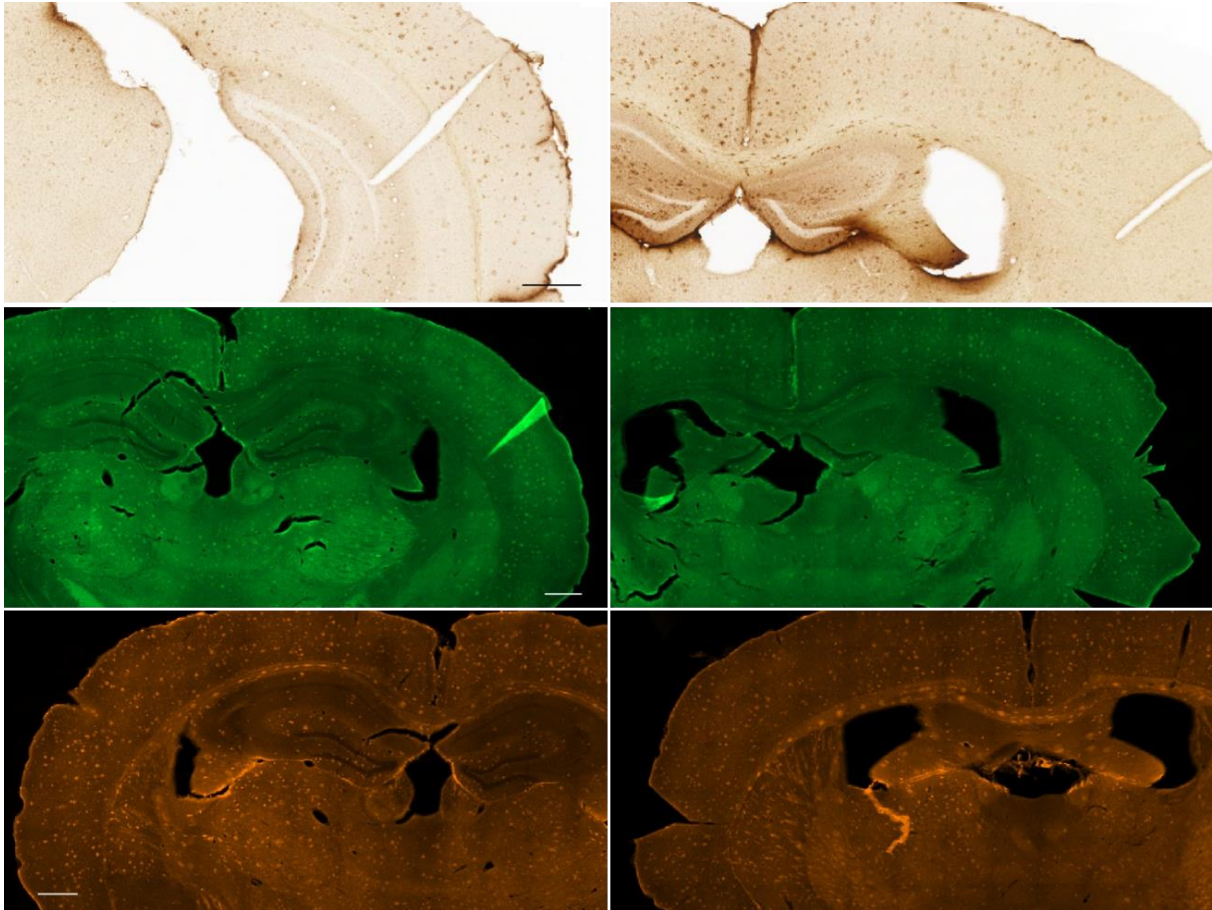


**Figure 21** AT8 immunostaining with pre-incubated secondary antibody in 9-month old female APP/PS1<sup>+/-</sup> x HM3-DDD<sup>+/-</sup>; Odz3-P8117<sup>+/-</sup> (72448). Primary antibody AT8 (1:1000), secondary antibodies (SA) (1:1000) biotinylated Goat anti-Mouse (top row), Alexa Fluor 488 Goat anti-Mouse (middle row), Alexa Fluor 546 Goat anti-Mouse (bottom row). Scale bars = 500 $\mu$ m

9-month old APP/PS1 mouse (72448) showed levels of non-specific binding similar to tissue processed without pre-incubated SA. The levels of background reactivity were consistent across biotinylated and fluorescent SA (Figure 21). Large amount of plaque-like substances were apparent and distributed evenly across the neocortex. Even with pre-incubating the SA, large variabilities in non-specific binding remained an issue (Figures 20 and 21).

Even when adjusting the protocol for non-specific binding, high background reactivity remained an issue in APP/PS1 mice, evidenced by the large variabilities in the pre-incubated APP/PS1 mice. Due to the inability to provide consistent results due to the amount of

background reactivity in the APP/PS1 mouse, the AT8 PA was replaced by the rabbit monoclonal antibody Ser396 to investigate potential changes in levels of p-tau.

### **3.2 Effects on p-Tau and GSK3 $\beta$ following reduction of reelin in entorhinal cortex layer II in the APP/PS1 mouse model**

#### *3.2.1 Reducing reelin in APP/PS1 76502 mouse results in increased levels of measured p-Tau and GSK3 $\beta$*

APP/PS1 mouse 76502 was injected with miRNA in the right cerebral hemisphere, control virus in the left cerebral hemisphere, with a viral interim of 2 months before being perfused at the age of 3 months. Mean levels of RE in miRNA-infected cells in the series stained for p-Tau and GSK3 $\beta$  were lowered by 62.6% and 62.8% respectively. This resulted in an increase of 48.5% in mean levels of measured p-Tau, and a 92.9% increase in mean levels of measured GSK3 $\beta$  (Figure 22).

Measured levels of RE was significantly lower in miRNA-infected EC LII cells (N = 22, Median (Mdn) = 0.07) compared to control virus-infected EC LII cells (N = 20, Mdn = 0.53) in the series stained for p-Tau (U = 5, p < 0.001, r = 0.84). Measured levels of RE was also significantly lowered in miRNA-infected EC LII cells (N = 39, Mdn = 0.13) compared to control virus-infected EC LII cells (N = 23, Mdn = 0.63) in the series stained for GSK3 $\beta$  (U = 0, p < 0.001, R = 0.83).. Measured levels of p-Tau was significantly higher in miRNA-infected EC LII cells (Mdn = 0.53) compared to control virus-infected EC LII cells (Mdn = 0.24) (U = 57, p < 0.001, r = 0.63). Levels of measured GSK3 $\beta$  was also significantly increased in miRNA-infected EC LII cells (Mdn = 0.72) compared to control virus-infected EC LII cells (Mdn = 0.38) (U = 28, p < 0.001, r = 0.78).

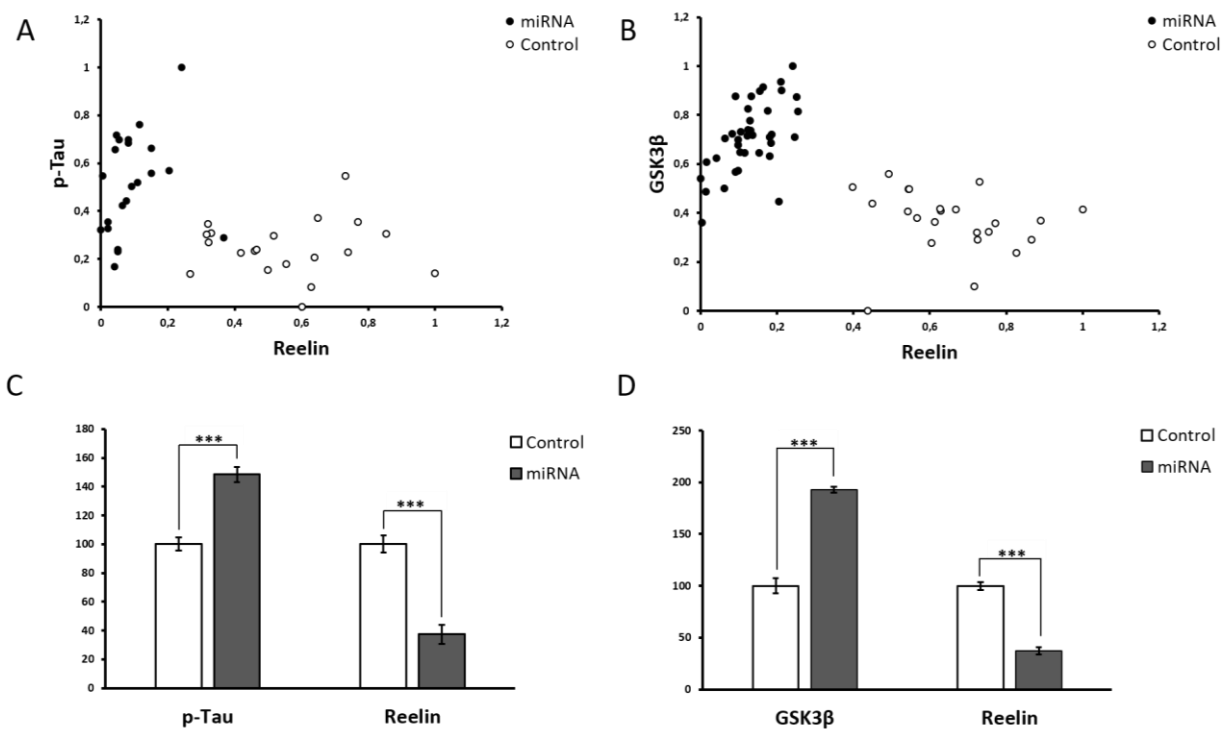


**Figure 22** Scatterplot and bar graphs displaying decreased levels in reelin (RE) and increased levels of measured p-Tau and GSK3 $\beta$  in miRNA-infected cells compared to control virus-infected cells in APP/PS1 mouse 76502. (A-B) Scatterplot shows control virus-infected cells (white) and miRNA-infected cells (black), normalized values of p-Tau/GSK3 $\beta$  intensity on the y-axis, normalized values of RE intensity on the x-axis. (C-D) Bar graphs displaying the mean percentage change in levels of RE, p-Tau and GSK3 $\beta$  in miRNA-infected cells (black), compared to control virus-infected cells (white), set to a value of 100. Error bars indicating  $\pm$  standard error of mean. \*\*\* = significance  $p < 0.001$ .

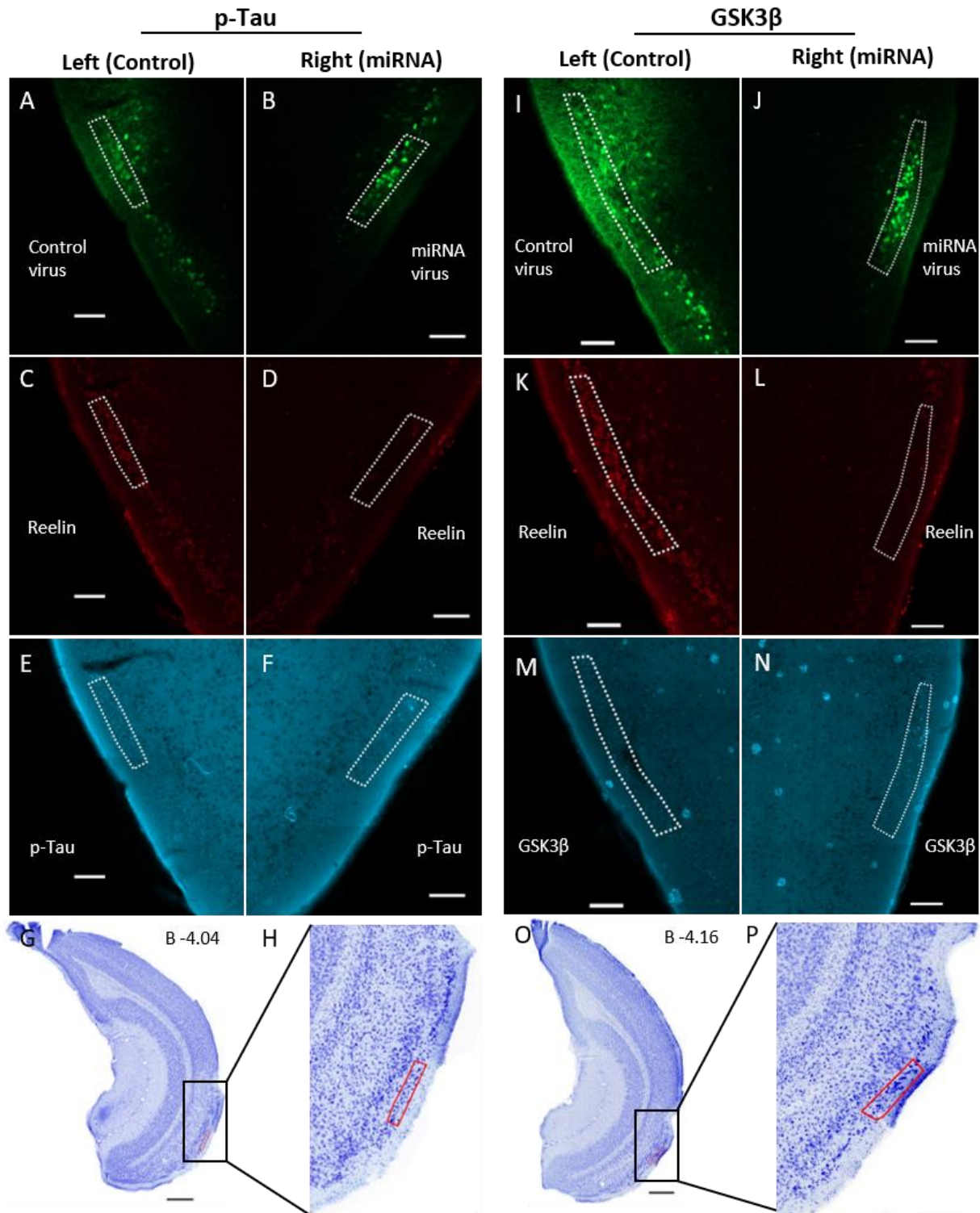


**Figure 234** Immunostaining of miRNA-injected APP/PS1 76502 with antibodies specific to p-Tau (A-F), GSK3 $\beta$  (I-N) and reelin (RE). Lowering expression of RE with miRNA-injection resulted in statistically higher levels of measured p-Tau and GSK3 $\beta$ . (A-B, I-J) Expression of GFP in control-infected (A, I) cells or miRNA-infected (B, J) cells. White dotted field indicates the region from which GFP-positive cells were selected for analysis. (C-D, K-L) Expression of RE (Alexa Fluor 635) in both hemispheres. (E-F, M-N) Expression of p-Tau/ GSK3 $\beta$  in both hemispheres (Alexa Fluor 546). (G-H, O-P) Nissl stained tissue of 6-month old C57BL/6 mouse at the corresponding bregma level for both miRNA- and control- hemispheres. Red field indicates the region of EC LII with GFP-positive cells selected for analysis. Scale bars = 100 $\mu$ m for fluorescent tissue, 500 $\mu$ m for Nissl sections.

### *3.2.2 Reducing reelin in APP/PS1+Ck2 mouse 75284 results in decreased levels of measured p-Tau and GSK3 $\beta$*

APP/PS1+Ck2 mouse 7584 was injected with miRNA in the right cerebral hemisphere, control virus in the left cerebral hemisphere, with a viral interim of 1 month before being perfused at the age of 3 months. Mean levels of RE in miRNA-infected cells in the series stained for p-Tau and GSK3 $\beta$  were lowered by 59.1% and 60% respectively. This resulted in a decrease of 25.1% in mean levels of measured p-Tau, and a 43.2% decrease in mean levels of measured GSK3 $\beta$  (Figure 24).

Measured levels of RE was significantly lower in miRNA-infected EC LII cells (N = 43, Mean (M) = 0.21, Standard deviation (SD) = 0.07) compared to control virus-infected EC LII cells (N = 45, M = 0.58, SD = 0.22) in the series stained for p-Tau ( $t(54,1) = 10.55$ ,  $p < 0.001$ ,  $d = 2.87$ ). Measured levels of RE was also significantly lower in miRNA-infected EC LII cells (N = 48, M = 0.15, SD = 0.1) compared to control virus-infected EC LII cells (N = 54, M = 0.55, SD = 0.19) in tissue stained for GSK3 $\beta$  ( $t(100) = 13.04$ ,  $p < 0.001$ ,  $d = 2.98$ ). Measured levels of p-Tau was significantly lower in miRNA-infected EC LII cells (M = 0.3, SD = 0.22) compared to control virus-infected EC LII cells (M = 0.48, SD = 0.28) ( $t(86) = 3.3$ ,  $p < 0.01$ ,  $d = 0.69$ ). Levels of measured GSK3 $\beta$  was also significantly lower in miRNA-infected EC LII cells compared to control virus-infected EC LII cells ( $t(100) = 7.94$ ,  $p < 0.001$ ,  $d = 1.59$ ).

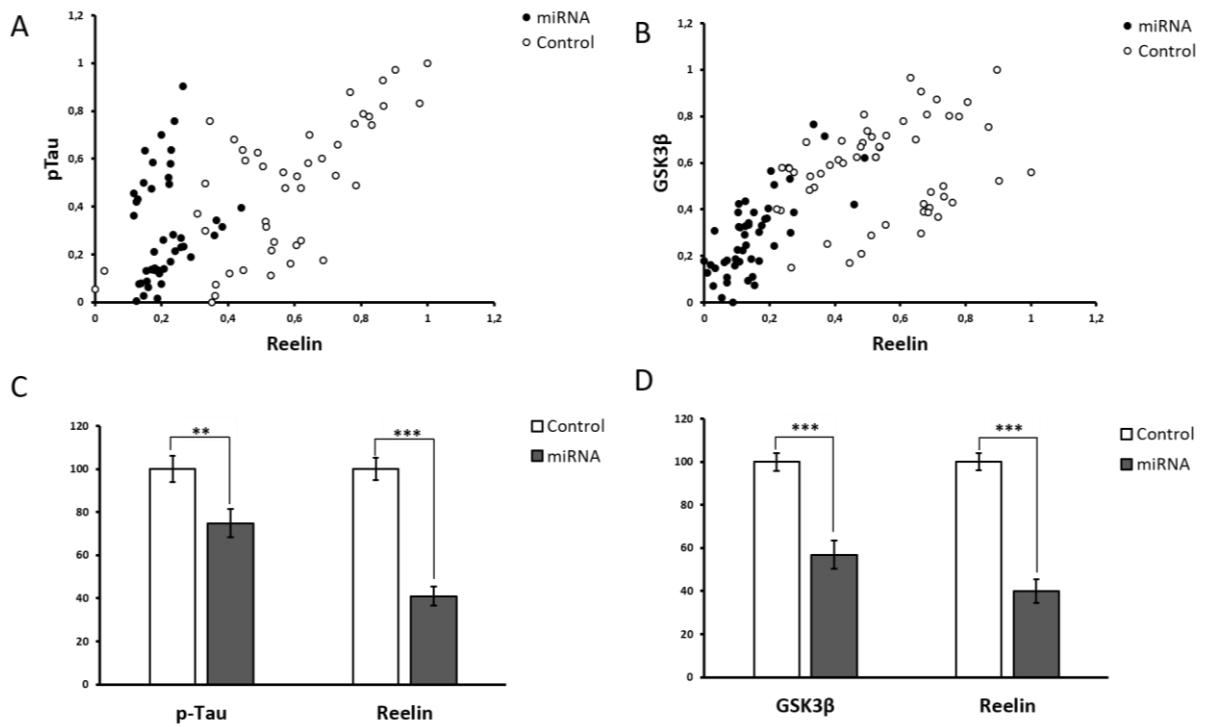


**Figure 245** Scatterplot and bar graphs displaying decreased levels in reelin (RE), p-Tau and GSK3β in miRNA-infected cells compared to control virus-infected cells in APP/PS1 mouse 75824 (A-B). Scatterplot shows control virus-infected cells (white) and miRNA-infected cells (black), normalized values of p-Tau/GSK3β intensity on the y-axis, normalized values of RE intensity on the x-axis. (C-D) Bar graphs displaying the mean percentage change in measured levels of RE, p-Tau and GSK3β in miRNA-infected cells (black), compared to control virus-infected cells (white) set to a value of 100. Error bars indicating  $\pm$  standard error of mean. \*\* = significance  $p < 0.01$ , \*\*\* = significance  $p < 0.001$ .

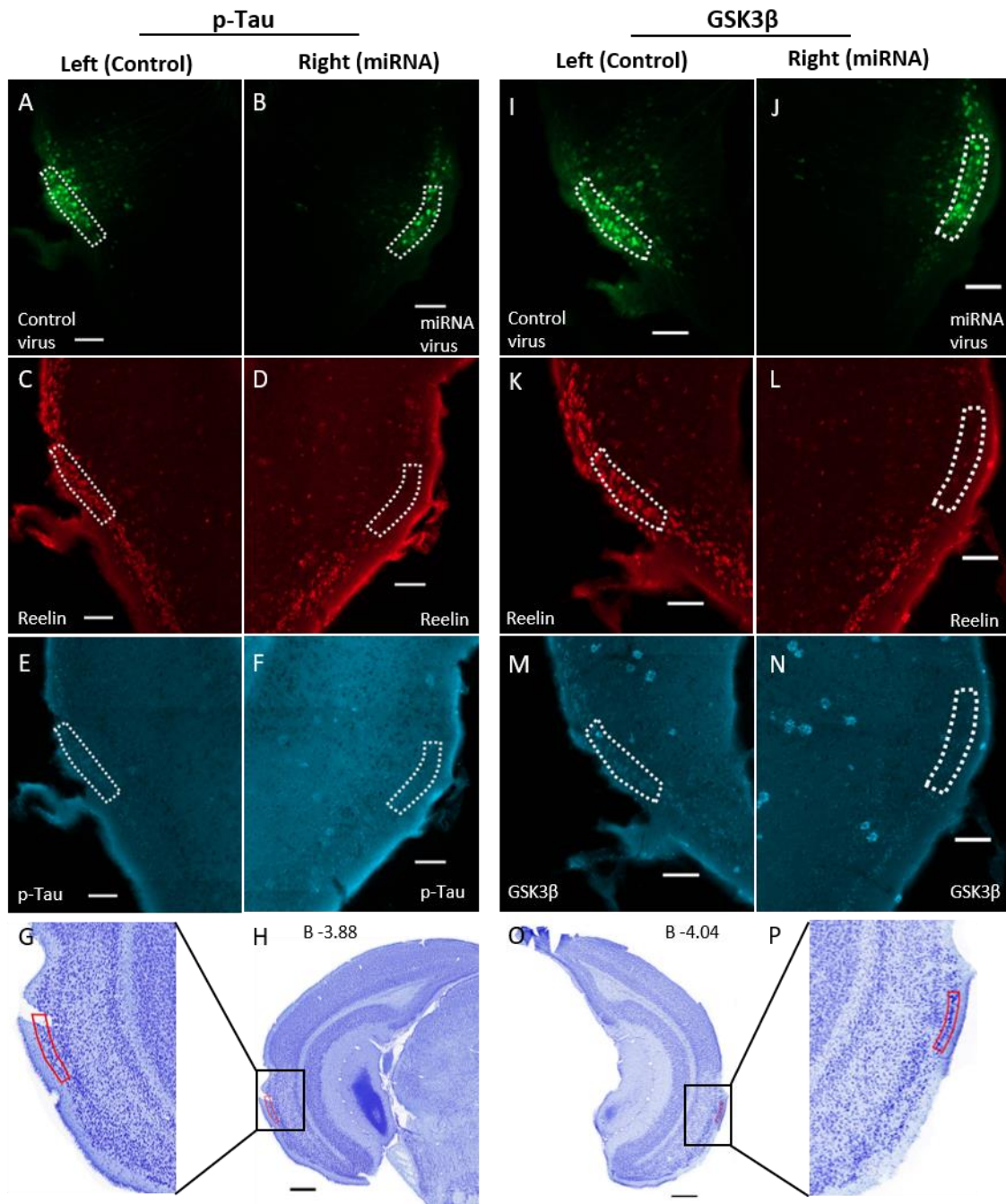


**Figure 256** Immunostaining of miRNA-injected APP/PS1 75284 with antibodies specific to p-Tau (A-F), GSK3 $\beta$  (I-N) and reelin (RE). Lowering expression of RE with miRNA-injection resulted in statistically significant lower levels of measured p-Tau and GSK3 $\beta$ . (A-B, I-J) Expression of GFP in control-infected (A, I) cells or miRNA-infected (B, J) cells. White dotted field indicates the region from which GFP-positive cells were selected for analysis. (C-D, K-L) Expression of RE (Alexa Fluor 635) in both hemispheres. (E-F, M-N) Expression of p-Tau/GSK3 $\beta$  in both hemispheres (Alexa Fluor 546). (G-H, O-P) Nissl stained tissue of 6-month old C57BL/6 mouse at the corresponding bregma level for both miRNA- and control-hemispheres. Red field indicates the region of EC LII with GFP-positive cells selected for analysis. Scale bars = 100 $\mu$ m for fluorescent tissue, 500 $\mu$ m for Nissl sections.

### **3.3 Effects on p-Tau and GSK3 $\beta$ following reduction of reelin in entorhinal cortex layer II in the 3xTG mouse model**

#### *3.3.1 Reducing reelin in 3xTG 77132 mouse did not alter the levels of measured p-Tau or GSK3 $\beta$ .*

3xTG mouse 77132 was injected with miRNA in the left cerebral hemisphere, control virus in the right cerebral hemisphere, with a viral interim of 7 months before being perfused at the age of 8 months. Mean levels of RE in miRNA-infected cells in the series stained for p-Tau and GSK3 $\beta$  were lowered by 5.2% and 54.8% respectively. This did result in altered levels of measured p-Tau or GSK3 $\beta$  (Figure 26).

Measured levels of RE was significantly lower in miRNA-infected EC LII cells (N = 69, M = 0.08, SD = 0.05) compared to control virus- infected EC LII cells (N = 54, M = 0.38, SD = 0.27) in the series stained for p-Tau ( $t(56.2) = 8.09$ ,  $p < 0.001$ ,  $d = 2.16$ ). Measured levels of RE was also significantly lower in miRNA-infected EC LII cells (N = 107, M = 0.11, SD = 0.07) compared to control virus-infected EC LII cells (N = 100, M = 0.33, SD = 0.22) in the series stained for GSK3 $\beta$  ( $t(119,2) = 9.3$ ,  $p < 0.001$ ,  $d = 1.7$ ). Measured levels of p-Tau indicated a non-significant reduction in miRNA-infected cells (M = 0.28, SD = 0.15) compared to control virus-infected cells (M = 0.36, SD = 0.29) ( $t(76.3) = 1.88$ ,  $p = 0.064$ ,  $d = 0.43$ ). Measured levels of GSK $\beta$  was not statistically different in miRNA-infected cells (M = 0.47, SD = 0.19) compared to control virus-infected cells (M = 0.50, SD = 0.19) ( $t(205) = 1.079$ ,  $p = 0.282$ ,  $d = 0.15$ ).

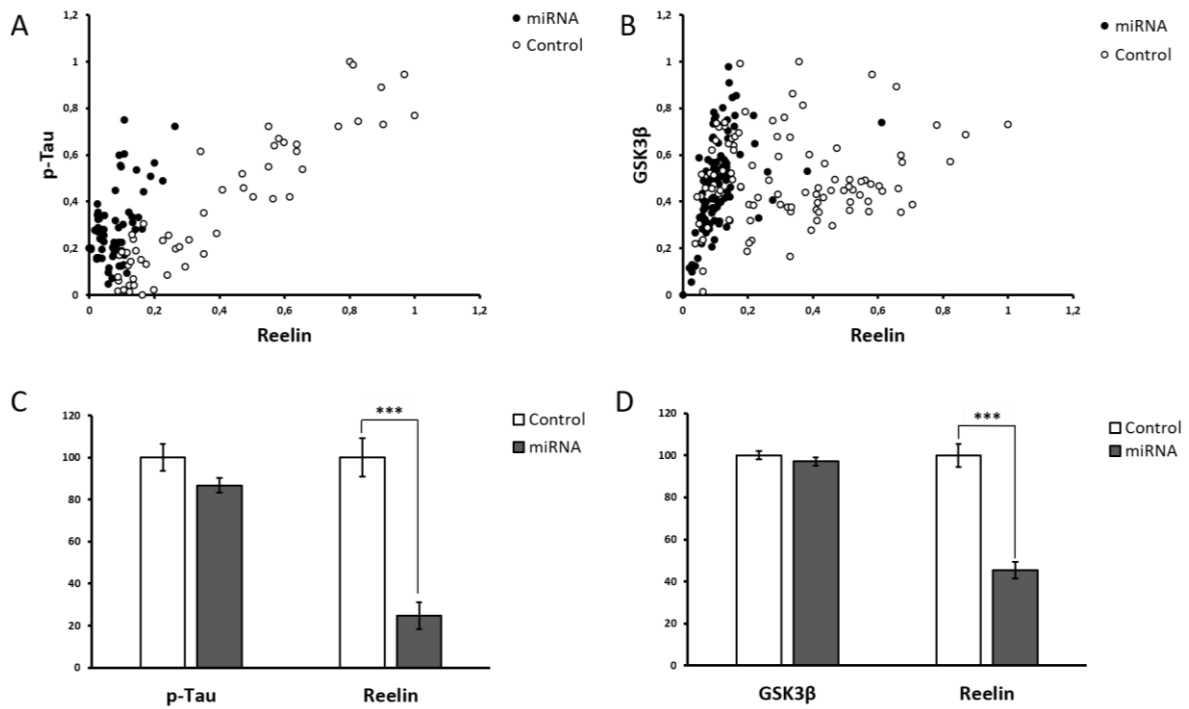


**Figure 26** Scatterplot and bar graphs displaying decreased levels in reelin (RE), but no statistically significant changes in either p-Tau or GSK3β in miRNA-infected cells compared to control virus-infected cells in 3xTG mouse 77132. (A-B) Scatterplots shows control virus-infected cells (white) and miRNA-infected cells (black), normalized values of p-Tau/GSK3β intensity on the y-axis, normalized values of RE intensity on the x-axis. (C-D) Bar graphs displaying the mean percentage change in measured levels of RE, p-Tau and GSK3β in miRNA-infected cells (black), compared to control virus-infected cells (white) set to a value of 100. Error bars indicating ± standard error of mean. \*\*\* = significance  $p < 0.001$ .

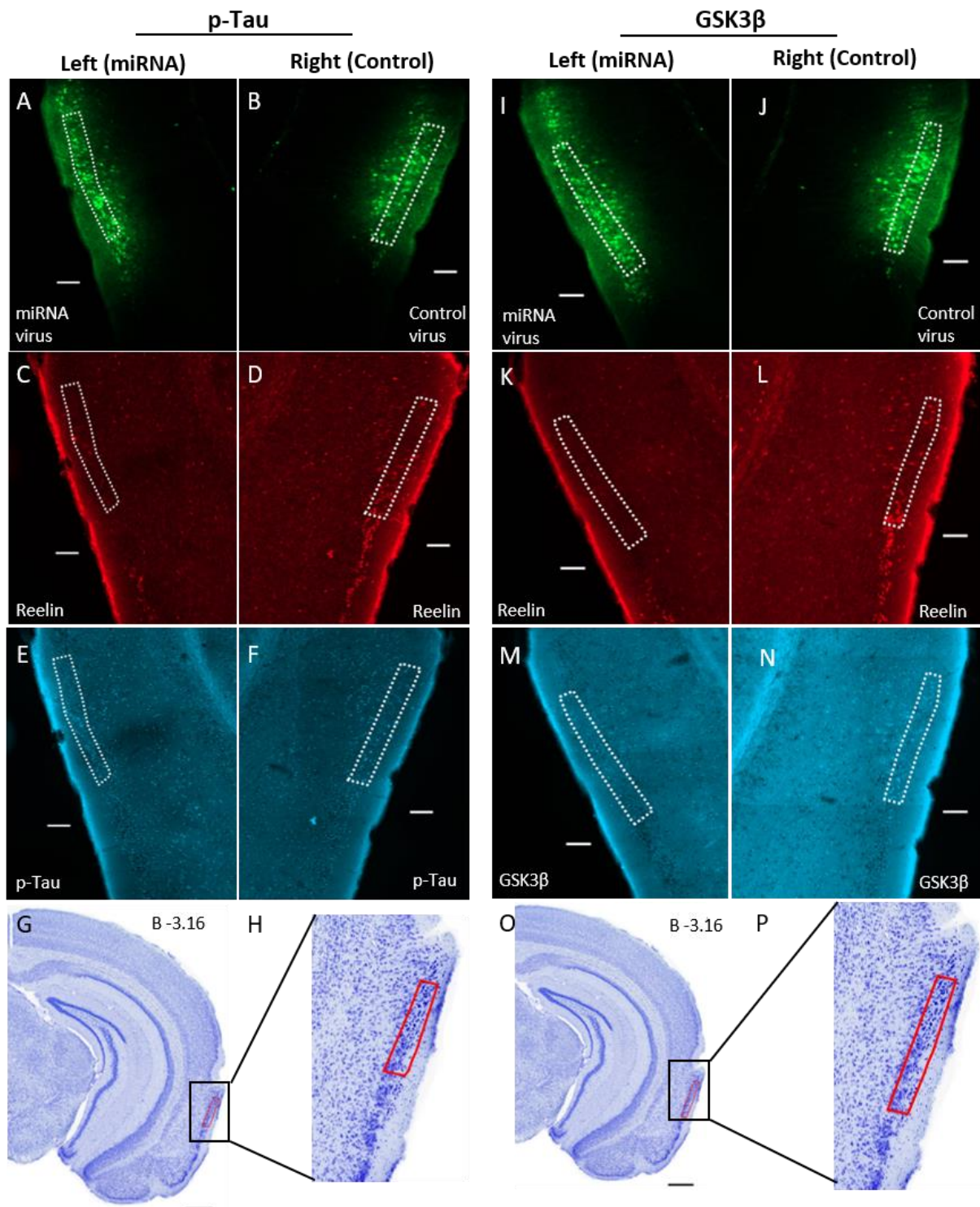


**Figure 277** Immunostaining of miRNA-injected 3xTG 77132 with antibodies specific for p-Tau (A-F), GSK3 $\beta$  (I-N) and reelin (RE). Lowering expression of RE in EC LII did not result in statistically significant reduction of measured levels of p-Tau or GSK3 $\beta$ . (A-B, I-J) Expression of GFP in miRNA-infected cells (A, I) and control virus-infected cells (B, J). White dotted field indicates the region from which GFP-positive cells were selected for analysis. (C-D, K-L) expression of RE (Alexa Fluor 635) in both hemispheres. (E-F, M-N) Expression of p-Tau/GSK3 $\beta$  (Alexa Fluor 546) in both hemispheres. (G-H, O-P) Nissl stained tissue of 6-month old C57BL/6 mouse at the corresponding bregma level for both miRNA and control-hemispheres. Red field indicates the region of EC LII with GFP-positive cells selected for analysis. Scale bars = 100 $\mu$ m for fluorescent tissue, 500 $\mu$ m for Nissl sections

### **3.4 Effects on p-Tau following reduction of reelin in entorhinal cortex layer II in the McGill-R-Thy1-APP rat model**

Four McGill-R-Thy1-APP rats were injected with the miRNA RE virus in combination with contralateral injection of control virus. All rats were perfused at 3 months of age, two months post-injection.

#### *3.4.1 Reducing reelin in McGill-R-Thy1-APP rat 25180 results in reduced levels of measured p-Tau*

McGill-R-Thy1-APP rat 25180 was injected with the miRNA virus in the right cerebral hemisphere and with control virus in the left cerebral hemisphere. Mean levels of RE in miRNA-infected cells were lowered by 67.6%. This resulted in a reduction of 49.9% in mean levels of p-Tau.

Measured levels of RE were significantly lower in miRNA-infected EC LII cells ( $N = 272$ ,  $M = 0.07$ ,  $SD = 0.04$ ), compared to control virus-infected EC LII cells ( $N = 259$ ,  $M = 0.31$ ,  $SD = 0.20$ ) ( $t(279.58) = 18.59$ ,  $p < 0.001$ ,  $d = 2.22$ ). Measured levels of p-Tau was reduced significantly lower in miRNA-infected EC LII cells ( $N = 272$ ,  $M = 0.16$ ,  $SD = 0.07$ ) compared to control virus-infected EC LII cells ( $N = 259$ ,  $M = 0.38$ ,  $SD = 0.15$ ) ( $t(371.87) = 22.47$ ,  $p < 0.001$ ,  $d = 2.33$ ) (Figure 28A-B).

#### *3.4.2 Reducing reelin in McGill-R-Thy1-APP rat 25181 results in increased levels of measured p-Tau*

McGill-R-Thy1-APP rat 25181 was injected with the miRNA virus in the left cerebral hemisphere and with control virus in the right cerebral hemisphere. Mean levels of RE in miRNA-infected cells were lowered by 93.6%. This resulted in an increase of 34.1% in mean levels of p-Tau.

Measured levels of RE were significantly lower in miRNA-infected EC LII cells ( $N = 58$ ,  $M = 0.03$ ,  $SD = 0.02$ ) compared to control virus-infected EC LII cells ( $N = 68$ ,  $M = 0.56$ ,  $SD = 0.17$ ) ( $t(69.08) = 25.15$ ,  $p < 0.001$ ,  $d = 6.05$ ). Measured levels of p-Tau was increased significantly in miRNA-infected EC LII cells ( $N = 58$ ,  $M = 0.56$ ,  $SD = 0.16$ ), compared to control virus-infected EC LII cells ( $N = 68$ ,  $M = 0.36$ ,  $SD = 0.14$ ) ( $t(124) = 7.39$ ,  $p < 0.001$ ,  $d = 1.33$ ) (Figure 28C-D).

### *3.4.3 Measured levels of reelin and p-Tau was not significantly altered in McGill-R-Thy1-APP rat 25561*

McGill-R-Thy1-APP rat 25561 was injected with the miRNA virus in the right cerebral hemisphere and with the control virus in the left cerebral hemisphere.

Measured levels of RE saw no statistically significant change in miRNA-infected EC LII cells (N = 28, Mdn = 0.33) compared to control virus-infected EC LII cells (N = 27, Mdn = 0.25) (U = 318, p = 0.312, r = 0.14). Measured levels of p-Tau in miRNA-infected cells (N = 28, Mdn = 0.20) indicated a non-significant reduction in comparison to control-virus infected EC LII cells (N= 27, Mdn = 0.75) (U = 343, p = 0.556, r = 0.08) (Figure 28E-F).

### *3.4.4 Reducing reelin in McGill-R-Thy1-APP rat 25562 results in decreased levels of measured p-Tau*

McGill-R-Thy1-APP rat 25562 was injected with the miRNA virus in the left cerebral hemisphere and with the control virus in the right cerebral hemisphere. Mean levels of RE in miRNA-infected cells were lowered by 72.6%. This resulted in a reduction of 23.8% in mean levels of p-Tau

Measured levels of RE were significantly lower in miRNA-infected EC LII cells (N = 126, M = 0.10, SD = 0.06) compared to control virus-infected EC LII cells (N = 125, M = 0.46, SD = 0.20) (t(148.56) = 19.38, p < 0.001, d = 3.18). Measured levels of p-Tau was significantly reduced in miRNA-infected EC LII cells (N = 126, M = 0.29, SD = 0.17) compared to control virus-infected EC LII cells (N = 125, M = 0.38, SD = 0.21) (t(237.21) = 3.38, p < 0.001, d = 0.48) (Figure 28G-H).

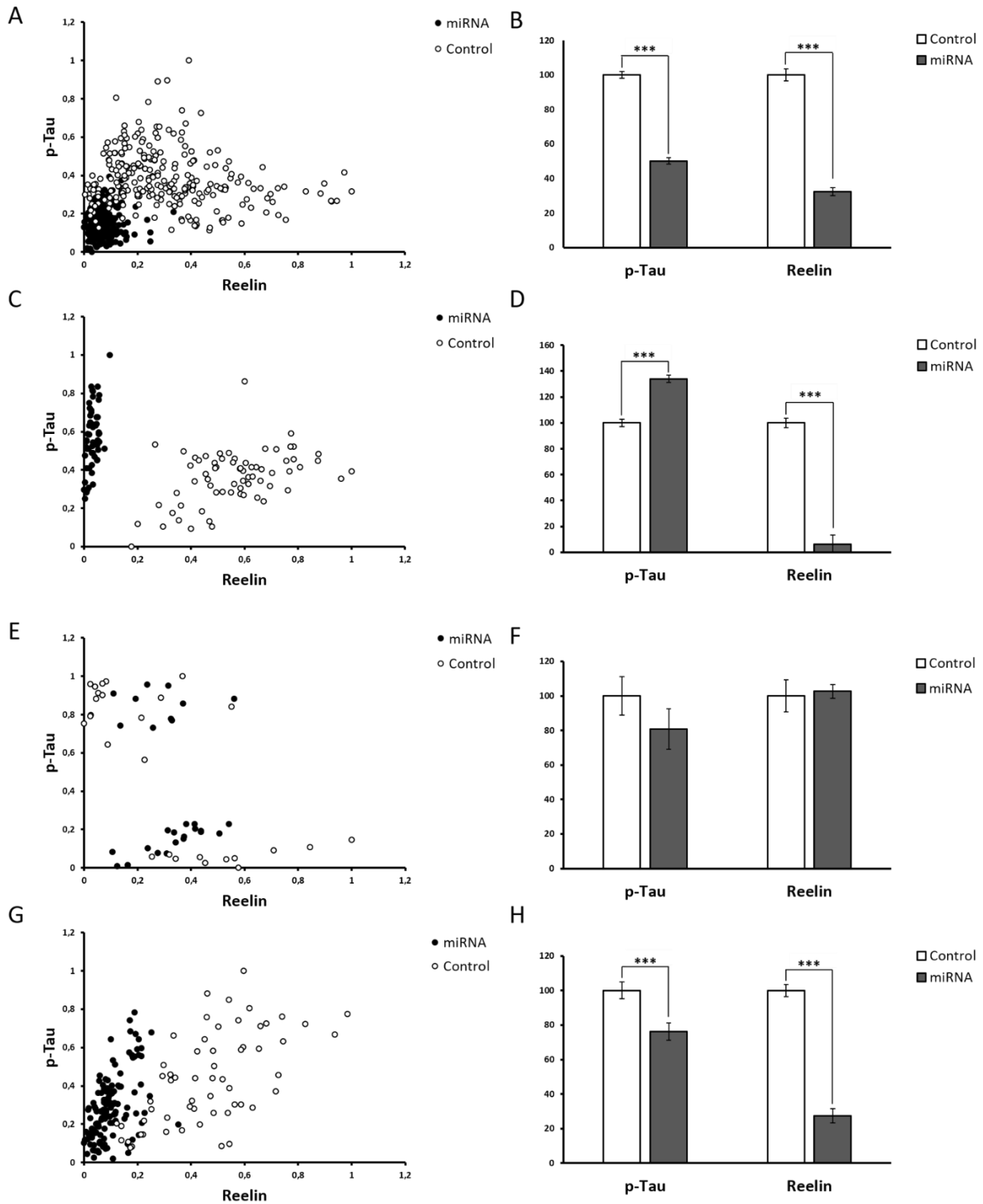


**Figure 28** Scatterplot and bar graphs for all McGill-R-Thy1-APP rats with miRNA reelin (RE) virus injected in LEC. Scatterplots show control virus-infected cells (white) and miRNA-infected cells (black), normalized values of p-Tau intensity on the y-axis, normalized values of RE intensity on the x-axis. Bar graphs displays the mean percentage change in measured levels of RE and p-Tau in miRNA-infected cells (black), compared to control virus-infected cells (white) set to a value of 100. (A-B) Decreased levels of measured RE and p-Tau in miRNA-infected cells in rat 25180. (C-D) Decrease in measured RE and increase in measured p-Tau in miRNA-infected cells in rat 25181. (E-F) No statistically significant change in measured levels of RE or p-Tau in rat 25561. (G-H) Decreased levels of measured RE and p-Tau in miRNA-infected cells in rat 25562. Error bars indicating  $\pm$  standard error of mean. \*\*\* = significance  $p < 0.001$ .

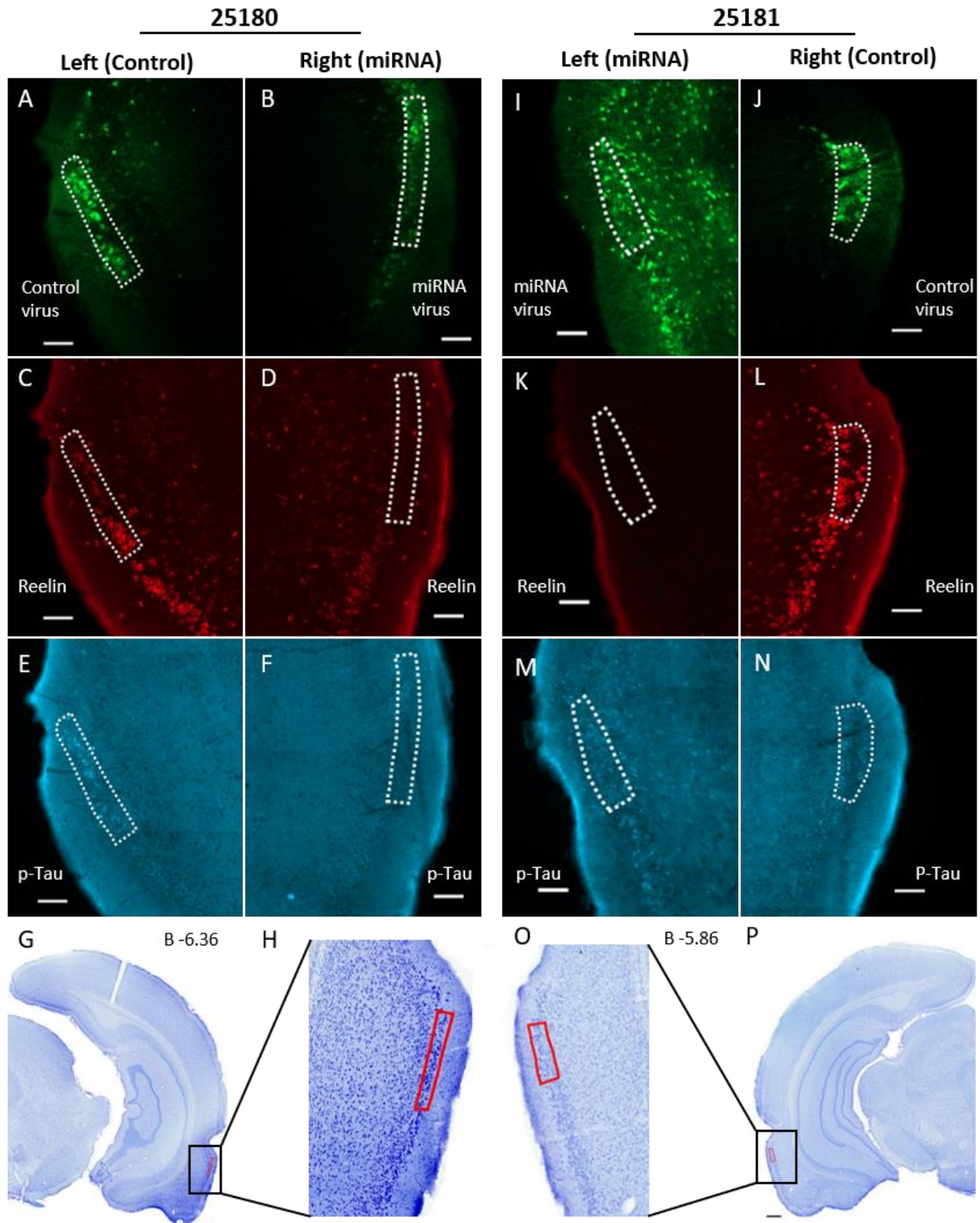


**Figure 29** Immunostaining of miRNA-injected McGill-R-Thy1-APP rats 25180 (A-F) and 25181 (I-N) with antibodies specific for p-Tau and reelin (RE). Reducing expression of RE in EC LII resulted in statistically significant decrease of p-Tau in 25180, and statistically significant increase in 25181. (A-B, I-J) Expression of GFP in miRNA-injected cells (A, I) and control virus-infected cells (B, J). White dotted field indicates the region from which GFP-positive cells were selected for analysis. (C-D, K-L) expression of RE (Alexa Fluor 635) in both hemispheres. (E-F, M-N) Expression of p-Tau (Alexa Fluor 546) in both hemispheres. (G-H, O-P) Nissl stained tissue of 5-month-old McGill-R-Thy1-APP  $+/+$  rat at the corresponding bregma level for both miRNA and control-hemispheres. Red field indicates the region of EC LII with GFP-positive cells selected for analysis. Scale bars = 100µm for fluorescent tissue, 500µm for Nissl sections.

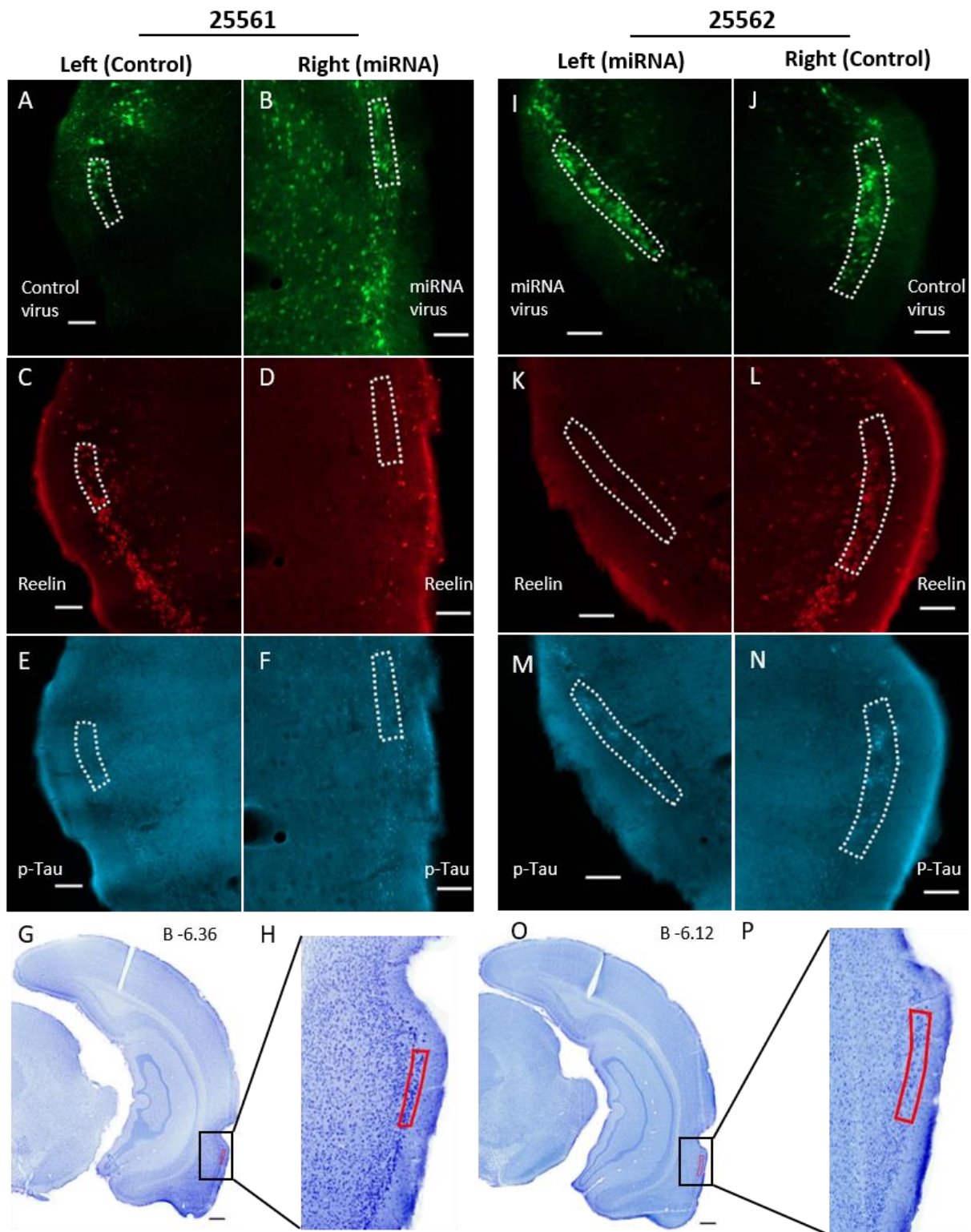


**Figure 30** Immunostaining of miRNA-injected McGill-R-Thy1-APP rats 25561 (A-F) and 25562 (I-N) with antibodies specific for p-Tau and reelin (RE). Neither RE nor p-Tau levels were altered with statistical significance in rat 25561. Reducing expression of RE in EC LII resulted in statistically significant decrease of p-Tau in 25562. (A-B, I-J) Expression of GFP in miRNA-infected cells (A, I) and control virus-infected cells (B, J). White dotted field indicates the region from which GFP-positive cells were selected for analysis. (C-D, K-L) expression of RE (Alexa Fluor 635) in both hemispheres. (E-F, M-N) Expression of p-Tau (Alexa Fluor 546) in both hemispheres. (G-H, O, P) Nissl stained tissue of 5-month-old McGill-R-Thy1-APP  $+/+$  rat at the corresponding bregma level for both miRNA and control-hemispheres. Red field indicates the region of EC LII with GFP-positive cells selected for analysis. Scale bars = 100µm for fluorescent tissue, 500µm for Nissl sections.

## **4. Discussion**

### **4.1 Summary of main findings**

The aim of this thesis is to investigate potential effects on levels of GSK3 $\beta$  and p-Tau following the lowering of the expression of RE in EC LII neurons in animal models of AD, including the APP/PS1, 3xTG and McGill-R-Thy1-APP models. By stereotaxic injection of a novel viral construct containing miRNA targeted to interfere with translation of RE, RE was successfully lowered EC LII neurons in the experimental hemisphere in nearly all studied animals. In contrast, the effects on measured levels of p-Tau and GSK3 $\beta$ , by way of quantification of immunofluorescence, in neurons infected with RE miRNA, were mixed. In the APP/PS1 mice, statistically significant increases of p-Tau and GSK3 $\beta$  was detected in one mouse. However, p-Tau and GSK3 $\beta$  were significantly decreased in another age-matched APP/PS1 mouse. As for the 3xTG mouse, a non-significant trend towards a decrease in p-Tau was detected, however GSK3 $\beta$  levels remained unchanged. Four McGill-R-Thy1-APP rats were analyzed. Statistically significant decreases in p-Tau was seen in two rats, while for one rat I found a statistically significant increase in p-Tau. The fourth rat did not show any significant decrease in levels of p-Tau, but also had no apparent reduction in levels of RE in the experimental hemisphere.

### **4.2 Non-specific binding of mouse secondary antibody in APP/PS1 mice**

Due to its frequent use on mouse tissue, the mouse monoclonal antibody AT8 was initially planned to be the used as the main PA to measure potential changes in p-Tau. However, this was later decided against due to large amounts of background staining in APP/PS1 tissue, which I discovered by be due to the SA. In particular, the non-specific binding of the SA in APP/PS1 mouse tissue was apparent in sections that were processed without PA. The non-specific binding was much more severe in APP/PS1 mice compared to C57 WT mouse and 3xTG mice, which only had slight diffuse labeling at most (Figure 18). Different types SAs were tested with the aim of reducing background reactivity, but to no avail. Biotinylated and different fluorescent SA all produced the same type of non-specific binding. Changing the SA species from goat to donkey produced similar amounts of non-specific binding. Conversely, no signal of AT8 or SA was detected in rat tissue. Based on the observations that the SA produces background reactivity in mice tissue, that the reactivity is

not a result of unspecific DAB deposits, and that the reactivity is more or less the same whether or not biotinylated or fluorescent SA is used, it is reasonable to conclude that the background reactivity seen when incubating with SA is a result of mouse-on-mouse cross-reactivity.

It is worth noting that the testing of the AT8 PA, and the subsequent attempts to minimize non-specific binding of the SA, was regarded as a technical issue and was not intended as a systematic study of the matter. The findings are presented here as part of the results, due to the widespread use of AT8 in mice tissue, and due to the fact that the APP/PS1 mouse model is a much-used transgenic animal model in AD research. The findings are only presented visually, with no quantification of the background levels. Only non-injected animals were used for the purpose of establishing a working AT8 protocol and lowering non-specific binding of mouse SA. When testing a protocol, two sections from each mouse were marked as controls, where one section was incubated without PA, and the other section was incubated with neither PA nor SA. Background reactivity was easily detectable in the neocortex of APP/PS1 mice, and for this reason, I would often use sections rostral to the hippocampal formation for controls in order to not waste tissue containing hippocampus or EC. By doing so, sections containing hippocampus or EC was tested for possible AT8-positive signal that potentially could be differentiated from the non-specific binding. For this reason, the results in section 3.1.1 contain micrograph comparisons of widely different brain regions. However, the presence or absence of background reactivity is readily apparent despite comparisons of two sections on different rostrocaudal levels. This ought to make the comparisons between different brain regions relatively unproblematic for the purposes of this thesis.

The non-specific binding of the SA in APP/PS1 mice had similar appearance to that of A $\beta$ -plaques. The plaque-like substances were more or less evenly distributed throughout the tissue and were especially apparent in the neocortex and hippocampal formation (Figure 16). Most of these plaque-like substances were similar in appearance to diffuse A $\beta$ -plaques, while some plaque-like substances were similar to dense-core A $\beta$ -plaques. No plaque-like substances were observed in 1-month old APP/PS1 mouse (Figure 17) but were widely apparent in a 5-month old APP/PS1 mouse (Figure 16). Although no APP/PS1 mice between the age of 1 and 5 months were tested, this is consistent with the onset of A $\beta$ -deposition reported by Radde et al., where A $\beta$  is reported to accumulate in the cortex after 6 weeks<sup>106</sup>. Based on the age of onset, the morphology of the plaque-like substances, it is highly likely that these in fact are, A $\beta$ -plaques. However, this was not verified, since no anti-A $\beta$  PA were

used, since the purposes of the testing was specific to the anti-tau AT8 PA, and various mouse SAs.

The AT8 protocols and various tests for reducing background reactivity had to be tested in the APP/PS1 tissue I had available at the time. For this reason, some of the APP/PS1 mice were taken from a colony crossbred with other strains, the latter with the purpose of enabling selective expression of viral vectors (see Appendix 6.1). Whether or not this might have affected the amount of non-specific binding of the SA seems unlikely but cannot be ruled out. Gender differences in background reactivity was not investigated. The majority of APP/PS1 mice used in these tests happened to be male. However, as seen Figure 21, a 9-month female APP/PS1 mouse (72448) also displayed large amounts of non-specific binding. Gender differences in A $\beta$ -plaque deposition in similar APP/PS1 models has previously been observed<sup>165</sup>. I did not systematically investigate differences in background reactivity as a function of age. Non-specific binding was apparent in APP/PS1 mice ranging from 5-months to 17-months of age.

Due to the large amount of A $\beta$  plaque deposits apparent in the APP/PS1 model from an early age, the APP/PS1 might be extra susceptible to issues with non-specific binding when using mouse antibodies. The results presented here in regard to non-specific binding of mouse SA in APP/PS1 mouse model, should at the very least serve as a reminder of the importance of including controls in immunohistochemistry protocols. Establishing the amount of background reactivity can enable the subtraction from the actual signal stemming from the PA, but this required careful investigation under the conditions of the pipeline and materials at hand. Most importantly, by including immunohistochemistry controls, one avoids the risk of analyzing false positives.

Additional blocking measures like increasing NGS concentration, adding additional NGS in PA/SA incubations, incubation with Tween-20, and pre-incubating the SA prior to use, was not sufficient to reduce background reactivity in APP/PS1 tissue. Perhaps, one could have attempted additional different blocking agents like bovine serum albumin, or dry milk. However, to remedy non-specific binding on this scale, the best bet would have to be purchase of either pre-adsorbed SA, or a mouse-on-mouse blocking kit. Due to the planned use of relatively young APP/PS1 mice in terms of potential NFT-pathology, the observed amount of cross-reactivity was deemed unacceptable. It was thus decided that the AT8 PA should be dropped in favor of a rabbit monoclonal PA specific for p-Tau Ser396. This latter PA, along with its appropriate SA, proved to prevent background signal.

## **4.3 Reducing reelin expression in layer II of the entorhinal cortex yields mixed results with respect to levels of p-Tau and GSK3 $\beta$**

### *4.3.1 APP/PS1 mice*

Two male, 3-month old APP/PS1 mice were analyzed. Both mice had similar reduction of RE levels in miRNA-infected cells (around 60%). In each APP/PS1 mouse, the measured levels of GSK $\beta$  went in the same direction as p-Tau levels, indicating that there might be a connection between GSK3 $\beta$  Tyr216 and p-Tau Ser396. Still, the two APP/PS1 mice had divergent measures of p-Tau and GSK3 $\beta$  compared to one another. The reason(s) why one mouse had significant increases in p-Tau and GSK3 $\beta$ , while the other had significant decreases in p-Tau and GSK3 $\beta$  remains unclear. It is conceivable that if more APP/PS1 mice could be included in the analysis, the results would cumulatively point in one direction. However, of the injected mice, a large number had to be excluded owing to lack of viral expression (see section 2.6.1). There were also overall, less GFP-infected cells available for analysis in mouse 76502 than in mouse 75284. Additionally, out of both series stained for p-Tau and GSK3 $\beta$  in mouse 76502, only one section in each series were viable for analysis, due to low expression of the viral constructs. On the other hand, the viral expression in mouse 75284 were much higher across sections, and multiple sections were analyzed for both p-Tau and GSK3 $\beta$ . This means, when comparing the two APP/PS1 mice, fluorescence intensity of one single section in mouse 76502, is compared to the summed values of multiple section in 75284. There could be large variability in overall fluorescence intensity between sections, and this might drive the overall result in one direction or obfuscate the results overall. Although there isn't any indication of a section in 75284 with suspiciously high fluorescence intensity, there are indications of this being the case in some of the other analyzed animals. This will be discussed further in section 4.4.1.

Interestingly, GSK3 $\beta$  Tyr216 emits strong signal in what appears to be A $\beta$ -plaques in APP/PS1 mice (Figure 23 M-N, Figure 25 M-N). Unlike what is described in section 4.2, this cannot be attributed to background reactivity in the APP/PS1 model. When establishing protocols for the GSK3 $\beta$  Tyr216 PA, the control sections incubated without PA were consistently negative. However, one cannot conclude with certainty that these are A $\beta$ -plaques, since no anti-A $\beta$  counterstain has been performed in conjunction with the GSK3 $\beta$  PA. GSK3 $\beta$  has been reported to co-localize with dystrophic neurites and NFTs, and active GSK3 $\beta$  phosphorylated at Tyr216 being detectable in pre-tangle neurons<sup>166-168</sup>. To my knowledge,

GSK3 $\beta$  Tyr216 immunoreactivity in A $\beta$ -plaques has not been observed in the APP/PS1 model prior to this.

#### 4.3.2 *3xTG mice*

One 8-month old male 3xTG mouse was analyzed. RE was markedly reduced in miRNA-infected cells compared to control virus-infected cells. However, no statistically significant changes in neither p-Tau nor GSK3 $\beta$  were observed. In the series stained for p-Tau, two sections were viable for analysis. Looking at the scatterplot (Figure 24A), it is evident that a cluster of control virus-infected cells all score very high in levels of RE and p-Tau. When investigating the raw data from each section, it seems like these cells all stem from the same section. If one were to consider this cluster as outliers, this 3xTG mouse would have statistically significant increase in p-Tau. This might indicate that there is a variability in overall fluorescence intensity between sections, and this variability can affect the result.

Unlike in the APP/PS1 model, no plaque-like GSK3 $\beta$  immunoreactivity was observed in the 3xTG mouse model. This is not unexpected, since A $\beta$ -plaque deposition in the hippocampus and neocortex occurs in the 3xTG mouse model by 12-15 months, much later than in the APP/PS1 model<sup>106, 147</sup>

#### 4.3.3. *McGill-R-Thy1-APP rat model*

Four 3-month old McGill-R-Thy1-APP rats were analyzed. RE was significantly reduced in miRNA-infected cells in three of the rats, and out of these three, two rats had statistically significant reductions in p-Tau, while the third had statistically significant increase in p-Tau. As was the case with the APP/PS1 mice, the results are also divergent in the McGill-R-Thy1-APP rats, and the reason for this remains unclear. The number of cells quantified in the rat tissue is overall much greater than in the mice tissue. However, there is a large variability in the number of analyzed cells between the three McGill-R-Thy1-APP rats. In rat 25180 where p-Tau was reduced, a total of 531 cells were quantified. While in rat 25181, which had an increase in p-Tau, 126 cells total were quantified. Whether or not discrepancies like this in the total number of analyzed cells could influence the overall results is unknown, thus this cannot be ruled out. However, the fact that cells were only selected if they were within the same part of the dorsolateral EC, falling along the same extent from the rhinal sulcus, may be taken to indicate that the discrepancies between animals are not due to variations in numbers of neurons.

The fourth McGill-R-Thy1-APP rat was the only animal in this thesis in which *measured* levels of RE was not lowered. Oddly enough, visual inspection of expressed RE seems to indicate that RE has been reduced, meaning that the miRNA virus must have had an effect (Figure 30 C-D). In the experimental hemisphere, no clearly defined LII of RE immunoreactive neurons remain, only some sporadic RE-positive cells are visible. A look at the respective scatter plot, reveals two distinct clusters of cells, with control- and miRNA-infected cells intermixed. Also, only 55 cells total were eligible for analysis. This was due to poor expression of control virus, as well as damage to one hemisphere.

#### **4.4 Tau in rodent animal models for AD**

Two of transgenic animal models for AD used in this thesis, are primarily considered models for amyloid pathology, since they are carrying variants of APP and/or PS1 mutations. Conversely, the third model used, namely the 3xTG mouse model, carries human MAPT with the P301L mutation along with APP and PS1 mutations.

In the case of the APP/PS1 model, the original paper by Radde et al. mentions A $\beta$ -plaques being surrounded by p-Tau-positive neuritic processes detectable by AT8 immunostaining. However, this was first detectable at 8 months, and no mature tangle pathology was observed<sup>106</sup>. However, some studies have detected positive tau signal with PAs specific to Ser396 at 6-, and 7-months, using western blotting<sup>169, 170</sup>. The McGill-R-Thy1-APP rat model is known to be devoid of NFT pathology<sup>171</sup>. Consistent with this, no AT8 immunoreactivity was detected in an un-injected 18-month old homozygous McGill-R-Thy1-APP rat (Figure 18). The APP/PS1 mice and McGill-R-Thy1-APP rats studied here were all 3 months old, which in respect to potential NFT pathology in these models, must be regarded as being very young.

The 3xTG mouse model show both A $\beta$ - and NFT pathology. In the original description of the model, the onset of tau-pathology happens in the hippocampus and does not occur until the 3xTG mice reach about 12 months of age. Phosphorylation of Ser396 is first detectable in the hippocampus at 18 months of age<sup>172</sup>. The 3xTG mouse analyzed in this thesis was 8 months old, which of course is older in comparison to the APP/PS1 and McGill-R-Thy1-APP rats used in this study, but in regards to expected onset of tau pathology in the 3xTG model, 8 months is still quite young. A different study of the tau pathology of the 3xTG model found that the P301L transgene product could not be detected in the EC until 12 months of age, nor does it accumulate with further aging. Also, a limited number of Ser396 immunoreactive cells were detectable in the EC only at 26 months of age<sup>173</sup>. Considering this, the 3xTG mouse

model is unsuitable for studying tau-related pathology in the EC, despite it being the only animal model with a tau-mutation presented in this thesis.

When considering the tau pathology, or lack thereof, that has previously been reported regarding the three transgenic animal models used in this project, the measured levels of p-Tau in EC might be so minute, that even small differences in methodological variability may outweigh any biological differences, giving rise to discrepant results that reflect artefacts.

## **4.5 Methodological considerations**

### *4.5.1 Scanning*

The variabilities in fluorescence intensity between sections could be a result of errors in the scanning procedure. Each series were scanned using the same scanner settings, in order to preserve the same fluorescence intensity throughout the series. Some sections were for some reason very difficult to scan in focus and had to be rescanned multiple times. When this happened, the relevant tissue marked for analysis were re-scanned together in order to avoid photobleaching in one section only. Another technical issue to consider, might be tiling effects in the scanned tissue, where one square has slightly different focus settings than the adjacent square, which might impact the readout of fluorescence intensity. It seems unlikely that this could have distorted the results of all animals, but in the case of McGill-R-Thy1-APP rat 25561, a technical issue related to tissue scanning might explain the seemingly random distribution of the scatter plot.

### *4.5.2 Stereotaxic injections*

One should not rule out the possibility of levels of p-Tau potentially being affected by the injection of the control-virus. Earlier studies have demonstrated that hyperphosphorylation of tau can occur due to external stimuli, such as hypothermia, anesthesia and hypoxia<sup>174, 175</sup><sup>176</sup>. To control for the possibility that control virus or the stress of the injection itself could have an impact on p-Tau, animals injected with control-virus only ought to be investigated in the continuation of the larger project this master's thesis is a part of.

## **4.6 Future directions**

A big challenge in studying tau pathology related to AD in transgenic animals, is that the tau pathology observed in transgenic mouse and rat models is very different from the tau-

pathology seen in human AD-patients. As previously discussed in section 4.4, the onset of tau-pathology in the 3xTG mouse occurs in the hippocampus, not in EC LII as it does in humans<sup>111</sup>. If there is a connection between RE and GSK3 $\beta$  and/or p-Tau, this needs to be studied in EC LII where RE is present.

An additional challenge is the use of tau mutations specific to frontotemporal dementia in transgenic animal models for AD. The ratio of tau isoforms that are hyperphosphorylated in frontotemporal dementia, are different to the ratio of tau isoforms that are hyperphosphorylated in AD. Neurofibrillary tangles in human AD consist of all six tau isoforms at ratio of 1:1 between 3R tau and 4R tau<sup>177</sup>. Whereas in frontotemporal dementia, only 4R isoforms are part of NFTs<sup>178</sup>. To have the full range of tau isoforms in AD transgenic animal models should be a goal to aim for when developing the next generation of transgenic animal models for AD. Mouse models for expressing the entire human MAPT gene, in the absence of mouse MAPT gene, effectively replicating human tau isoform splicing, has also been developed<sup>177</sup>. These types of mice could be interesting to crossbreed with other existing AD- or tauopathy animal models, to see if tau pathology would manifest itself closer to that of human AD. Another step in the right direction, would be to focus on establishing novel transgenic rat models with NFT pathology. This is important due to the fact that the rat brain already express all six isoforms of tau, albeit with a different ratio of 3R tau to 4R tau (9:1) than in humans<sup>91</sup>. Still, a transgenic rat model might simulate tau neuropathology closer to that seen in humans, which in turn might be critical in understanding the underlying mechanisms of the disease process.

As for future directions with this project, increasing the age of the animals studied would be preferable. According to the amyloid cascade hypothesis, tau-pathology is downstream from the A $\beta$ -oligomerization<sup>69</sup>. Consistent with this, the APP/PS1 and 3xTG models develop tau-pathology after onset of A $\beta$ -pathology<sup>106, 172</sup>. If the goal is to study p-Tau, then the animals studied need to be old enough to have had time to develop NFT pathology. This might require quite a long time, which might not be feasible nor cost-effective. Alternatively, one could shift focus from p-Tau to investigating tau kinases like GSK3 $\beta$  or CDK5. It is well established at this point that increased activity or decreased inhibition of tau protein kinases leads to p-Tau. By focusing on tau kinases, one could perhaps rely on using younger animals. Also, one could bypass the issues of lack of full tau isoform expression in mice and rats, since the mechanisms leading to p-Tau are being studied, not p-Tau itself.

## **4.7 Conclusions**

The aim of this thesis was to investigate a possible relationship between RE and p-Tau in EC LII. It was hypothesized that reducing expression of RE in EC LII, would lead to an observable increase in both GSK3 $\beta$  and p-Tau. The results from this thesis demonstrate that stereotaxic injection of a novel RE miRNA virus is an effective means of lowering expressed RE in EC LII in different transgenic animal models for AD. Conversely, no consistent change was observed with respect to levels of p-Tau and GSK3 $\beta$  in EC LII.

## 5. References

1. World Health Organization. Global action plan on the public health response to dementia 2017–2025. Geneva: World Health Organization. 2017.
2. Vermunt L, Sikkes SAM, van den Hout A, Handels R, Bos I, van der Flier WM, et al. Duration of preclinical, prodromal, and dementia stages of Alzheimer's disease in relation to age, sex, and APOE genotype. *Alzheimers Dement*. 2019;15(7):888-98.
3. Beason-Held LL, Goh JO, An Y, Kraut MA, O'Brien RJ, Ferrucci L, et al. Changes in brain function occur years before the onset of cognitive impairment. *The Journal of neuroscience : the official journal of the Society for Neuroscience*. 2013;33(46):18008-14.
4. Förstl H, Kurz A. Clinical features of Alzheimer's disease. *European Archives of Psychiatry and Clinical Neuroscience*. 1999;249(6):288-90.
5. Kukull WA, Brenner DE, Speck CE, Nochlin D, Bowen J, McCormick W, et al. Causes of Death Associated with Alzheimer Disease: Variation by Level of Cognitive Impairment Before Death. *Journal of the American Geriatrics Society*. 1994;42(7):723-6.
6. 2020 Alzheimer's disease facts and figures. *Alzheimer's & Dementia*. 2020;16(3):391-460.
7. Alzheimer A. Über eine eigenartige Erkrankung der Hirnrinde. *Allgemeine Zeitschrift für Psychiatrie und phychish-Gerichtliche Medizin*. 1907;64:146-8.
8. Stelzmann RA, Schnitzlein HN, Murtagh FR. An English translation of Alzheimer's 1907 paper, "Über eine eigenartige Erkankung der Hirnrinde". *Clinical anatomy (New York, NY)*. 1995;8(6):429-31.
9. Grøntvedt GR, Schröder TN, Sando SB, White L, Bråthen G, Doeller CF. Alzheimer's disease. *Current Biology*. 2018;28(11):R645-R9.
10. Ryan NS, Rossor MN, Fox NC. Alzheimer's disease in the 100 years since Alzheimer's death. *Brain*. 2015;138(12):3816-21.
11. Hippus H, Neundörfer G. The discovery of Alzheimer's disease. *Dialogues Clin Neurosci*. 2003;5(1):101-8.
12. Kraeplin E. *Psychiatrie*. 8th ed. Vol I: Allgemeine Psychiatrie; Vol II: Klinische Psychiatrie. Leipzig, Germany: Barth;1910.
13. Kidd M. Paired Helical Filaments in Electron Microscopy of Alzheimer's Disease. *Nature*. 1963;197(4863):192-3.
14. Blessed G, Tomlinson BE, Roth M. The association between quantitative measures of dementia and of senile change in the cerebral grey matter of elderly subjects. *Br J Psychiatry*. 1968;114(512):797-811.
15. Roth M, Tomlinson BE, Blessed G. Correlation between Scores for Dementia and Counts of 'Senile Plaques' in Cerebral Grey Matter of Elderly Subjects. *Nature*. 1966;209(5018):109-10.
16. Roth M, Tomlinson BE, Blessed G. The relationship between quantitative measures of dementia and of degenerative changes in the cerebral grey matter of elderly subjects. *Proc R Soc Med*. 1967;60(3):254-60.
17. Tomlinson BE, Blessed G, Roth M. Observations on the brains of demented old people. *J Neurol Sci*. 1970;11(3):205-42.
18. Tomlinson BE, Blessed G, Roth M. Observations on the brains of non-demented old people. *J Neurol Sci*. 1968;7(2):331-56.
19. Alzheimer A. über eigenartige Krankheitsfälle des späteren Alters. *Zeitschrift für die gesamte Neurologie und Psychiatrie*. 1911;4(1):356.

20. Glenner GG, Wong CW. Alzheimer's disease: initial report of the purification and characterization of a novel cerebrovascular amyloid protein. *Biochemical and biophysical research communications*. 1984;120(3):885-90.
21. Glenner GG, Wong CW. Alzheimer's disease and Down's syndrome: Sharing of a unique cerebrovascular amyloid fibril protein. *Biochemical and biophysical research communications*. 1984;122(3):1131-5.
22. Masters CL, Simms G, Weinman NA, Multhaup G, McDonald BL, Beyreuther K. Amyloid plaque core protein in Alzheimer disease and Down syndrome. *Proceedings of the National Academy of Sciences of the United States of America*. 1985;82(12):4245-9.
23. Hyman BT, Van Hoesen GW, Damasio AR, Barnes CL. Alzheimer's disease: cell-specific pathology isolates the hippocampal formation. *Science (New York, NY)*. 1984;225(4667):1168-70.
24. Grundke-Iqbal I, Iqbal K, Quinlan M, Tung YC, Zaidi MS, Wisniewski HM. Microtubule-associated protein tau. A component of Alzheimer paired helical filaments. *The Journal of biological chemistry*. 1986;261(13):6084-9.
25. Iqbal K, Grundke-Iqbal I, Zaidi T, Merz PA, Wen GY, Shaikh SS, et al. Defective brain microtubule assembly in Alzheimer's disease. *Lancet (London, England)*. 1986;2(8504):421-6.
26. Grundke-Iqbal I, Iqbal K, Tung YC, Quinlan M, Wisniewski HM, Binder LI. Abnormal phosphorylation of the microtubule-associated protein tau (tau) in Alzheimer cytoskeletal pathology. *Proceedings of the National Academy of Sciences of the United States of America*. 1986;83(13):4913-7.
27. Kosik KS, Joachim CL, Selkoe DJ. Microtubule-associated protein tau (tau) is a major antigenic component of paired helical filaments in Alzheimer disease. *Proceedings of the National Academy of Sciences of the United States of America*. 1986;83(11):4044-8.
28. Moscovitch M, Cabeza R, Winocur G, Nadel L. Episodic Memory and Beyond: The Hippocampus and Neocortex in Transformation. *Annu Rev Psychol*. 2016;67:105-34.
29. Gold CA, Budson AE. Memory loss in Alzheimer's disease: implications for development of therapeutics. *Expert Rev Neurother*. 2008;8(12):1879-91.
30. Witter MP, Amaral DG. Hippocampal formation. In: Paxinos G, editor. *The Rat Nervous System*. 3. San Diego, California: Elsevier Academic Press; 2004. p. 635-704.
31. Cappaert NLM, Van Strien NM, Witter MP. Chapter 20 - Hippocampal Formation. In: Paxinos G, editor. *The Rat Nervous System (Fourth Edition)*. San Diego: Academic Press; 2015. p. 511-73.
32. Strange BA, Witter MP, Lein ES, Moser EI. Functional organization of the hippocampal longitudinal axis. *Nature reviews Neuroscience*. 2014;15(10):655-69.
33. Witter MP, Doan TP, Jacobsen B, Nilssen ES, Ohara S. Architecture of the Entorhinal Cortex A Review of Entorhinal Anatomy in Rodents with Some Comparative Notes. *Frontiers in systems neuroscience*. 2017;11:46.
34. Kjonigsen LJ, Leergaard TB, Witter MP, JG B. Digital atlas of anatomical subdivisions and boundaries of the rat hippocampal region: *Frontiers in Neuroinformatics*; 2011 [5:2:[Available from: [http://cmbn-navigator.uio.no/rat\\_hippocampus\\_atlas/](http://cmbn-navigator.uio.no/rat_hippocampus_atlas/)].
35. Insausti R, Herrero M, Witter M. Entorhinal cortex of the rat: Cytoarchitectonic subdivisions and the origin and distribution of cortical efferents. *Hippocampus*. 1998;7:146-83.

36. Doan TP, Lagartos-Donate MJ, Nilssen ES, Ohara S, Witter MP. Convergent Projections from Perirhinal and Postrhinal Cortices Suggest a Multisensory Nature of Lateral, but Not Medial, Entorhinal Cortex. *Cell Reports*. 2019;29(3):617-27.e7.
37. Witter MP. The perforant path: projections from the entorhinal cortex to the dentate gyrus. *Progress in brain research*. 2007;163:43-61.
38. Yau SS-Y, Li A, So K-F. Involvement of Adult Hippocampal Neurogenesis in Learning and Forgetting. *Neural plasticity*. 2015;2015.
39. van Strien NM, Cappaert NLM, Witter MP. The anatomy of memory: an interactive overview of the parahippocampal–hippocampal network. *Nature Reviews Neuroscience*. 2009;10(4):272-82.
40. Kibro-Flatmoen A, Witter MP. Neuronal chemo-architecture of the entorhinal cortex: A comparative review. *The European journal of neuroscience*. 2019.
41. Nilssen ES, Doan TP, Nigro MJ, Ohara S, Witter MP. Neurons and networks in the entorhinal cortex: A reappraisal of the lateral and medial entorhinal subdivisions mediating parallel cortical pathways. *Hippocampus*. 2019.
42. Cajal SR. Estudios sobre la corteza cerebral humana: IV. Estructura de la corteza cerebral olfativa del hombre y mamíferos 1901.
43. de N6 RL. Studies on the structure of the cerebral cortex I The area entorhinalis. *Journal Fur Psychologie und Neurologie*. 1933;45:381-438.
44. Perl DP. Neuropathology of Alzheimer's Disease. *Mount Sinai Journal of Medicine: A Journal of Translational and Personalized Medicine*. 2010;77(1):32-42.
45. Gomez-Isla T, Spire T, De Calignon A, Hyman BT. Neuropathology of Alzheimer's disease. *Handb Clin Neurol*. 2008;89:233-43.
46. Masliah E. Mechanisms of synaptic dysfunction in Alzheimer's disease. *Histol Histopathol*. 1995;10(2):509-19.
47. Marsh J, Alifragis P. Synaptic dysfunction in Alzheimer's disease: the effects of amyloid beta on synaptic vesicle dynamics as a novel target for therapeutic intervention. *Neural regeneration research*. 2018;13(4):616-23.
48. Nunomura A, Castellani RJ, Zhu X, Moreira PI, Perry G, Smith MA. Involvement of oxidative stress in Alzheimer disease. *Journal of neuropathology and experimental neurology*. 2006;65(7):631-41.
49. Chen Z, Zhong C. Oxidative stress in Alzheimer's disease. *Neurosci Bull*. 2014;30(2):271-81.
50. Hensley K. Neuroinflammation in Alzheimer's disease: mechanisms, pathologic consequences, and potential for therapeutic manipulation. *Journal of Alzheimer's disease : JAD*. 2010;21(1):1-14.
51. Bagad DM, Chowdhury D, Khan Z. Towards understanding Alzheimer's Disease: An Overview. *Research Journal of Pharmaceutical, Biological and Chemical Sciences*. 2013;4:286-98.
52. Pini L, Pievani M, Bocchetta M, Altomare D, Bosco P, Cavado E, et al. Brain atrophy in Alzheimer's Disease and aging. *Ageing Research Reviews*. 2016;30:25-48.
53. Whitwell JL. Progression of Atrophy in Alzheimer's Disease and Related Disorders. *Neurotoxicity Research*. 2010;18(3):339-46.
54. Henneman WJP, Sluimer JD, Barnes J, van der Flier WM, Sluimer IC, Fox NC, et al. Hippocampal atrophy rates in Alzheimer disease: added value over whole brain volume measures. *Neurology*. 2009;72(11):999-1007.
55. Arendt T, Brückner MK, Morawski M, Jäger C, Gertz H-J. Early neurone loss in Alzheimer's disease: cortical or subcortical? *Acta neuropathologica communications*. 2015;3:10-.

56. Kordower JH, Chu Y, Stebbins GT, DeKosky ST, Cochran EJ, Bennett D, et al. Loss and atrophy of layer II entorhinal cortex neurons in elderly people with mild cognitive impairment. *Annals of neurology*. 2001;49(2):202-13.
57. Gomez-Isla T, Price JL, McKeel DW, Jr., Morris JC, Growdon JH, Hyman BT. Profound loss of layer II entorhinal cortex neurons occurs in very mild Alzheimer's disease. *The Journal of neuroscience : the official journal of the Society for Neuroscience*. 1996;16(14):4491-500.
58. Haass C, Kaether C, Thinakaran G, Sisodia S. Trafficking and proteolytic processing of APP. *Cold Spring Harbor Perspectives in Medicine*. 2012;2(5):a006270.
59. O'Brien RJ, Wong PC. Amyloid precursor protein processing and Alzheimer's disease. *Annual review of neuroscience*. 2011;34:185-204.
60. Nunan J, Small DH. Regulation of APP cleavage by alpha-, beta- and gamma-secretases. *FEBS letters*. 2000;483(1):6-10.
61. Morgado I, Fändrich M. Assembly of Alzheimer's A $\beta$  peptide into nanostructured amyloid fibrils. *Current Opinion in Colloid & Interface Science*. 2011;16(6):508-14.
62. Jarrett JT, Berger EP, Lansbury PT, Jr. The carboxy terminus of the beta amyloid protein is critical for the seeding of amyloid formation: implications for the pathogenesis of Alzheimer's disease. *Biochemistry*. 1993;32(18):4693-7.
63. Chromy BA, Nowak RJ, Lambert MP, Viola KL, Chang L, Velasco PT, et al. Self-Assembly of A $\beta$ 1-42 into Globular Neurotoxins. *Biochemistry*. 2003;42(44):12749-60.
64. Lambert MP, Barlow AK, Chromy BA, Edwards C, Freed R, Liosatos M, et al. Diffusible, nonfibrillar ligands derived from Abeta1-42 are potent central nervous system neurotoxins. *Proceedings of the National Academy of Sciences of the United States of America*. 1998;95(11):6448-53.
65. Hampel H, Shen Y, Walsh DM, Aisen P, Shaw LM, Zetterberg H, et al. Biological markers of amyloid  $\beta$ -related mechanisms in Alzheimer's disease. *Experimental neurology*. 2010;223(2):334-46.
66. Rak M, Del Bigio MR, Mai S, Westaway D, Gough K. Dense-core and diffuse Abeta plaques in TgCRND8 mice studied with synchrotron FTIR microspectroscopy. *Biopolymers*. 2007;87(4):207-17.
67. Selkoe DJ. Alzheimer's Disease: Genes, Proteins, and Therapy. *Physiological reviews*. 2001;81(2):741-66.
68. Chen G-f, Xu T-h, Yan Y, Zhou Y-r, Jiang Y, Melcher K, et al. Amyloid beta: structure, biology and structure-based therapeutic development. *Acta Pharmacologica Sinica*. 2017;38(9):1205-35.
69. Selkoe DJ, Hardy J. The amyloid hypothesis of Alzheimer's disease at 25 years. *EMBO molecular medicine*. 2016;8(6):595-608.
70. Hardy J, Selkoe DJ. The amyloid hypothesis of Alzheimer's disease: progress and problems on the road to therapeutics. *Science (New York, NY)*. 2002;297(5580):353-6.
71. Hardy J, Allsop D. Amyloid deposition as the central event in the aetiology of Alzheimer's disease. *Trends Pharmacol Sci*. 1991;12(10):383-8.
72. Citron M, Westaway D, Xia W, Carlson G, Diehl T, Levesque G, et al. Mutant presenilins of Alzheimer's disease increase production of 42-residue amyloid  $\beta$ -protein in both transfected cells and transgenic mice. *Nature Medicine*. 1997;3(1):67-72.
73. Kelleher RJ, 3rd, Shen J. Presenilin-1 mutations and Alzheimer's disease. *Proceedings of the National Academy of Sciences of the United States of America*. 2017;114(4):629-31.

74. McLean CA, Cherny RA, Fraser FW, Fuller SJ, Smith MJ, Konrad V, et al. Soluble pool of A $\beta$  amyloid as a determinant of severity of neurodegeneration in Alzheimer's disease. *Annals of neurology*. 1999;46(6):860-6.
75. Näslund J, Haroutunian V, Mohs R, Davis KL, Davies P, Greengard P, et al. Correlation between elevated levels of amyloid beta-peptide in the brain and cognitive decline. *Jama*. 2000;283(12):1571-7.
76. Gouras GK, Tsai J, Naslund J, Vincent B, Edgar M, Checler F, et al. Intraneuronal Abeta42 accumulation in human brain. *Am J Pathol*. 2000;156(1):15-20.
77. Nelson PT, Alafuzoff I, Bigio EH, Bouras C, Braak H, Cairns NJ, et al. Correlation of Alzheimer Disease Neuropathologic Changes With Cognitive Status: A Review of the Literature. *Journal of neuropathology and experimental neurology*. 2012;71(5):362-81.
78. Weingarten MD, Lockwood AH, Hwo SY, Kirschner MW. A protein factor essential for microtubule assembly. *Proceedings of the National Academy of Sciences of the United States of America*. 1975;72(5):1858-62.
79. Castellani RJ, Perry G. Tau Biology, Tauopathy, Traumatic Brain Injury, and Diagnostic Challenges. *Journal of Alzheimer's disease : JAD*. 2019;67(2):447-67.
80. Orr ME, Sullivan AC, Frost B. A Brief Overview of Tauopathy: Causes, Consequences, and Therapeutic Strategies. *Trends Pharmacol Sci*. 2017;38(7):637-48.
81. Mandelkow E-M, Mandelkow E. Biochemistry and Cell Biology of Tau Protein in Neurofibrillary Degeneration. *Cold Spring Harbor Perspectives in Medicine*. 2012;2(7):a006247.
82. Stoothoff WH, Johnson GV. Tau phosphorylation: physiological and pathological consequences. *Biochimica et biophysica acta*. 2005;1739(2-3):280-97.
83. Guo T, Noble W, Hanger DP. Roles of tau protein in health and disease. *Acta neuropathologica*. 2017;133(5):665-704.
84. Chen J, Kanai Y, Cowan NJ, Hirokawa N. Projection domains of MAP2 and tau determine spacings between microtubules in dendrites and axons. *Nature*. 1992;360(6405):674-7.
85. Simic G, Babic Leko M, Wray S, Harrington C, Delalle I, Jovanov-Milosevic N, et al. Tau Protein Hyperphosphorylation and Aggregation in Alzheimer's Disease and Other Tauopathies, and Possible Neuroprotective Strategies. *Biomolecules*. 2016;6(1):6.
86. Park SA, Ahn SI, Gallo J-M. Tau mis-splicing in the pathogenesis of neurodegenerative disorders. *BMB Rep*. 2016;49(8):405-13.
87. Liu C, Götz J. Profiling murine tau with 0N, 1N and 2N isoform-specific antibodies in brain and peripheral organs reveals distinct subcellular localization, with the 1N isoform being enriched in the nucleus. *PLoS One*. 2013;8(12):e84849.
88. Janke C, Beck M, Stahl T, Holzer M, Brauer K, Bigl V, et al. Phylogenetic diversity of the expression of the microtubule-associated protein tau: implications for neurodegenerative disorders. *Brain Res Mol Brain Res*. 1999;68(1-2):119-28.
89. Kampers T, Pangalos M, Geerts H, Wiech H, Mandelkow E. Assembly of paired helical filaments from mouse tau: implications for the neurofibrillary pathology in transgenic mouse models for Alzheimer's disease. *FEBS letters*. 1999;451(1):39-44.
90. Takuma H, Arawaka S, Mori H. Isoforms changes of tau protein during development in various species. *Developmental Brain Research*. 2003;142(2):121-7.
91. Hanes J, Zilka N, Bartkova M, Caletkova M, Dobrota D, Novak M. Rat tau proteome consists of six tau isoforms: implication for animal models of human tauopathies. *Journal of neurochemistry*. 2009;108(5):1167-76.

92. Gong CX, Iqbal K. Hyperphosphorylation of microtubule-associated protein tau: a promising therapeutic target for Alzheimer disease. *Current medicinal chemistry*. 2008;15(23):2321-8.
93. Hanger DP, Byers HL, Wray S, Leung KY, Saxton MJ, Seereeram A, et al. Novel phosphorylation sites in tau from Alzheimer brain support a role for casein kinase 1 in disease pathogenesis. *The Journal of biological chemistry*. 2007;282(32):23645-54.
94. Hanger DP, Anderton BH, Noble W. Tau phosphorylation: the therapeutic challenge for neurodegenerative disease. *Trends in Molecular Medicine*. 2009;15(3):112-9.
95. Alonso AC, Zaidi T, Grundke-Iqbal I, Iqbal K. Role of abnormally phosphorylated tau in the breakdown of microtubules in Alzheimer disease. *Proceedings of the National Academy of Sciences of the United States of America*. 1994;91(12):5562-6.
96. Kneynsberg A, Combs B, Christensen K, Morfini G, Kanaan NM. Axonal Degeneration in Tauopathies: Disease Relevance and Underlying Mechanisms. *Frontiers in neuroscience*. 2017;11:572-.
97. Krestova M, Garcia-Sierra F, Bartos A, Ricny J, Ripova D. Structure and Pathology of Tau Protein in Alzheimer Disease 2012. 731526 p.
98. Wang JZ, Xia YY, Grundke-Iqbal I, Iqbal K. Abnormal hyperphosphorylation of tau: sites, regulation, and molecular mechanism of neurofibrillary degeneration. *Journal of Alzheimer's disease : JAD*. 2013;33 Suppl 1:S123-39.
99. Wiśniewski HM, Narang HK, Terry RD. Neurofibrillary tangles of paired helical filaments. *Journal of the Neurological Sciences*. 1976;27(2):173-81.
100. Crowther RA. Straight and paired helical filaments in Alzheimer disease have a common structural unit. *Proceedings of the National Academy of Sciences of the United States of America*. 1991;88(6):2288-92.
101. Mandelkow E, von Bergen M, Biernat J, Mandelkow EM. Structural principles of tau and the paired helical filaments of Alzheimer's disease. *Brain Pathol*. 2007;17(1):83-90.
102. Mokhtar S, Bakhuraysah M, Cram D, Petratos S. The Beta-Amyloid Protein of Alzheimer's Disease: Communication Breakdown by Modifying the Neuronal Cytoskeleton. *International journal of Alzheimer's disease*. 2013;2013:910502.
103. Cras P, Kawai M, Siedlak S, Perry G. Microglia are associated with the extracellular neurofibrillary tangles of Alzheimer disease. *Brain research*. 1991;558(2):312-4.
104. Maphis N, Xu G, Kokiko-Cochran ON, Jiang S, Cardona A, Ransohoff RM, et al. Reactive microglia drive tau pathology and contribute to the spreading of pathological tau in the brain. *Brain*. 2015;138(6):1738-55.
105. Sheffield LG, Marquis JG, Berman NE. Regional distribution of cortical microglia parallels that of neurofibrillary tangles in Alzheimer's disease. *Neuroscience letters*. 2000;285(3):165-8.
106. Radde R, Bolmont T, Kaeser SA, Coomaraswamy J, Lindau D, Stoltze L, et al. Abeta42-driven cerebral amyloidosis in transgenic mice reveals early and robust pathology. *EMBO reports*. 2006;7(9):940-6.
107. Kurihara M, Mano T, Saito Y, Murayama S, Toda T, Iwata A. Colocalization of BRCA1 with Tau Aggregates in Human Tauopathies. *Brain Sci*. 2019;10(1).
108. Arriagada PV, Growdon JH, Hedley-Whyte ET, Hyman BT. Neurofibrillary tangles but not senile plaques parallel duration and severity of Alzheimer's disease. *Neurology*. 1992;42(3 Pt 1):631-9.
109. Bierer LM, Hof PR, Purohit DP, Carlin L, Schmeidler J, Davis KL, et al. Neocortical neurofibrillary tangles correlate with dementia severity in Alzheimer's disease. *Arch Neurol*. 1995;52(1):81-8.

110. Braak H, Braak E. Neuropathological staging of Alzheimer-related changes. *Acta neuropathologica*. 1991;82(4):239-59.
111. Braak H, Braak E. Staging of Alzheimer's disease-related neurofibrillary changes. *Neurobiology of aging*. 1995;16(3):271-8; discussion 8-84.
112. Van Hoesen GW, Augustinack JC, Dierking J, Redman SJ, Thangavel R. The Parahippocampal Gyrus in Alzheimer's Disease: Clinical and Preclinical Neuroanatomical Correlates. *Annals of the New York Academy of Sciences*. 2000;911(1):254-74.
113. Taylor KI, Probst A. Anatomic localization of the transentorhinal region of the perirhinal cortex. *Neurobiology of aging*. 2008;29(10):1591-6.
114. Witter MP, Kleven H, Kobro Flatmoen A. Comparative Contemplations on the Hippocampus. *Brain Behav Evol*. 2017;90(1):15-24.
115. Gertz HJ, Xuereb J, Huppert F, Brayne C, McGee MA, Paykel E, et al. Examination of the validity of the hierarchical model of neuropathological staging in normal aging and Alzheimer's disease. *Acta neuropathologica*. 1998;95(2):154-8.
116. Braak H, Alafuzoff I, Arzberger T, Kretzschmar H, Del Tredici K. Staging of Alzheimer disease-associated neurofibrillary pathology using paraffin sections and immunocytochemistry. *Acta neuropathologica*. 2006;112(4):389-404.
117. Martin L, Latypova X, Wilson CM, Magnaudeix A, Perrin M-L, Yardin C, et al. Tau protein kinases: Involvement in Alzheimer's disease. *Ageing Research Reviews*. 2013;12(1):289-309.
118. Woodgett JR. Molecular cloning and expression of glycogen synthase kinase-3/factor A. *The EMBO journal*. 1990;9(8):2431-8.
119. Shaw PC, Davies AF, Lau KF, Garcia-Barcelo M, Waye MM, Lovestone S, et al. Isolation and chromosomal mapping of human glycogen synthase kinase-3 alpha and -3 beta encoding genes. *Genome*. 1998;41(5):720-7.
120. Krishnankutty A, Kimura T, Saito T, Aoyagi K, Asada A, Takahashi S-I, et al. In vivo regulation of glycogen synthase kinase 3 $\beta$  activity in neurons and brains. *Scientific Reports*. 2017;7(1):8602.
121. Ishiguro K, Shiratsuchi A, Sato S, Omori A, Arioka M, Kobayashi S, et al. Glycogen synthase kinase 3 beta is identical to tau protein kinase I generating several epitopes of paired helical filaments. *FEBS letters*. 1993;325(3):167-72.
122. Ishiguro K, Omori A, Takamatsu M, Sato K, Arioka M, Uchida T, et al. Phosphorylation sites on tau by tau protein kinase I, a bovine derived kinase generating an epitope of paired helical filaments. *Neuroscience letters*. 1992;148(1):202-6.
123. Jope RS, Johnson GVW. The glamour and gloom of glycogen synthase kinase-3. *Trends in Biochemical Sciences*. 2004;29(2):95-102.
124. Reynolds CH, Betts JC, Blackstock WP, Nebreda AR, Anderton BH. Phosphorylation Sites on Tau Identified by Nanoelectrospray Mass Spectrometry. *Journal of neurochemistry*. 2000;74(4):1587-95.
125. Liu F, Liang Z, Shi J, Yin D, El-Akkad E, Grundke-Iqbal I, et al. PKA modulates GSK-3 $\beta$ - and cdk5-catalyzed phosphorylation of tau in site- and kinase-specific manners. *FEBS letters*. 2006;580(26):6269-74.
126. Wang J-z, Wu Q, Smith A, Grundke-Iqbal I, Iqbal K.  $\tau$  is phosphorylated by GSK-3 at several sites found in Alzheimer disease and its biological activity markedly inhibited only after it is prephosphorylated by A-kinase. *FEBS letters*. 1998;436(1):28-34.
127. Li T, Paudel HK. Glycogen Synthase Kinase 3 $\beta$  Phosphorylates Alzheimer's Disease-Specific Ser396 of Microtubule-Associated Protein Tau by a Sequential Mechanism. *Biochemistry*. 2006;45(10):3125-33.

128. Sengupta A, Wu Q, Grundke-Iqbal I, Iqbal K, Singh TJ. Potentiation of GSK-3-catalyzed Alzheimer-like phosphorylation of human tau by cdk5. *Mol Cell Biochem.* 1997;167(1-2):99-105.
129. Hatten ME. New Directions in Neuronal Migration. *Science (New York, NY).* 2002;297(5587):1660.
130. Doehner J, Knuesel I. Reelin-mediated Signaling during Normal and Pathological Forms of Aging. *Aging Dis.* 2010;1(1):12-29.
131. D'Arcangelo G, Curran T. Reeler: New tales on an old mutant mouse. *BioEssays.* 1998;20(3):235-44.
132. D'Arcangelo G, Miao GG, Chen SC, Soares HD, Morgan JI, Curran T. A protein related to extracellular matrix proteins deleted in the mouse mutant reeler. *Nature.* 1995;374(6524):719-23.
133. Pielecka-Fortuna J, Wagener R, Martens A-K, Goetze B, Schmidt K-F, Staiger J, et al. The disorganized visual cortex in reelin-deficient mice is functional and allows for enhanced plasticity. *Brain structure & function.* 2014;220.
134. Weeber EJ, Beffert U, Jones C, Christian JM, Forster E, Sweatt JD, et al. Reelin and ApoE receptors cooperate to enhance hippocampal synaptic plasticity and learning. *The Journal of biological chemistry.* 2002;277(42):39944-52.
135. Chen Y, Beffert U, Ertunc M, Tang TS, Kavalali ET, Bezprozvanny I, et al. Reelin modulates NMDA receptor activity in cortical neurons. *The Journal of neuroscience : the official journal of the Society for Neuroscience.* 2005;25(36):8209-16.
136. Herz J, Chen Y. Reelin, lipoprotein receptors and synaptic plasticity. *Nature Reviews Neuroscience.* 2006;7(11):850-9.
137. Beffert U, Morfini G, Bock HH, Reyna H, Brady ST, Herz J. Reelin-mediated signaling locally regulates protein kinase B/Akt and glycogen synthase kinase 3beta. *The Journal of biological chemistry.* 2002;277(51):49958-64.
138. Kibro-Flatmoen A, Nagelhus A, Witter MP. Reelin-immunoreactive neurons in entorhinal cortex layer II selectively express intracellular amyloid in early Alzheimer's disease. *Neurobiology of disease.* 2016;93:172-83.
139. Chin J, Massaro CM, Palop JJ, Thwin MT, Yu GQ, Bien-Ly N, et al. Reelin depletion in the entorhinal cortex of human amyloid precursor protein transgenic mice and humans with Alzheimer's disease. *The Journal of neuroscience : the official journal of the Society for Neuroscience.* 2007;27(11):2727-33.
140. Stranahan AM, Haberman RP, Gallagher M. Cognitive decline is associated with reduced reelin expression in the entorhinal cortex of aged rats. *Cereb Cortex.* 2011;21(2):392-400.
141. Knuesel I, Nyffeler M, Mormède C, Muhia M, Meyer U, Pietropaolo S, et al. Age-related accumulation of Reelin in amyloid-like deposits. *Neurobiology of aging.* 2009;30(5):697-716.
142. Hiesberger T, Trommsdorff M, Howell BW, Goffinet A, Mumby MC, Cooper JA, et al. Direct binding of Reelin to VLDL receptor and ApoE receptor 2 induces tyrosine phosphorylation of disabled-1 and modulates tau phosphorylation. *Neuron.* 1999;24(2):481-9.
143. Ohkubo N, Lee YD, Morishima A, Terashima T, Kikkawa S, Tohyama M, et al. Apolipoprotein E and Reelin ligands modulate tau phosphorylation through an apolipoprotein E receptor/disabled-1/glycogen synthase kinase-3beta cascade. *FASEB journal : official publication of the Federation of American Societies for Experimental Biology.* 2003;17(2):295-7.
144. Deutsch SI, Rosse RB, Deutsch LH. Faulty regulation of tau phosphorylation by the reelin signal transduction pathway is a potential mechanism of pathogenesis and

- therapeutic target in Alzheimer's disease. *Eur Neuropsychopharmacol.* 2006;16(8):547-51.
145. Maia L, Kaeser S, Reichwald J, Hruscha M, Martus P, Staufenbiel M, et al. Changes in Amyloid- and Tau in the Cerebrospinal Fluid of Transgenic Mice Overexpressing Amyloid Precursor Protein. *Science translational medicine.* 2013;5:194re2.
  146. Oddo S, Caccamo A, Shepherd JD, Murphy MP, Golde TE, Kaye R, et al. Triple-transgenic model of Alzheimer's disease with plaques and tangles: intracellular Abeta and synaptic dysfunction. *Neuron.* 2003;39(3):409-21.
  147. Oddo S, Caccamo A, Kitazawa M, Tseng BP, LaFerla FM. Amyloid deposition precedes tangle formation in a triple transgenic model of Alzheimer's disease. *Neurobiology of aging.* 2003;24(8):1063-70.
  148. Billings LM, Oddo S, Green KN, McGaugh JL, LaFerla FM. Intraneuronal Abeta causes the onset of early Alzheimer's disease-related cognitive deficits in transgenic mice. *Neuron.* 2005;45(5):675-88.
  149. Leon WC, Canneva F, Partridge V, Allard S, Ferretti MT, DeWilde A, et al. A novel transgenic rat model with a full Alzheimer's-like amyloid pathology displays pre-plaque intracellular amyloid-beta-associated cognitive impairment. *Journal of Alzheimer's disease : JAD.* 2010;20(1):113-26.
  150. Do Carmo S, Cuello A. Modeling Alzheimer's disease in transgenic rats. *Molecular neurodegeneration.* 2013;8:37.
  151. Russel WMS, Burch RL. *The Principles of Humane Experimental Technique.* London, Methuen 1959.
  152. Gage GJ, Kipke DR, Shain W. Whole animal perfusion fixation for rodents. *Journal of visualized experiments : JoVE.* 2012(65):3564.
  153. Hu W, Wu F, Zhang Y, Gong C-X, Iqbal K, Liu F. Expression of Tau Pathology-Related Proteins in Different Brain Regions: A Molecular Basis of Tau Pathogenesis. *Frontiers in aging neuroscience.* 2017;9:311-.
  154. Kubo A, Misonou H, Matsuyama M, Nomori A, Wada-Kakuda S, Takashima A, et al. Distribution of endogenous normal tau in the mouse brain. *J Comp Neurol.* 2019;527(5):985-98.
  155. Yao H-B, Shaw P-C, Wong C-C, Wan DC-C. Expression of glycogen synthase kinase-3 isoforms in mouse tissues and their transcription in the brain. *Journal of Chemical Neuroanatomy.* 2002;23(4):291-7.
  156. Takahashi M, Tomizawa K, Kato R, Sato K, Uchida T, Fujita SC, et al. Localization and developmental changes of tau protein kinase I/glycogen synthase kinase-3 beta in rat brain. *Journal of neurochemistry.* 1994;63(1):245-55.
  157. Kwak SG, Kim JH. Central limit theorem: the cornerstone of modern statistics. *Korean J Anesthesiol.* 2017;70(2):144-56.
  158. Paxinos G, Watson C. *The Rat Brain in Stereotaxic Coordinates.* 6th Edition ed: London: Academic Press.; 2007.
  159. Paxinos G, Franklin K. *The Mouse Brain in Stereotaxic Coordinates.* London: Academic Press; 2019.
  160. Lein ES, Hawrylycz MJ, Ao N, Ayres M, Bensinger A, Bernard A, et al. Genome-wide atlas of gene expression in the adult mouse brain. *Nature.* 2007;445(7124):168-76.
  161. Canto CB, Wouterlood FG, Witter MP. What does the anatomical organization of the entorhinal cortex tell us? *Neural plasticity.* 2008;2008:381243.
  162. Cappaert NLM, Van Strien NM, P WM. Hippocampal Formation. In: Paxinos G, editor. *The Rat Nervous System.* 4th Volume ed. London: Academic Press; 2015. p. 511-73.

163. Ennis M, Puche AC, Holy T, Shipley MT. The Olfactory System. In: Paxinos G, editor. *The Rat Nervous System*. 4th Edition ed. London: Academic Press; 2015. p. 761-803.
164. Jolkkonen E, Miettinen R, Pitkanen A. Projections from the amygdalo-piriform transition area to the amygdaloid complex: a PHA-I study in rat. *J Comp Neurol*. 2001;432(4):440-65.
165. Wang J, Tanila H, Puoliväli J, Kadish I, van Groen T. Gender differences in the amount and deposition of amyloidbeta in APPswe and PS1 double transgenic mice. *Neurobiology of disease*. 2003;14(3):318-27.
166. Hooper C, Killick R, Lovestone S. The GSK3 hypothesis of Alzheimer's disease. *Journal of neurochemistry*. 2008;104(6):1433-9.
167. Ishizawa T, Sahara N, Ishiguro K, Kersh J, McGowan E, Lewis J, et al. Co-localization of glycogen synthase kinase-3 with neurofibrillary tangles and granulovacuolar degeneration in transgenic mice. *The American journal of pathology*. 2003;163(3):1057-67.
168. Pei JJ, Braak E, Braak H, Grundke-Iqbal I, Iqbal K, Winblad B, et al. Distribution of active glycogen synthase kinase 3beta (GSK-3beta) in brains staged for Alzheimer disease neurofibrillary changes. *Journal of neuropathology and experimental neurology*. 1999;58(9):1010-9.
169. Pedros I, Petrov D, Allgaier M, Sureda F, Barroso E, Beas-Zarate C, et al. Early alterations in energy metabolism in the hippocampus of APPswe/PS1dE9 mouse model of Alzheimer's disease. *Biochimica et biophysica acta*. 2014;1842(9):1556-66.
170. Wang Z, Xiong L, Wan W, Duan L, Bai X, Zu H. Intranasal BMP9 Ameliorates Alzheimer Disease-Like Pathology and Cognitive Deficits in APP/PS1 Transgenic Mice. *Frontiers in Molecular Neuroscience*. 2017;10(32).
171. Do Carmo S, Cuello AC. Modeling Alzheimer's disease in transgenic rats. *Molecular neurodegeneration*. 2013;8:37-.
172. Oddo S, Caccamo A, Shepherd JD, Murphy MP, Golde TE, Kaye R, et al. Triple-transgenic model of Alzheimer's disease with plaques and tangles: intracellular Abeta and synaptic dysfunction. *Neuron*. 2003;39(3):409-21.
173. Mastrangelo MA, Bowers WJ. Detailed immunohistochemical characterization of temporal and spatial progression of Alzheimer's disease-related pathologies in male triple-transgenic mice. *BMC Neurosci*. 2008;9:81-.
174. Fang H, Zhang L-F, Meng F-T, Du X, Zhou J-N. Acute hypoxia promote the phosphorylation of tau via ERK pathway. *Neuroscience letters*. 2010;474(3):173-7.
175. Raz L, Bhaskar K, Weaver J, Marini S, Zhang Q, Thompson JF, et al. Hypoxia promotes tau hyperphosphorylation with associated neuropathology in vascular dysfunction. *Neurobiology of disease*. 2019;126:124-36.
176. Planel E, Richter KE, Nolan CE, Finley JE, Liu L, Wen Y, et al. Anesthesia leads to tau hyperphosphorylation through inhibition of phosphatase activity by hypothermia. *The Journal of neuroscience : the official journal of the Society for Neuroscience*. 2007;27(12):3090-7.
177. McMillan P, Korvatska E, Poorkaj P, Evstafjeva Z, Robinson L, Greenup L, et al. Tau isoform regulation is region- and cell-specific in mouse brain. *J Comp Neurol*. 2008;511(6):788-803.
178. Hutton M, Lendon CL, Rizzu P, Baker M, Froelich S, Houlden H, et al. Association of missense and 5'-splice-site mutations in tau with the inherited dementia FTDP-17. *Nature*. 1998;393(6686):702-5.

## 6. Appendices

### Appendix 6.1 List of animals

#### 6.1.1 Animals used for antibody testing and Nissl staining.

Animal ID	Strain	Age	Sex
76073	Ck2/tTA+/- x APP/PS1+/-	1 month	Male
72451/72421	APP/PS1 (HM3-DDD+/-;Odz3-P8117+/- x APP/PS1+/- )	9 months	Male
72977	APP/PS1+/- x Odz3-P8117+/-;tetO-HM4+/-	8 months	Male
73331	APP/PS1+/- x Odz3-P8117+/-;tetO-HM4+/-	7 months	Male
72448	APP/PS1 ( HM3-DDD+/-;Odz3-P8117+/- x APP/PS1+/-)	9 months	Female
76339	Ck2/tTA+/- x APP/PS1+/-	2 months P59	Male
76340	Ck2/tTA+/- x APP/PS1+/-	2 months P59	Male
78782	Ck2/tTA+/- x APP/PS1+/-	P39	Male
78806	Ck2/tTA+/- x APP/PS1+/-	P36	Male
Unknown ID (M17)	APP/PS1+ KO for DNA repair gene Graciously donated to me by Katja Scheffler at Institute for Neuromedicine and Movement Science	17 months	Male
71758	APP/PS1 +/- X CK2/tTa +/-	5 months	Male
57986	C57	6 months	Female
57987	C57	6 months	Female
23506	Alzheimer's +/+	2.5 months	Female
22464	AD+/+	5 months	Male
19020	AD+/+	9 months	Female
17461	AD-/-	9 months	Male
14216	AD+/+	18 months	Female

80156	3xTg-AD <sup>+/+</sup> x 3xTg-AD <sup>+/+</sup>	8 months P249	Female
80158	3xTg-AD <sup>+/+</sup> x 3xTg-AD <sup>+/+</sup>	8 months P249	Female
80157	3xTg-AD <sup>+/+</sup> x 3xTg-AD <sup>+/+</sup>	8 months P249	Female

### 6.1.2 List of injected 3xTG mice excluded from final analysis

Animal ID	Strain	Age	Sex	Injection
77130	3xTG	3 months	F	right AAV/CMV/siRNA4/GFP, left: AAV/CMV/GFP. GOOD PERFUSION. Good GFP signal
77131	3xTG	3 months	F	right AAV/CMV/siRNA4/GFP, left: AAV/CMV/GFP. GOOD PERFUSION (some dura left)
77133	3xTG	3 months	M	right: AAV/CMV/GFP; left: AAV/CMV/siRNA4/GFP. Perfused because it was sick, GOOD PERFUSION

### 6.1.3 List of injected APP/PS1 mice excluded from final analysis

Animal ID	Strain	Age	Sex	Injection
76070	APP/PS1 +/-	6m	F	Injections: right AAV/CMV/shRNA/GFP, left: AAV/CMV/GFP GOOD PERFUSION. No GFP signal
76075	APP/PS1 +/- X CK2 +/-	6m	M	Injections: right AAV/TetO R3-R6 myc His(900nl!), left AAV/TetO GFP GOOD PERFUSION. No GFP signal
75282	APP/PS1 +/- X CK2 +/-	3m	F	Injections: right AAV/CMV/shRNA/GFP, left: AAV/CMV/GFP. GOOD PERFUSION

76072	APP/PS1 +/- X CK2 +/-	7m	M	Injections: right AAV/TetO R3-R6 myc His(900nl!), left AAV/TetO GFP GOOD PERFUSION
77016	APP/PS1 +/-	3m	F	Injections: right AAV/CMV/siRNA4/GFP, left: AAV/CMV/GFP GOOD PERFUSION
75824	APP/PS1 +/- X CK2 +/-	6m	M	Injections: right AAV/TetO R3-R6 myc His(900nl!), left AAV/TetO GFP. GOOD PERFUSION
75817	APP/PS1 +/- X CK2 +/-	6m	F	Injections: right AAV/TetO R3-R6 myc His(900nl!), left AAV/TetO GFP. GOOD PERFUSION
77017	APP/PS1 +/- X CK2 +/-	3m	M	Injections: right: AAV/CMV/GFP; left: AAV/CMV/siRNA4/GFP GOOD PERFUSION
76945	APP/PS1 +/- X CK2 +/-	3m	M	Injections: right AAV/CMV/siRNA4/GFP, left: AAV/CMV/GFP GOOD PERFUSION
75282	APP/PS1 +/- X CK2 +/-	3m	F	Injections: right AAV/CMV/shRNA/GFP, left: AAV/CMV/GFP. GOOD PERFUSION
71983	APP/PS1 +/- X CK2 +/-	5m	F	Injections: right AAV/TetO R3-R6 myc His, left AAV/TetO GFP
77024	APP/PS1 +/- X CK2 +/-	3m	F	Injections: right, AAV/TetO GFP, left, AAV/TetO R3-R6 myc His(1200nl!) GOOD PERFUSION. NB very little GFP signal
76938	APP/PS1 +/-	3m	F	Injections: right AAV/CMV/siRNA4/GFP, left: AAV/CMV/GFP OK PERFUSION. Smaller PFA response

#### 6.1.4 List of injected McGill-R-Thy1-APP rats excluded from analysis

Animal ID	Strain	Age	Sex	Injections
-----------	--------	-----	-----	------------

23914	McGill-R- Thy1-APP	4m	M	right: AAV/CMV/mRNA1/GFP, left: AAV/CMV/GFP
-------	-----------------------	----	---	--

## Appendix 6.2 Immunohistochemistry protocols

### 6.2.1 pSer396 tau and Reelin G10 double immunofluorescent protocol

Wash sections 3 x 2 minutes in PB

1. Heat induced antigen retrieval in PB 60 °C for 2 hours
2. Wash sections 3x 10 minutes in PBT
3. Incubate for 1 hour with 10% normal goat serum in PBT.
4. Incubate with primary antibody monoclonal rabbit anti **pS396-Tau (1:2000)** and monoclonal mouse anti-reelin **G10 (1:1000)** overnight on shaker at 4°C with PBT + **5% NGS**
5. Wash sections 3 x 5 minutes in PBT
6. Incubate with secondary antibody **goat anti-RABBIT Alexa 546 (1:1000)** and **Goat anti-MOUSE Alexa 635 (1:1000)** in PBT for 120 minutes on shaker in room temperature. + **5% NGS**
7. Wash sections 3 x 5 minutes in PB
8. Wash sections 2 x 5 minutes in Tris-HCl
9. Mount in Tris-HCl on Superfrost slides and dry overnight
10. Coverslip with Xylene and Entellan and dry overnight

### 6.2.2 GSK3β Tyr216 and Reelin G10 double immunofluorescent protocol.

Wash sections 3 x 2 minutes in PB

1. Heat induced antigen retrieval in PB 60 °C for 2 hours
2. Wash sections 3x 10 minutes in PBT
3. Incubate for 1 hour with 10% normal goat serum in PBT.
4. Incubate with primary antibody monoclonal **rabbit anti pGSK3β (1:1000)** and monoclonal **mouse anti-reelin G10 (1:1000)** overnight on shaker at 4°C with PBT + **5% NGS**
5. Wash sections 3 x 10 minutes in PBT
6. Incubate with secondary antibody **goat anti-RABBIT Alexa 546 (1:1000)** and **goat anti-MOUSE Alexa 635 (1:1000)** in PBT for 120 minutes on shaker in room temperature. + **5% NGS**

7. Wash sections 3 x 10 minutes in PB
8. Wash sections 2 x 5 minutes in Tris-HCl
9. Mount in Tris-HCl on Superfrost slides and dry overnight
10. Coverslip with Tolouene and Entellan and dry overnight

### 6.2.3 AT8 phospho tau protocol

Pre-treatment:

Wash sections 3x2 min in TBS

Heat induced antigen retrieval in TBS 60 °C for 2 hours

1. Wash sections 3 x 10 minutes in TBS
2. Quench endogenous peroxidases in 3% H<sub>2</sub>O<sub>2</sub> in TBS for 30 minutes
3. Wash sections 3x 10 minutes in TBS-Tx (SA 1: )
4. Incubate for 1 hour with 10% normal goat serum in TBS-Tx (SA2)
5. Incubate with primary antibody AT8 (1:1000) overnight on shaker at 4°C with TBS-TX. Select control sections (no PA). One triangular cut.
6. Wash sections 3 x 10 minutes in TBS-Tx
7. Incubate with secondary antibody, biotinylated goat anti-mouse (1:1000) in TBS-Tx for 90 minutes on shaker in room temperature Select control sections (No PA/SA). Two triangular cuts.
8. Wash sections 3 x 10 minutes in TBS-Tx
9. Incubate with ABC for 90 minutes at room temperature
10. Wash sections 3 x 10 minutes in TBS-Tx
11. Rinse sections 2 x 5 minutes in Tris-HCl
12. Incubate with DAB for 10 minutes
13. Wash sections 2 x 5 minutes in Tris-HCl
14. Mount in Tris-HCl on Superfrost slides and dry overnight
15. Coverslip with Xylene and Entellan and dry overnight

Make ABC one hour before use

Make DAB two hours before use

#### 6.2.4 AT8 protocol with pre-incubation of SA

Pre-treatment:

Wash sections 3x2 min in TBS

Heat induced antigen retrieval in TBS 60 °C for 2 hours

1. Wash sections 3 x 10 minutes in TBS
2. Quench endogenous peroxidases in 3% H<sub>2</sub>O<sub>2</sub> in TBS for 30 minutes
3. Wash sections 3x 10 minutes in TBS-Tx
4. Incubate for 1 hour with 10% normal goat serum in TBS-Tx
5. Incubate with primary antibody AT8 (1:1000) overnight on shaker at 4°C with TBS-TX +5% NGS. Select control sections (no PA). One triangular cut.
  - a. Pre-incubate biotinylated goat anti-mouse overnight. 1:500
6. Wash sections 3 x 10 minutes in TBS-Tx
7. Incubate with secondary antibody, biotinylated goat anti-mouse (1:500) in TBS-Tx + 5%NGS for 90 minutes on shaker in room temperature Select control sections (No PA/SA, SA only two triangular cuts).
8. Wash sections 3 x 10 minutes in TBS-Tx
9. Incubate with ABC for 90 minutes at room temperature
10. Wash sections 3 x 10 minutes in TBS-Tx
11. Rinse sections 2 x 5 minutes in Tris-HCl
12. Incubate with DAB for 10 minutes
13. Wash sections 2 x 5 minutes in Tris-HCl
14. Mount in Tris-HCl on Superfrost slides and dry overnight
15. Coverslip with Xylene and Entellan and dry overnight

Make ABC one hour before use

Make DAB two hours before use

#### 6.2.5 AT8 protocol with Tween-20

Four groups with different incubations with tween-20:

- 1) Tween-20 in: NGS, PA, SA
- 2) Tween-20 in: NGS
- 3) Tween-20 in: PA
- 4) Tween-20 in: SA

Pre-treatment:

Wash sections 3x2 min in TBS

Heat induced antigen retrieval in TBS 60 °C for 2 hours

- 1) Wash sections 3 x 10 minutes in TBS
- 2) Quench endogenous peroxidases in 3% H<sub>2</sub>O<sub>2</sub> in TBS for 30 minutes
- 3) Wash sections 3x 10 minutes in TBS-Tx
- 4) Incubate for 1 hour with 10% normal goat serum in TBS-Tx (Group 1 and 2)
- 5) Incubate with primary antibody AT8 (1:1000) overnight on shaker at 4°C with TBS-TX +5% NGS. Select control sections (no PA). One triangular cut. (Group 1 and 3)
- 6) Pre-incubate biotinylated goat anti-mouse overnight. 1:500
- 7) Wash sections 3 x 10 minutes in TBS-Tx
- 8) Incubate with secondary antibody, biotinylated goat anti-mouse (1:500) in TBS-Tx + 5%NGS for 90 minutes on shaker in room temperature Select control sections (No PA/SA, SA only two triangular cuts). (Group 1 and 4)
- 9) Wash sections 3 x 10 minutes in TBS-Tx
- 10) Incubate with ABC for 90 minutes at room temperature
- 11) Wash sections 3 x 10 minutes in TBS-Tx
- 12) Rinse sections 2 x 5 minutes in Tris-HCl
- 13) Incubate with DAB for 10 minutes
- 14) Wash sections 2 x 5 minutes in Tris-HCl
- 15) Mount in Tris-HCl on Superfrost slides and dry overnight
- 16) Coverslip with Xylene and Entellan and dry overnight

Make ABC one hour before use

Make DAB two hours before use

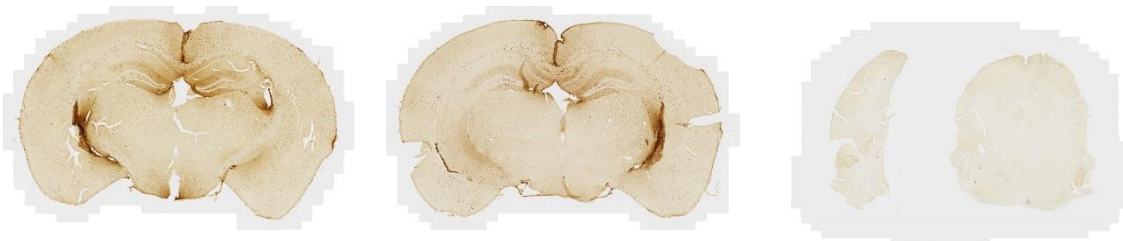


**Figure 31.** Mouse 7331 incubated with Tween-20 in NGS, PA and SA. Left: PA/SA, Middle: PA omitted, Right; no PA/SA

### 6.2.6 AT8 protocol with Goat SA/Donkey SA

8 sections from each mouse (71758/72448)

4 sections incubated with Goat SA (1:1000/1:4000)

4 sections incubated with Donkey SA (1:1000/1:4000)

- 1) Wash sections 3 x 10 minutes in TBS
- 2) Quench endogenous peroxidases in 3% H<sub>2</sub>O<sub>2</sub> in TBS for 30 minutes
- 3) Wash sections 3x 10 minutes in TBS-Tx
- 4) Incubate for 1 hour with 10% normal goat serum in TBS-Tx
- 5) Incubate with primary antibody AT8 (1:1000) overnight on shaker at 4°C with TBS-TX +5% NGS. Select control sections (no PA). One triangular cut.
- 6) Pre-incubate biotinylated goat anti-mouse overnight. 1:500
- 7) Wash sections 3 x 10 minutes in TBS-Tx
- 8) Incubate with secondary antibody, biotinylated goat anti-mouse (1:1000/1:4000) And biotinylated Donkey anti mouse (1:1000/1:4000) in TBS-Tx + 5%NGS for 90 minutes on shaker in room temperature Select control sections (No PA/SA, SA only two triangular cuts).
- 9) Wash sections 3 x 10 minutes in TBS-Tx
- 10) Incubate with ABC for 90 minutes at room temperature
- 11) Wash sections 3 x 10 minutes in TBS-Tx
- 12) Rinse sections 2 x 5 minutes in Tris-HCl
- 13) Incubate with DAB for 10 minutes
- 14) Wash sections 2 x 5 minutes in Tris-HCl
- 15) Mount in Tris-HCl on Superfrost slides and dry overnight
- 16) Coverslip with Xylene and Entellan and dry overnight

Make ABC one hour before use

Make DAB two hours before use

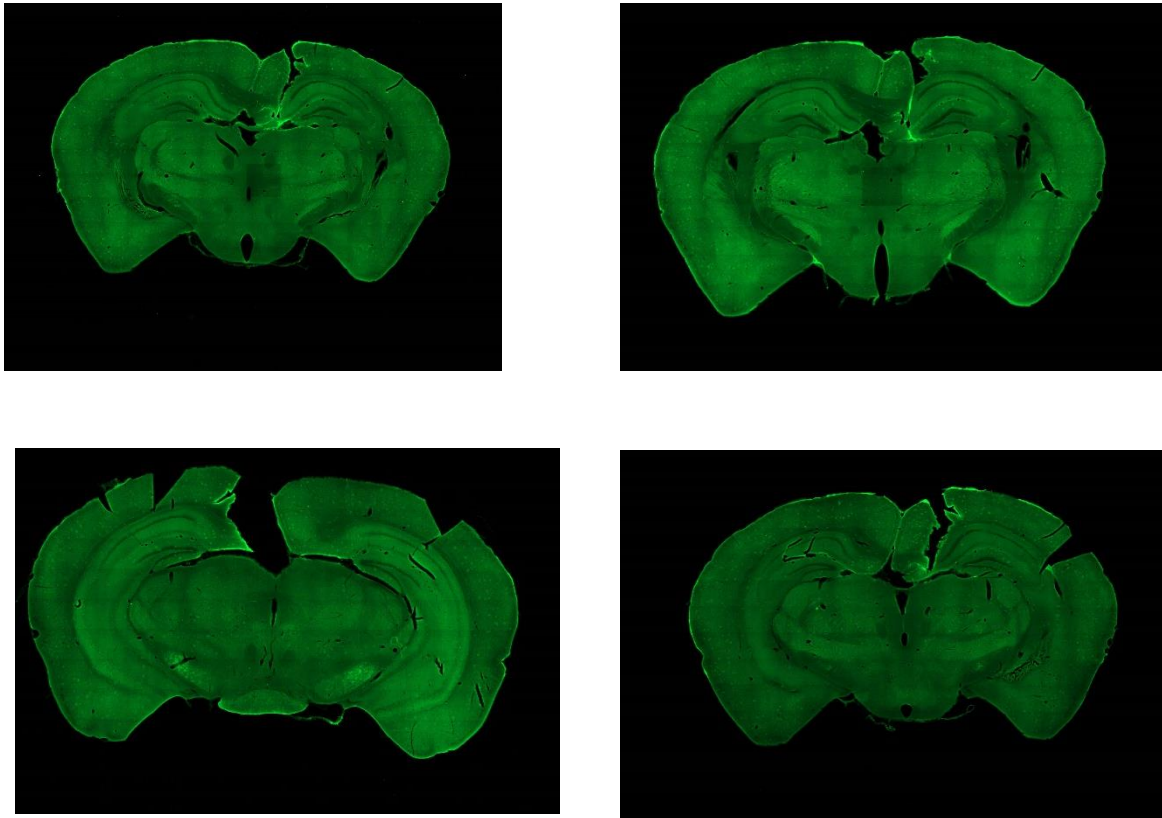


*Figure 32 Comparison of background reactivity in Goat anti mouse- and Donkey anti mouse SA. 9 month old APP/PS1 (HM3-DDD+/-;Odz3-P8117+/- x APP/PS1+/- (72421). Top left: Donkey (1:1000), top right: Donkey (1:4000), bottom right: Goat (1:1000), bottom left: goat (1:4000).*

### Appendix 6.3 List of secondary antibodies

<b>Secondary antibody</b>	<b>Supplier</b>	<b>Reference</b>
Goat anti-Mouse A488	Thermo Fisher	A11003
Goat anti-Mouse A546	Thermo Fisher	A31574
Goat anti-Mouse A635	Thermo Fisher	A11001
Donkey anti-mouse A488	Invitrogen	A-21202
Donkey anti-mouse A546	Invitrogen	
Goat anti-rabbit A488	Invitrogen	A11008

Goat anti-rabbit A546	Invitrogen	A11010
Goat anti-Mouse IgG biotin	Sigma	B7151
Goat anti-rabbit IgG biotin	Sigma	B8895

## **Appendix 6.4 Chemical solutions**

### **Ringer Solution, pH 6.9**

0.85% NaCl 4.25 g / 500 mL H<sub>2</sub>O

0.025% KCl 0.125 g / 500 mL H<sub>2</sub>O

0.02% NaHCO<sub>3</sub> 0.1 g / 500 mL H<sub>2</sub>O

Mix the salts with the water in a container with magnet on a stirrer until dissolved. Filtrate solution and heat to about 40 °C before use. Set the pH to 6,9 using O<sub>2</sub>. Ringer should be made fresh before every perfusion.

### **Phosphate buffer (PB) 0.4M, pH 7.4**

A: NaH<sub>2</sub>PO<sub>4</sub>H<sub>2</sub>O 27.6 g/500 mL H<sub>2</sub>O

B: Na<sub>2</sub>HPO<sub>4</sub>H<sub>2</sub>O 35.6 g/500 mL H<sub>2</sub>O

Make solutions A and B (start with B, it needs longer time). Add solution A to solution B until the pH is 7,4 ( = 0.4M ). Store in a dark place at room temperature for up to one month.

#### **Phosphate buffer (PB) 0.125M, pH 7.4**

Dilute 0.4M phosphate buffer. Can be stored in refrigerator for up to 1 week.

100 mL: 31.25 mL 0.4M phosphate buffer + 68.75 mL H<sub>2</sub>O

500 mL: 156 mL 0.4M phosphate buffer + 344 mL H<sub>2</sub>O

#### **10% paraformaldehyde (PFA)**

200mL H<sub>2</sub>O

20g PFA

A few drops sodium hydroxide (NaOH)

Warm the water in a microwave oven to 60°C. Measure the PFA and add it to the water. Let it stir on a heating stirrer and add the NaOH. The solution is ready when it becomes clear.

Everything should be carefully carried out in a ventilated hood.

#### **Fixative 4% paraformaldehyde (PFA) 500 ml**

200mL 10% paraformaldehyde (described above)

156 mL 0.4 M phosphate buffer

144 mL H<sub>2</sub>O

Start by adding water and PB to the 10% paraformaldehyde solution. Use HCl to adjust the pH to 7.4 and filtrate before use. Everything should be carefully carried out in a ventilated hood. Make new fixative for every perfusion.

68

#### **Tris-HCl pH 7.6**

Tris 3.03 g/500 mL H<sub>2</sub>O

Use HCl to adjust the pH to 7.6. Store in refrigerator for up to one week.

#### **TBS buffer pH 8.0**

Tris 3.03 g/500 mL H<sub>2</sub>O

NaCl 4.48 g/500 mL H<sub>2</sub>O

Mix the measured water, Tris and NaCl before adjusting the pH to 8.0 with HCl. The solution can be stored in refrigerator for up to one week.

#### **0.2% TBS-TX buffer pH 8,0**

Tris 3.03 g/500 ml H<sub>2</sub>O

NaCl 4.48 g/500 ml H<sub>2</sub>O

Triton-X-100 1 mL/500 ml H<sub>2</sub>O

Mix the measured water, Tris, NaCl and Triton-X-100. Adjust pH to 8.0 by using HCl. Store in refrigerator for up to one week.

#### **Sucrose**

Dissolve 30 g sucrose in 31.25 ml 0.4M PB and 68.75 mL H<sub>2</sub>O (or in 100 mL 0.125M PB).

#### **Cryoprotective solution (DMSO)**

31,25 ml 0,4 M phosphate buffer

46,75 ml H<sub>2</sub>O

20 ml glycerine

2 ml DMSO

Mixing should be carefully carried out in a ventilated hood.

## Appendix 6.5 SPSS output from statistical analyses

### 6.5.1 APP/PS1 76502

pTau

#### Mann-Whitney Test

Ranks				
	Hemisphere	N	Mean Rank	Sum of Ranks
pTau	pTau control	20	13,35	267,00
	pTau miRNA	22	28,91	636,00
Total		42		

#### Test Statistics<sup>a</sup>

pTau	
Mann-Whitney U	57,000
Wilcoxon W	267,000
Z	-4,105
Asymp. Sig. (2-tailed)	,000

a. Grouping Variable:  
Hemisphere

#### Mann-Whitney Test

Ranks				
	Hemisphere	N	Mean Rank	Sum of Ranks
Reelin	pTau control	20	32,25	645,00
	pTau miRNA	22	11,73	258,00
Total		42		

#### Test Statistics<sup>a</sup>

Reelin	
Mann-Whitney U	5,000
Wilcoxon W	258,000
Z	-5,415
Asymp. Sig. (2-tailed)	,000

a. Grouping Variable:  
Hemisphere

$$r = 4,105 / \sqrt{42} = 0,633$$

$$r = 5,415 / \sqrt{42} = 0,835$$

### GSK3B

#### Mann-Whitney Test

Ranks				
	Hemisphere_2	N	Mean Rank	Sum of Ranks
GSK3B	,00	23	13,22	304,00
	1,00	39	42,28	1649,00
Total		62		

#### Test Statistics<sup>a</sup>

GSK3B	
Mann-Whitney U	28,000
Wilcoxon W	304,000
Z	-6,128
Asymp. Sig. (2-tailed)	,000

a. Grouping Variable:  
Hemisphere\_2

#### Mann-Whitney Test

Ranks				
	Hemisphere_2	N	Mean Rank	Sum of Ranks
Reelin_2	,00	23	51,00	1173,00
	1,00	39	20,00	780,00
Total		62		

#### Test Statistics<sup>a</sup>

Reelin_2	
Mann-Whitney U	,000
Wilcoxon W	780,000
Z	-6,536
Asymp. Sig. (2-tailed)	,000

a. Grouping Variable:  
Hemisphere\_2

$$r = 6,128 / \sqrt{62} = 0,778$$

$$r = 6,536 / \sqrt{62} = 0,83$$

## 6.5.2 APP/PS1 75284

**Group Statistics**

	Hemisphere	N	Mean	Std. Deviation	Std. Error Mean
pTau	pTau control	45	,4824	,28365	,04228
	pTau miRNA	43	,3072	,22298	,03400

**Independent Samples Test**

		Levene's Test for Equality of Variances		t-test for Equality of Means					95% Confidence Interval of the Difference	
		F	Sig.	t	df	Sig. (2-tailed)	Mean Difference	Std. Error Difference	Lower	Upper
pTau	Equal variances assumed	3,819	,054	3,211	86	,002	,17519	,05456	,06674	,28365
	Equal variances not assumed			3,229	82,962	,002	,17519	,05426	,06727	,28311

$$d = 2 \times 3,211 / \sqrt{86} = 0.692$$

**Group Statistics**

	Hemisphere	N	Mean	Std. Deviation	Std. Error Mean
Reelin	pTau control	45	,5755	,22083	,03292
	pTau miRNA	43	,2085	,07382	,01126

**Independent Samples Test**

		Levene's Test for Equality of Variances		t-test for Equality of Means					95% Confidence Interval of the Difference	
		F	Sig.	t	df	Sig. (2-tailed)	Mean Difference	Std. Error Difference	Lower	Upper
Reelin	Equal variances assumed	29,095	,000	10,355	86	,000	,36693	,03544	,29649	,43738
	Equal variances not assumed			10,547	54,116	,000	,36693	,03479	,29718	,43668

$$d = 2 \times 10,547 / \sqrt{54,1} = 2.867$$

**Group Statistics**

	Hemisphere_2	N	Mean	Std. Deviation	Std. Error Mean
GSK3B	,00	54	,5770	,20158	,02743
	1,00	48	,2845	,16574	,02392

**Independent Samples Test**

		Levene's Test for Equality of Variances		t-test for Equality of Means					95% Confidence Interval of the Difference	
		F	Sig.	t	df	Sig. (2-tailed)	Mean Difference	Std. Error Difference	Lower	Upper
GSK3B	Equal variances assumed	1,912	,170	7,944	100	,000	,29246	,03682	,21942	,36551
	Equal variances not assumed			8,035	99,424	,000	,29246	,03640	,22025	,36468

$$d = 2 \times 7,944 / \sqrt{100} = 1,588$$

**Group Statistics**

Hemisphere_2		N	Mean	Std. Deviation	Std. Error Mean
Reelin_2	,00	54	,5506	,19234	,02617
	1,00	48	,1465	,10098	,01458

**Independent Samples Test**

		Levene's Test for Equality of Variances		t-test for Equality of Means					95% Confidence Interval of the Difference	
		F	Sig.	t	df	Sig. (2-tailed)	Mean Difference	Std. Error Difference	Lower	Upper
Reelin_2	Equal variances assumed	24,065	,000	13,039	100	,000	,40403	,03099	,34255	,46551
	Equal variances not assumed			13,486	82,068	,000	,40403	,02996	,34443	,46363

$$d = 2 \times 13,486 / \sqrt{82,1} = 2.976$$

**6.5.3 3xTG 77132**

**Group Statistics**

Hemisphere		N	Mean	Std. Deviation	Std. Error Mean
pTau	Control	54	,3649	,28850	,03926
	miRNA	69	,2832	,15388	,01852

**Independent Samples Test**

		Levene's Test for Equality of Variances		t-test for Equality of Means					95% Confidence Interval of the Difference	
		F	Sig.	t	df	Sig. (2-tailed)	Mean Difference	Std. Error Difference	Lower	Upper
pTau	Equal variances assumed	37,707	,000	2,016	121	,046	,08169	,04053	,00145	,16193
	Equal variances not assumed			1,882	76,281	,064	,08169	,04341	-,00476	,16814

$$d = 2 \times 1,882 / \sqrt{76,281} = 0.430$$

**Group Statistics**

Hemisphere		N	Mean	Std. Deviation	Std. Error Mean
Reelin	Control	54	,3848	,27242	,03707
	miRNA	69	,0804	,05379	,00648

**Independent Samples Test**

		Levene's Test for Equality of Variances		t-test for Equality of Means					95% Confidence Interval of the Difference	
		F	Sig.	t	df	Sig. (2-tailed)	Mean Difference	Std. Error Difference	Lower	Upper
Reelin	Equal variances assumed	129,747	,000	9,068	121	,000	,30439	,03357	,23793	,37084
	Equal variances not assumed			8,088	56,242	,000	,30439	,03763	,22901	,37977

$$d = 2 \times 8,088 / \sqrt{56,2} = 2.157$$

Group Statistics					
	Hemisphere_2	N	Mean	Std. Deviation	Std. Error Mean
GSK3B	Control	100	,4961	,18949	,01895
	miRNA	107	,4674	,19267	,01863

Independent Samples Test										
		Levene's Test for Equality of Variances				t-test for Equality of Means				
		F	Sig.	t	df	Sig. (2-tailed)	Mean Difference	Std. Error Difference	95% Confidence Interval of the Difference	
									Lower	Upper
GSK3B	Equal variances assumed	,127	,722	1,079	205	,282	,02869	,02659	-,02373	,08110
	Equal variances not assumed			1,080	204,461	,282	,02869	,02657	-,02370	,08107

$$d = 2 \times 1.079 / \sqrt{205} = 0.150$$

Group Statistics					
	Hemisphere_2	N	Mean	Std. Deviation	Std. Error Mean
Reelin_2	Control	100	,3258	,22006	,02201
	miRNA	107	,1109	,07299	,00706

Independent Samples Test										
		Levene's Test for Equality of Variances				t-test for Equality of Means				
		F	Sig.	t	df	Sig. (2-tailed)	Mean Difference	Std. Error Difference	95% Confidence Interval of the Difference	
									Lower	Upper
Reelin_2	Equal variances assumed	119,225	,000	9,557	205	,000	,21492	,02249	,17058	,25926
	Equal variances not assumed			9,300	119,228	,000	,21492	,02311	,16916	,26068

$$d = 2 \times 9.300 / \sqrt{119.2} = 1.703$$

### 6.5.4 *Mcgill-R-Thy1-APP 25180*

0=control, 1=miRNA

Group Statistics					
	Hemisphere	N	Mean	Std. Deviation	Std. Error Mean
pTau	,00	259	,3835	,14662	,00911
	1,00	272	,1564	,07215	,00437

Independent Samples Test										
		Levene's Test for Equality of Variances				t-test for Equality of Means				
		F	Sig.	t	df	Sig. (2-tailed)	Mean Difference	Std. Error Difference	95% Confidence Interval of the Difference	
									Lower	Upper
pTau	Equal variances assumed	82,640	,000	22,808	529	,000	,22708	,00996	,20752	,24664
	Equal variances not assumed			22,469	371,869	,000	,22708	,01011	,20720	,24695

$$d = 2 \times 22.469 / \sqrt{371.869} = 2.330$$

**Group Statistics**

	Hemisphere	N	Mean	Std. Deviation	Std. Error Mean
Reelin	,00	259	,3063	,20171	,01253
	1,00	272	,0685	,04229	,00256

**Independent Samples Test**

		Levene's Test for Equality of Variances		t-test for Equality of Means				95% Confidence Interval of the Difference		
		F	Sig.	t	df	Sig. (2-tailed)	Mean Difference	Std. Error Difference	Lower	Upper
Reelin	Equal variances assumed	264,137	,000	19,013	529	,000	,23783	,01251	,21326	,26240
	Equal variances not assumed			18,590	279,584	,000	,23783	,01279	,21265	,26301

$$d = 2 \times 18.590 / \sqrt{279.584} = 2.224$$

**6.5.5 McGill-R-Thy1-APP 25181**

**Group Statistics**

	Hemisphere	N	Mean	Std. Deviation	Std. Error Mean
pTau	Control	68	,3620	,13928	,01689
	miRNA	58	,5614	,16347	,02146

**Independent Samples Test**

		Levene's Test for Equality of Variances		t-test for Equality of Means				95% Confidence Interval of the Difference		
		F	Sig.	t	df	Sig. (2-tailed)	Mean Difference	Std. Error Difference	Lower	Upper
pTau	Equal variances assumed	1,777	,185	-7,393	124	,000	-,19936	,02697	-,25274	-,14598
	Equal variances not assumed			-7,299	112,684	,000	-,19936	,02731	-,25348	-,14525

$$d = 2 \times 7.393 / \sqrt{124} = -1.328$$

**Group Statistics**

	Hemisphere	N	Mean	Std. Deviation	Std. Error Mean
Reelin	Control	68	,5642	,17319	,02100
	miRNA	58	,0318	,01992	,00262

**Independent Samples Test**

		Levene's Test for Equality of Variances		t-test for Equality of Means				95% Confidence Interval of the Difference		
		F	Sig.	t	df	Sig. (2-tailed)	Mean Difference	Std. Error Difference	Lower	Upper
Reelin	Equal variances assumed	74,360	,000	23,266	124	,000	,53236	,02288	,48707	,57765
	Equal variances not assumed			25,154	69,075	,000	,53236	,02116	,49014	,57458

$$d = 2 \times 25.154 / \sqrt{69.075} = 6.053$$

### 6.5.6 McGill-R-Thy1-APP 25561

#### Mann-Whitney Test

Ranks				
	Hemisphere	N	Mean Rank	Sum of Ranks
p_Tau	Control	27	29,30	791,00
	miRNA	28	26,75	749,00
	Total	55		

#### Test Statistics<sup>a</sup>

p_Tau	
Mann-Whitney U	343,000
Wilcoxon W	749,000
Z	-,589
Asymp. Sig. (2-tailed)	,556

a. Grouping Variable:  
Hemisphere

#### Mann-Whitney Test

Ranks				
	Hemisphere	N	Mean Rank	Sum of Ranks
Reelin	Control	27	25,78	696,00
	miRNA	28	30,14	844,00
	Total	55		

#### Test Statistics<sup>a</sup>

Reelin	
Mann-Whitney U	318,000
Wilcoxon W	696,000
Z	-,1010
Asymp. Sig. (2-tailed)	,312

a. Grouping Variable:  
Hemisphere

$$r = 0.589/\sqrt{55} = 0.079$$

$$r = 1.010/\sqrt{55} = 0.136$$

### 6.5.7 McGill-R-Thy1-APP 25562

#### Group Statistics

	Hemisphere	N	Mean	Std. Deviation	Std. Error Mean
pTau	Control	125	,3780	,20916	,01871
	miRNA	126	,2875	,16810	,01498

#### Independent Samples Test

		Levene's Test for Equality of Variances		t-test for Equality of Means					95% Confidence Interval of the Difference	
		F	Sig.	t	df	Sig. (2-tailed)	Mean Difference	Std. Error Difference	Lower	Upper
pTau	Equal variances assumed	4,718	,031	3,782	249	,000	,09054	,02394	,04338	,13770
	Equal variances not assumed			3,778	237,214	,000	,09054	,02396	,04333	,13775

$$d = 2 \times 3.782/\sqrt{249} = 0.479$$

#### Group Statistics

	Hemisphere	N	Mean	Std. Deviation	Std. Error Mean
Reelin	Control	125	,4638	,20117	,01799
	miRNA	126	,0981	,06386	,00569

#### Independent Samples Test

		Levene's Test for Equality of Variances		t-test for Equality of Means					95% Confidence Interval of the Difference	
		F	Sig.	t	df	Sig. (2-tailed)	Mean Difference	Std. Error Difference	Lower	Upper
Reelin	Equal variances assumed	90,512	,000	19,441	249	,000	,36567	,01881	,32863	,40272
	Equal variances not assumed			19,377	148,556	,000	,36567	,01887	,32838	,40296

$$d = 2 \times 19.377 / \sqrt{148.556} = 3.179$$